MASTER OF SCIENCE IN APPLIED GEOPHYSICS

Time-lapse GPR full-waveform inversion to monitor heat tracers at the Krauthausen test site

Brianna Mueller

August 27, 2023

Time-lapse GPR full-waveform inversion to monitor heat tracers at the Krauthausen test site

MASTER OF SCIENCE THESIS

for the degree of Master of Science in Applied Geophysics
by

Brianna Mueller

August 27, 2023

Dated: *August 27, 2023*

Supervisor(s):

Prof. Dr. Anja Klotzsche
Forschungszentrum Jülich, Universität zu Köln

Prof. Dr. Jan van der Kruk
Forschungszentrum Jülich, RWTH Aachen

Committee Members:

Prof. Dr. Jan van der Kruk
Forschungszentrum Jülich, RWTH Aachen

Prof. Dr. Anja Klotzsche
Forschungszentrum Jülich, Universität zu Köln

Dr. Ranajit Ghose
Technische Universiteit Delft

Zentrales Prüfungsamt/Central Examination Office

Eidesstattliche Versicherung
Statutory Declaration in Lieu of an Oath

Mueller, Brianna	438468
Name, Vorname/Last Name, First Name	Matrikelnummer (freiwillige Angabe) Matriculation No. (optional)

Ich versichere hiermit an Eides Statt, dass ich die vorliegende Arbeit/Bachelorarbeit/Masterarbeit* mit dem Titel
I hereby declare in lieu of an oath that I have completed the present paper/Bachelor thesis/Master thesis* entitled

Time-lapse GPR full-waveform inversion to monitor heat tracers at the Krauthausen test site

selbstständig und ohne unzulässige fremde Hilfe (insbes. akademisches Ghostwriting) erbracht habe. Ich habe keine anderen als die angegebenen Quellen und Hilfsmittel benutzt. Für den Fall, dass die Arbeit zusätzlich auf einem Datenträger eingereicht wird, erkläre ich, dass die schriftliche und die elektronische Form vollständig übereinstimmen. Die Arbeit hat in gleicher oder ähnlicher Form noch keiner Prüfungsbehörde vorgelegen.
independently and without illegitimate assistance from third parties (such as academic ghostwriters). I have used no other than the specified sources and aids. In case that the thesis is additionally submitted in an electronic format, I declare that the written and electronic versions are fully identical. The thesis has not been submitted to any examination body in this, or similar, form.

Aachen, 01.08.2023
Ort, Datum/City, Date

Unterschrift/Signature

*Nichtzutreffendes bitte streichen
*Please delete as appropriate

Belehrung:
Official Notification:

§ 156 StGB: Falsche Versicherung an Eides Statt
Wer vor einer zur Abnahme einer Versicherung an Eides Statt zuständigen Behörde eine solche Versicherung falsch abgibt oder unter Berufung auf eine solche Versicherung falsch aussagt, wird mit Freiheitsstrafe bis zu drei Jahren oder mit Geldstrafe bestraft.
Para. 156 StGB (German Criminal Code): False Statutory Declarations
Whoever before a public authority competent to administer statutory declarations falsely makes such a declaration or falsely testifies while referring to such a declaration shall be liable to imprisonment not exceeding three years or a fine.
§ 161 StGB: Fahrlässiger Falscheid; fahrlässige falsche Versicherung an Eides Statt
(1) Wenn eine der in den §§ 154 bis 156 bezeichneten Handlungen aus Fahrlässigkeit begangen worden ist, so tritt Freiheitsstrafe bis zu einem Jahr oder Geldstrafe ein.
(2) Straflosigkeit tritt ein, wenn der Täter die falsche Angabe rechtzeitig berichtigt. Die Vorschriften des § 158 Abs. 2 und 3 gelten entsprechend.
Para. 161 StGB (German Criminal Code): False Statutory Declarations Due to Negligence
(1) If a person commits one of the offences listed in sections 154 through 156 negligently the penalty shall be imprisonment not exceeding one year or a fine.
(2) The offender shall be exempt from liability if he or she corrects their false testimony in time. The provisions of section 158 (2) and (3) shall apply accordingly.

Die vorstehende Belehrung habe ich zur Kenntnis genommen:
I have read and understood the above official notification:

Aachen, 01.08.2023
Ort, Datum/City, Date

Unterschrift/Signature

Abstract

Understanding solute and heat transport processes in aquifers is crucial for monitoring and protecting the groundwater critical zone. Crosshole ground-penetrating radar (GPR) is a useful method for enhancing transport characterization in aquifers. Particularly, GPR full-waveform inversion (FWI) can provide subsurface images with resolution at the subwavelength scale, making it a well-suited method for monitoring tracer plumes. While previously applied to a salt tracer test, its effectiveness for other tracer types with different conductivity and permittivity contrasts remains unexplored. Here, we apply this method to two tracer tests conducted at the Krauthausen test site in northwest Germany: (1) a natural gradient heat tracer test and (2) a forced-gradient combined heat-salt tracer test. Both tracers use hot water, which provides a contrast in both electrical conductivity and dielectric permittivity with the groundwater. This should permit improved monitoring capabilities with GPR FWI in comparison to the salt tracer, which only provides a contrast in electrical conductivity. However, this comes with new challenges in the processing workflow, specifically, in the starting model strategy. The results illustrate that using the ray-based permittivity tomogram and a homogeneous conductivity as FWI starting models for each time-lapse dataset is the best strategy. Additionally, we applied an amplitude analysis approach to improve the starting model in regions with low ray coverage. The effects of the heat tracer were detected over the entire depth range of the aquifer, from 3-11 m, and especially at mid-aquifer depths from 6-8.5 m. For the heat-salt tracer, we were able to detect separate effects from the salt and heat: the salt was observed at depth in the aquifer, in accordance with the salt tracer test, and the heat was observed approximately two days after the salt effects at mid-aquifer depths (from 5.5-7.5 m). In regions where minimal effects from the tracer were observed, specifically for the heat tracer, the consistent results between independent time-lapse datasets demonstrate the repeatability of the method, indicating the suitability of GPR FWI for hydrogeophysical time-lapse studies.

Acknowledgements

First of all, I want to thank my supervisor Prof. Dr. Anja Klotzsche, for all of the guidance and feedback throughout the processing, fieldwork, and writing stages, and Prof. Dr. Jan van der Kruk for the guidance in theoretical aspects and reviewing. I am grateful to Sophia Schiebel for helping me with organizational matters, getting acquainted with the processing workflow, helping with the field work and equipment, and reviewing my thesis. I also want to express gratitude to everyone else who helped with my fieldwork in May, namely, Dominik Hoven and Thomas Simader. This fieldwork was made possible by collaboration with Dr. Andreas Englert, Hannah Gebhart, and David Hoffmann from the Department of Applied Geology of the University of Halle-Wittenberg for the heat-salt tracer experiment. I would also like to thank Peleg Haruzi and colleagues, who acquired the heat tracer experiment data in 2019. This study was also only possible with access to the JURECA cluster thanks to the Jülich Supercomputing Center (JSC). Finally, I want to thank my fellow Master's students, especially Anton Ziegon, for all of the encouragement, positivity, and advice along the way.

RWTH Aachen University
August 27, 2023

Brianna Mueller

Table of Contents

Chapter 1

Introduction

Monitoring and protecting the groundwater critical zone is crucial for modern life and all living organisms, given its vital role in supplying drinking water, supporting agriculture, and serving as a repository for wastewater. Therefore, understanding transport processes in aquifers is crucial for monitoring groundwater contaminant migration. With comprehensive knowledge of solute transport and preferential flow paths in the subsurface, appropriate remediation efforts can be established to protect groundwater quality and hence minimize environmental impact (Amirabdollahian and Datta, 2013). Additionally, geothermal resource exploitation and monitoring is becoming increasingly important with the current demand for renewable energy and therefore understanding heat transport in heterogeneous aquifers is important (Klepikova et al., 2016). Preferential flow paths on the decimeter scale have a large influence on plume-scale solute and heat transport (Zheng and Gorelick, 2003). Traditional hydrogeological methods for aquifer characterization, such as pumping and tracer tests, are able to provide averaged hydrological properties, mostly applicable to the large-scale. Other hydrogeological methods such as core sampling, slug tests, and logging provide high vertical resolution. However, the properties are measured only at borehole locations and laterally interpolated, which does not provide the true spatial variability of the aquifer properties.

In the last two decades, the use of geophysical methods has enhanced the understanding of aquifer properties at various scales, giving rise to the field of hydrogeophysics (Binley et al., 2015). Geophysical methods are able to close the gap between large-scale and point measurements, providing higher resolution images of the subsurface. Ground penetrating radar (GPR), electrical resistivity tomography (ERT), and seismic methods have been widely used for higher resolution imaging in hydrogeologic contexts (Binley et al., 2002; Bradford et al., 2009; Doetsch et al., 2012; Linde et al., 2006; Coscia et al., 2011; Chen et al., 2010). Geophysical properties obtained from these methods can be related to desired hydrogeological parameters through empirical or petrophysical models (Looms et al., 2008; Linde et al., 2006; Klotzsche et al., 2018).

For the characterization of aquifers in terms of small-scale structures that influence flow and transport processes, GPR has shown high potential. Many studies have investigated the potential of GPR in hydrogeophysical applications (Holliger et al., 2001; Dorn et al., 2011; Dafflon et al., 2011; Giertzuch et al., 2020). GPR uses high frequency electromagnetic pulses and is therefore able to provide the highest resolution among the geophysical methods. Furthermore, the velocity and attenuation of electromagnetic waves measured with GPR can be transformed into the electrical conductivity and dielectric permittivity distributions in the subsurface. Both of these geophysical parameters can be related to hydrogeologic properties, including porosity, water content, salinity, permeability, and changes in lithology (Huisman et al., 2003; Turesson, 2006; Archie, 1942; Topp et al., 1980; Steelman and Endres, 2011).

Various acquisition setups are possible with GPR depending on the application, including surface, single-hole, and crosshole measurements. Crosshole GPR provides a more constrained problem than single-hole or surface measurements, because of the known distance between boreholes, while also having a denser ray coverage (Klotzsche et al., 2019b). Air wave measurements are necessary to determine time zero accurately; for crosshole GPR, wide angle reflection and refraction (WARR) measurements are typically completed for time zero, in which the transmitter position remains fixed while the antenna separation is increased. For crosshole measurements, two measurement types are commonly used: zero-offset profiles (ZOP) and multi-offset gathers (MOG). ZOPs are one-dimensional profiles that are produced when the transmitter and receiver are in two different boreholes and are placed at equal depths such that the recorded signal is assumed to have travelled horizontally (Figure 1-1). The transmitter and receiver are then moved with the same constant spacing to different depths. This provides information on the variations in dielectric permittivity and signal attenuation with depth, averaged horizontally over the span of the plane. In contrast, a MOG is measured by having the transmitter at a fixed location in one borehole, while the receiver is moved with a constant spacing to different depths in the other borehole (Figure 1-1). This is repeated for different transmitter locations and all MOGs are then the input for tomographic imaging and inversion. By collecting data with multiple angles, the ray coverage is improved in the area of interest between the boreholes (Annan, 2005b). The highest resolution is in the center of the crosshole plane as there is a denser ray coverage, while the lowest ray coverage is located near the transmitter and receiver positions.

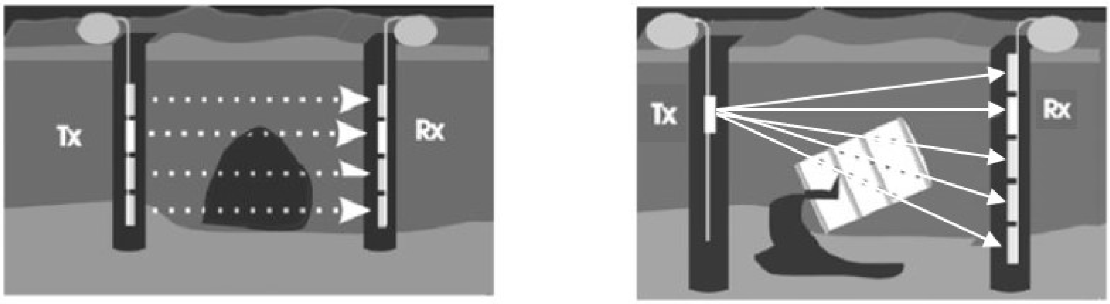

Figure 1-1: Schematic of a zero-offset profile (ZOP) acquisition setup (left) and a multi-offset gather (MOG) acquisition setup (right), based on Annan (2005b).

Traditionally, ray-based approaches were used to invert MOG data, which use the first-arrival times and first-cycle amplitudes of the GPR traces. The resolution capabilities of GPR have been improved with full-waveform inversion (FWI) in the two last decades (Klotzsche et al., 2010; Gueting et al., 2015; van der Kruk et al., 2018; Zhou et al., 2020; Haruzi et al., 2022). GPR FWI uses the entire information content of the measured waveform including reflections and refractions, and therefore provides more accurate and higher resolution results in comparison to standard ray-based inversion techniques. GPR FWI is therefore able to reconstruct smaller features, on the decimeter scale within aquifers. It has been applied to more than 50 datasets from various aquifers and validated with logging data, resulting in an improved aquifer understanding (Gueting et al., 2015, 2017). Studies using GPR FWI have mainly focused on steady-state aquifer characterization. However, to study transport properties, time-lapse studies are necessary.

To study changes over time, tracer experiments are often applied by hydrogeologists and geophysicists. These experiments involve injecting fluid with a contrast in properties to the ambient groundwater into the subsurface and monitoring it over time. Tracer types can be divided into conservative and non-conservative (reactive) substances and subsequently into solutes and particles (Goldscheider et al., 2008). Some common tracer classes include fluorescent dyes, salts, and particles (Goldscheider et al., 2008). The most common tracer type that has been complemented with geophysics is salt, which affects the electrical conductivity of the groundwater and is therefore well-suited for electrical methods (Doetsch et al., 2012). So far, only a few studies applied GPR to monitor salt tracers, since the traditional ray-based inversion has limitations in resolving changes in electrical conductivity (Dorn et al., 2011). Haruzi (2023) showed, for the first time, the potential of GPR FWI to monitor salt tracers in an application at the Krauthausen test site. The results of the salt tracer experiment show transport primarily at deeper parts of the aquifer, because of the density effect of the salt fluids in contrast to the groundwater. Additionally, this salt tracer primarily provides a contrast in electrical conductivity. A more modern tracer type is a heat tracer, which not only concerns advection as a heat transport mechanism in the intergranular phase, where solute transport also occurs, but also the heat conductance of the porous medium (Cirpka et al., 2014). Rau et al. (2014) provide an overview of the use of heat tracers in unconsolidated water-saturated media and outline the use of heat tracers for information on both water flow and thermal dispersion, although quantification of both parameters remains a challenge. With a combined heat and salt tracer, information on both solute transport and thermal dispersion can be obtained. So far, heat tracer experiments have been coupled with geophysics by monitoring with ERT. Hermans et al. (2015) monitored a heat tracer at a test site in Liège, Belgium, using crosshole ERT. In this study, they demonstrated the ability of crosshole ERT to characterize heat transfer in the subsurface and to monitor geothermal resources. GPR FWI was applied at this test site by Zhou et al. (2020) after the heat tracer experiment to better understand the findings from the previous study. Cirpka et al. (2014) applied ERT monitoring in a coupled inversion approach with temperature logging data, pumping tests, and slug tests. To our knowledge, GPR has not yet been applied to heat tracer experiments and could provide promising monitoring capabilities due to the contrast in electrical conductivity and dielectric permittivity that the heat tracer has with the groundwater.

The electromagnetic properties of interest with GPR FWI, the electrical conductivity (σ) and the relative dielectric permittivity (ε_r), referred to as the permittivity for simplicity, vary for different subsurface materials and fluids (Table 1-1) and for varying temperature and salinity. Empirical relations show that the electrical conductivity of the pore fluid increases with temperature (Revil et al., 1998) and salinity (Archie, 1942) and that the permittivity of water decreases with increasing temperature for static values (Kaatze, 1989; Catenaccio et al., 2003; Seyfried and Grant, 2007). This effect is only minor, and an increase in water temperature from 10 to 30°C constitutes a decrease in permittivity from approximately 84 to

76. Seyfried and Grant (2007) show the temperature effects on the real and imaginary parts of the complex permittivity for different soil samples and also provide empirical relationships between bulk permittivity and temperature. Overall, the tracer provides a stronger contrast in conductivity than permittivity in the pore space. These changes in subsurface properties due to the introduced tracers will be encoded in the measured GPR data.

Table 1-1: Typical values for relative dielectric permittivity and electrical conductivity for common subsurface materials at 100 MHz based on Annan (2005a) and Jol (2008).

Material	ε_r [-]	σ [mS/m]
Air	1	0
Fresh water	80	0.5
Sea water	80	3000
Dry sand	3-5	0.01
Saturated sand	20-30	1-10
Silts	5-30	1-100
Clays	5-40	2-1000
Dry salt	5-6	0.01-1
Ice	3-4	0.01

1-1 Objectives and outline

The objective of this thesis is to apply crosshole GPR FWI to time-lapse measurements of two tracer experiments at the Krauthausen test site: a heat tracer experiment, which took place in 2019, and a heat-salt tracer experiment, conducted in May 2023. GPR has not yet been applied to heat tracers to our knowledge as it is an emerging tracer in the field of hydrogeology. This extends on the work of Haruzi et al. (2022) and Haruzi (2023), where these methods were tested numerically for salt, ethanol, and heat tracers and were applied to a salt tracer experiment. With GPR FWI, both the conductivity and the permittivity are simultaneously inverted. Lavoué et al. (2014) demonstrate that the permittivity, which is derived from the travel times, is more constrained and is therefore more reliable than the conductivity, which is derived from attenuation (see Figure 7 in publication). With the use of a heat tracer, a contrast in dielectric permittivity in addition to electrical conductivity with respect to the groundwater is expected; therefore FWI of the time-lapse measurements should provide better monitoring capabilities than with a salt tracer. The results from the numerical studies from Haruzi (2023) for both heat and ethanol tracers, which both provide a contrast in permittivity, show promising results for tracer transport reconstruction. In addition to a more promising contrast in properties and a more constrained problem, the heat tracer does not suffer from density effects as severely as the salt tracer (Shakas et al., 2017) and it provides information for different parts of the aquifer. This is because the heat tracer will not only indicate fluid transport within the pores, but the heat plume will also travel through the grains through conduction and therefore should also show a contrast in the upper aquifer. The heat-salt tracer experiment will be an interesting combination of the modern heat tracer and the conventional salt tracer test from Haruzi (2023) as the heat is expected to be transported through different paths on a slower time-scale than the salt, which only travels through the pore space. For the time-lapse data, various inversion strategies with different starting models are investigated and a guideline for future studies is provided.

In the following chapter, a theoretical overview of electromagnetic wave propagation and the GPR full-waveform inversion workflow and algorithm are given. After the theory section that provides sufficient background in GPR FWI, the main part of the thesis is subdivided into two parts, first, the heat tracer test (Chapter 3-Chapter 5), and second, the heat-salt tracer test (Chapter 6-Chapter 8). In Chapter 3, an overview and description of the Krauthausen test site are given, followed by the data acquisition details for the heat tracer test. The results of the temperature logging data, zero-offset profiles, the starting model FWI tests, and the time-lapse FWI are provided in Chapter 4 and discussed in Chapter 5. The data acquisition details of the heat-salt tracer test are provided in Chapter 6. The temperature logging data, zero-offset profiles, and time-lapse FWI results are then given in Chapter 7 and discussed in Chapter 8. The final conclusions from both tracers are then summarized and an outlook for future research questions and applications is provided in Chapter 9.

Chapter 2

Theory

In this chapter, an overview of electromagnetic wave propagation is provided. The entire full-waveform inversion workflow is then described, including the pre-processing steps, source wavelet estimation, and the full-waveform inversion algorithm.

2-1 Electromagnetic wave propagation

Maxwell's equations describe the propagation of electromagnetic fields. The frequency range for GPR is 10-2600 MHz (Kearey et al., 2002). Maxwell's equations in differential form in the time domain as given by Annan (2005a) are:

$$\nabla \times \mathbf{E} = -\frac{\partial \mathbf{B}}{\partial t} \tag{2-1}$$

$$\nabla \times \mathbf{H} = \mathbf{J} + \frac{\partial \mathbf{D}}{\partial t} \tag{2-2}$$

$$\nabla \cdot \mathbf{D} = \rho \tag{2-3}$$

$$\nabla \cdot \mathbf{B} = 0, \tag{2-4}$$

where $\mathbf{E}$ is the electric field strength vector [V/m], $\mathbf{B}$ is the magnetic flux density vector [T], $\mathbf{H}$ is the magnetic field intensity [A/m], $\mathbf{D}$ is the electric displacement vector [C/m^2], $\mathbf{J}$ is the electric current density vector [A/m^2], ρ is the electric charge density [C/m^2], and t is time [s].

The constitutive relations relate material physical properties to the applied electromagnetic field. For EM and GPR methods, the electric and magnetic properties of the subsurface are important (Annan, 2005a). In reality, subsurface properties are anisotropic, heterogenous, non-linear, and complex. For modelling and inversion purposes, subsurface properties are often simplified to be isotropic, linear, and non-dispersive (frequency independent) (Annan, 2005a), such that the constitutive relations are simplified to:

$$\mathbf{J} = \sigma \mathbf{E} \tag{2-5}$$
$$\mathbf{D} = \varepsilon \mathbf{E} \tag{2-6}$$
$$\mathbf{B} = \mu \mathbf{H}, \tag{2-7}$$

where **J** is the electric current density vector, **E** is the electric field strength vector, **D** is the electric displacement vector, **B** is the magnetic flux density vector, and **H** is the magnetic field intensity. Here the electrical conductivity, σ, the dielectric permittivity, ε, and the magnetic permeability, μ, are all constants in this simplification rather than tensors. By substituting the constitutive relations and combining Eq. (2-1) and Eq. (2-2), the transverse vector wave equation is obtained:

$$\nabla^2 \mathbf{E} + \mu\varepsilon \frac{\partial^2 \mathbf{E}}{\partial t^2} + \mu\sigma \frac{\partial \mathbf{E}}{\partial t} = 0 \tag{2-8}$$
$$\nabla^2 \mathbf{H} + \mu\varepsilon \frac{\partial^2 \mathbf{H}}{\partial t^2} + \mu\sigma \frac{\partial \mathbf{H}}{\partial t} = 0. \tag{2-9}$$

Eq. (2-8) and Eq. (2-9) are the transverse vector wave equation for a coupled set of electric and magnetic fields that vary with time, which are described by Maxwell's equations in Eq. (2-1)-Eq. (2-2) (Annan, 2005a). The second term of Eq. (2-8) can be referred to as the displacement current term, while the third term is related to conduction current. For GPR, the high frequencies lead to the displacement current term dominating over the conduction current term and therefore wave propagation dominates over diffusion. Eq. (2-8) then simplifies to the following wave equation:

$$\nabla^2 \mathbf{E} + \mu\varepsilon \frac{\partial^2 \mathbf{E}}{\partial t^2} = 0. \tag{2-10}$$

The solution to this simplified wave equation in low-loss environments for a plane EM wave with negligible magnetic effects ($\mu = 1$) is of the form (Annan, 2005a):

$$E(z,t) = \mathbf{E}_0 e^{\pm i(\omega t - kz)}, \tag{2-11}$$

where ω is the angular frequency and k is the propagation constant, defined as (Slob et al., 2010)

$$k = \sqrt{i\omega\mu\sigma + \omega^2\mu\varepsilon} = \alpha + \frac{i\omega}{v}, \tag{2-12}$$

where velocity, v, and attenuation, α, respectively, are given by (Jol, 2008):

$$v = \frac{c}{\sqrt{\varepsilon_r}}, \tag{2-13}$$

$$\alpha = \frac{\sigma}{2}\sqrt{\frac{\mu}{\varepsilon}}, \tag{2-14}$$

where $\varepsilon_r = \varepsilon/\varepsilon_0$ is the relative dielectric permittivity or the dielectric constant. In this thesis, this parameter is referred to as the permittivity for simplicity. These relations for radar velocity and attenuation are only valid with the low-loss approximation, $\sigma << \omega\varepsilon$, which yields wave-like behaviour such that GPR is considered valid, and taking the magnetic permeability as the free-space value, which is acceptable for most earth materials (Slob et al., 2010).

2-2 Full-waveform inversion methodology

The full-waveform inversion workflow is shown in Figure 2-1. In Part I, pre-processing including noise removal and dewow, time zero correction, ray-based inversion, and 3D to 2D correction are applied. In Part II, the source wavelet estimation is completed by first estimating an initial source wavelet and applying two source wavelet corrections. The full-waveform inversion is then performed in Part III and its steps are described in section 2-2-3.

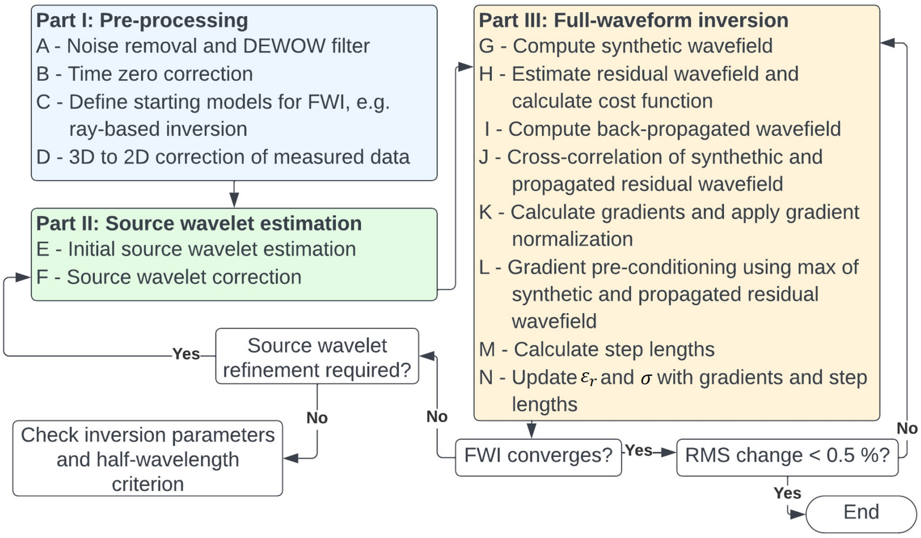

Figure 2-1: Full-waveform inversion workflow overview adapted from Klotzsche et al. (2010).

2-2-1 Pre-processing

In step A of Figure 2-1, first a dewow filter is applied to remove the initial DC signal component and the ringing of the low-frequency signal trend (Cassidy and Jol, 2009), followed by a bandpass filter to remove any noise outside of the source frequency range in the case of noisy data. A crucial step is then to determine time zero in step B. Time zero is defined as the time when the transmitter initiates signal emission and it is unknown, system dependent, and can vary in time (Annan, 2005a). The travel time of the wave depends on this exact starting time and variations in time zero over the course of the measurement period due to thermal drift, cable length differences, variations in antenna coupling, and electronic instability need to be accounted for (Cassidy and Jol, 2009). Errors associated with this time zero correction can propagate into subsequent processing steps and it is difficult to recognize later at all. To correct for time zero, two common methods can be applied: the WARR method and the ZOP-MOG cross-correlation method. For the WARR method, several point WARR measurements in air are performed over the time of the acquisition, which can be used to define the t_0 shift using the air wave speed as

$$t_0^{abs} = t^{fb} - \frac{x^t - x^r}{c_0}, \tag{2-15}$$

where t^{fb} is the first break time, c_0 is the speed of the EM wave in air (3×10^8 m/s), x^t is the position of the transmitter, and x^r is the position of the receiver. These obtained time zeros can then be linearly interpolated to the time of the MOG measurements.

A second more accurate method was introduced by Oberröhrmann et al. (2013). For this method, one WARR measurement in air is performed close in time to a ZOP measurement, which is time corrected with the WARR time zero. By assuming that each MOG measurement has an identical measured ZOP position, the corrected ZOP data can in a second step be used via cross-correlation of the ZOP and MOG data to determine an individual time zero for each MOG. The cross-correlation of the z-component of the electric field between two corresponding traces, i is given by

$$(E_{z,i}^{ZOP} * E_{z,i}^{MOG})(\tau) = \sum_{-\infty}^{\infty} E_{z,i}^{ZOP}(t) \cdot E_{z,i}^{MOG}(t+\tau)dt, \tag{2-16}$$

where the time lag, τ, of the maximum of the cross-correlation indicates the relative time zero shift. This provides information on the similarity of the traces and therefore the suitability to use the trace for the time zero correction. Generally, there is a good similarity between MOG and ZOP traces within the saturated zone. This method provides a time zero for each measurement and is therefore more accurate than using the CMP method, which is only an interpolation.

It is important that the starting models for the FWI produce synthetic data that is within half of a wavelength of the observed data for the FWI to converge to the global minimum and avoid local minimum trapping; this is referred to as the half-wavelength criterion (Meles et al., 2012). These starting models are determined using ray-based inversion techniques. The filtered and time zero corrected data are the input for the ray-based inversion (Figure 2-1, step C). For this, first-break picking is completed for all MOGs to obtain the first arrival times and the maximum first-cycle amplitudes, which are then inverted to obtain velocity and attenuation tomograms, respectively. We use a non-linear finite-difference implementation of the Eikonal equation for the ray-based inversion (Holliger et al., 2001; Maurer and Musil, 2004), which takes into account the curvature of the ray paths. This allows for more accurate modelling of heterogeneous media in comparison to other ray-tracing algorithms (Vidale, 1990). Damping and smoothing regularization are applied to stabilize the inversion (Holliger et al., 2001). The velocity and attenuation tomograms obtained from the ray-based inversion are then converted to permittivity and conductivity distributions using Eq. (2-13) and Eq. (2-14), respectively, which are then the starting models for the FWI.

Ray-based results are often less reliable close to the water table because of the low ray coverage and additional testing to update the starting model is needed. One option is to apply the so-called amplitude analysis (AA) approach (Klotzsche et al., 2012; Zhou et al., 2020), which helps to identify wave-guiding structures. High contrast layers in the subsurface, e.g., high porosity or clay lenses, can act as low velocity waveguides if their velocity is lower than the surrounding material and the thickness smaller than the dominant wavelength (Zhou et al., 2020). These waveguiding layers cause internal multiple reflections beyond the critical angle which create distinct late arrival high amplitude events in the data (Van der Kruk et al., 2009). Such low-velocity waveguides could be linked to high porosity layers and therefore they should not be disregarded. An amplitude analysis (AA) approach proposed by Klotzsche et al. (2012) enables locating the waveguide layer by identifying trace energy maxima, which corresponds to receivers located within the waveguide, and mapping its boundaries by identifying minima in trace energy for receivers located outside of the waveguide layer or at the boundaries of the layer. Zhou et al. (2020) distinguish between two types of waveguides: those caused by a high permittivity and a low or intermediate conductivity (type I), which can be related to high porosity zones and have characteristic elongated wave trains and diminished amplitudes at the boundaries, and those caused by a high permittivity and high conductivity (type II), which can be related to high clay content layers and do not have elongated wave trains due to the high attenuation, but diminished amplitudes can be observed. This is also a relatively simple analysis as the raw or dewowed data can be used and therefore some low-velocity/high permittivity layers can be identified prior to extensive processing and inversion. This can add prior information if modifications in the starting model for the FWI are needed to satisfy the half-wavelength criterion.

Once satisfactory starting models are determined, the final pre-processing step applied to the data is the 3D-to-2D correction of the measured data (Figure 2-1, step D). The EM wave has different radiation patterns in 2D and 3D space. Since we will use 2D modelling for the 2D finite difference time domain (FDTD) forward modelling as given by Ernst et al. (2007b), the Bleistein function is applied to transform the 3D measured data to 2D (Klotzsche et al., 2019b). The transformation applies a scaling factor of $1/\sqrt{\omega}$ and a phase shift of $\pi/4$ and is given by (Bleistein, 1986)

$$\hat{\mathbf{E}}^{2D}(\mathbf{x}_{trn}, \mathbf{x}_{rec}, \omega) = \hat{\mathbf{E}}^{obs}(\mathbf{x}_{trn}, \mathbf{x}_{rec}, \omega)\sqrt{\frac{2\pi t(\mathbf{x}_{trn}, \mathbf{x}_{rec})}{-j\omega\varepsilon^{mean}\mu}}, \tag{2-17}$$

where $\hat{\mathbf{E}}^{2D}$ and $\hat{\mathbf{E}}^{obs}$ are the corrected 2D and the observed 3D data for each transmitter, $\mathbf{x}_{trn}$, and receiver, $\mathbf{x}_{rec}$, position, respectively, ε^{mean} is the mean dielectric permittivity from the starting model, ω is the angular frequency, μ is the magnetic permeability, and t indicates the travel times of each measurement location. This 3D-to-2D conversion introduced by Bleistein (1986) assumes that the highest amplitude is associated with the first-arrival time, which is not always the case, for example, in the presence of high contrast waveguiding layers that cause high amplitudes at late arrival times (Mozaffari et al., 2020). Additionally, out-of-plane effects influence the data, however, by considering only the first few cycles by reducing the time window, these effects should be minimal (Ernst et al., 2007a). Haruzi (2023) investigates these out-of-plane effects using 3D modelling and finds only minor effects from out-of-plane reflections. The fit between 2D-corrected 3D data and corresponding 2D data has been shown to be in agreement, but only for far-field conditions (Ernst et al., 2007a). Despite the errors that this Bleistein filter introduces, it is still necessary to apply it in order to use 2D modelling. The difference between the data before and after applying this 3D-to-2D conversion should therefore be monitored to ensure that the traces are not shifted by more than half a wavelength, which would hinder the convergence of the FWI.

2-2-2 Source wavelet estimation

In order to accurately model the measured wavefield, it is important to obtain an effective source wavelet (Figure 2-1, Part II). In the 2D case where these effects have not been included in the model, this effective source wavelet contains the information about the borehole filling, borehole tube, antennae coupling, and finite antennae length, which allows to account for these effects (Klotzsche et al., 2019a). The source wavelet estimation can be divided into three parts as shown in Figure 2-2: Part A, the initial source wavelet estimation, Part B, the source wavelet correction, and Part C, further corrections in the full-waveform inversion. The workflow follows the steps as described by Klotzsche et al. (2010). More information can be found in this publication.

In Part A, the initial source wavelet estimation is completed by first estimating the average horizontal trace from ZOP data and its neighbouring horizontal traces from MOG data (Figure 2-2, step 1). With the use of a cross-correlation method, the similarity of the waveforms for each transmitter is evaluated and waveform outliers can be discarded. This initial estimate does not consider amplitudes as the traces are normalized to 1. Therefore, only the shape of the wavelet is estimated in this step. From Maxwell's equations, we know that the electric field is proportional to the time derivative of the current density source wavelet, which is equivalent to multiplication with $i\omega$ in the frequency domain. The initial source wavelet, $\mathbf{S}_{ini}(t)$, is then determined by dividing the average Fourier-transformed electric field pulse by $i\omega$ in the frequency domain (Figure 2-2, step 2).

In Part B, synthetic radargrams, $\mathbf{E}^{syn}(t)$, are calculated for each transmitter-receiver pair using the 2D finite-difference time domain forward modelling code in Cartesian coordinates from Ernst et al. (2007b) with the initial source wavelet and the initial permittivity, $\varepsilon_{k=0}$, and conductivity, $\sigma_{k=0}$, models from the ray-based inversion (Figure 2-2, steps 3 and 4). Theoretically, the measured data are represented by the convolution of the true source wavelet with the Earth's impulse response, however, the latter is unknown. Therefore, a Green's function, which is a best estimate of the Earth's impulse response, is used. An effective source wavelet is then determined by deconvolving the data in the frequency domain with the appropriate Green's function, $\hat{\mathbf{G}}(f)$, in steps 5 and 6 of Figure 2-2. The Green's function is derived in step 5 by dividing the Fourier-transformed synthetic data, $\hat{\mathbf{E}}^{syn}(f)$, by the Fourier-transformed initial source wavelet spectrum. The updated source wavelet spectrum, $\hat{\mathbf{S}}_{k+1}(f)$, is then estimated by dividing the Fourier-transformed observed data, $\hat{\mathbf{E}}^{obs}(f)$, by this Green's function using all traces in a least-squares sense (Ernst et al., 2007a). Pre-whitening factors η_D and η_I are applied in these steps to avoid division by zero. Finally, the updated source wavelet spectrum is inverse Fourier-transformed which results in the time domain effective source wavelet, $\mathbf{S}_{k+1}(t)$ (Figure 2-2, step 7). The source wavelet is further updated in Loop 1 by repeating steps 3-7 until the solution has converged. Generally, one or two source wavelet corrections suffice, the first to accurately fit the shape and the second to mainly fit the amplitude. Source wavelet refinement can be further applied in Part C during the full-waveform inversion if necessary, after the permittivity and conductivity models have been updated (Figure 2-2, Loop 2). Note that there is no rule of thumb for how many iterations are necessary and the only option is to perform tests.

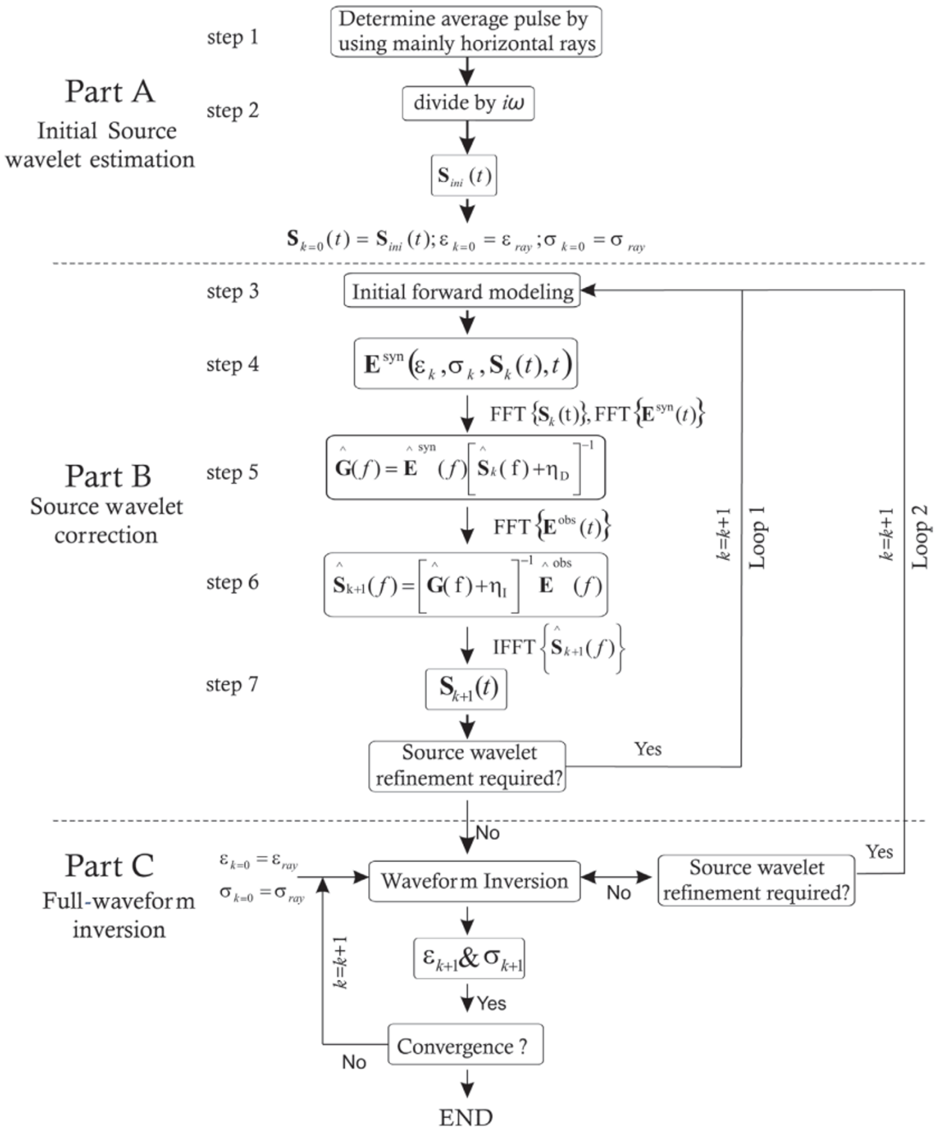

Figure 2-2: Source wavelet estimation workflow adapted from Klotzsche et al. (2010)

.

2-2-3 Full-waveform inversion

Crosshole GPR FWI is a gradient-based method as proposed by Tarantola (1984) for the inversion of seismic reflection data. The first approach for GPR FWI was introduced by Ernst et al. (2007a) and further enhanced by Meles et al. (2010) to include the vectorial behaviour of the fields and simultaneous updating of permittivity and conductivity. Generally, the FWI tries to minimize the misfit function between the observed and synthetic wavefields.

Here, we provide the main steps in the FWI as shown in Part III of Figure 2-1; more details can be found in Meles et al. (2010). The cost or misfit function is minimized for all transmitter-receiver pairs within a set time window by computing the gradients of the cost function to obtain the update directions, in a steepest descent method, and subsequently computing the step lengths. The cost function is given as

$$C(\varepsilon,\sigma) = \frac{1}{2}\sum_{s}\sum_{r}\sum_{\tau}\left[\mathbf{E}^{syn}(\varepsilon,\sigma) - \mathbf{E}^{obs}\right]^{T}_{r,\tau}\delta(\mathbf{x}-\mathbf{x}_r, t-\tau)\left[\mathbf{E}^{syn}(\varepsilon,\sigma) - \mathbf{E}^{obs}\right]_{r,\tau}, \quad (2\text{-}18)$$

where T indicates the adjoint operator, $\mathbf{x}$ and t are the space and time domain of the wavefields, $\mathbf{x}_r$ is the receiver location, and s, r, and τ indicate summing over sources, receivers, and observation times. The synthetic wavefield, $\mathbf{E}^{syn}$, is calculated in step G (Figure 2-1) with the effective source wavelet and the starting models using 2D FDTD forward modelling to solve Maxwell's equations; it is important that this synthetic data is within half of a wavelength of the observed data. Then, the cost function (Eq. (2-18)) and residual wavefield are computed in step H. The residual wavefield is defined as the difference between the observed wavefield and the synthetic wavefield for each transmitter, calculated by

$$\mathbf{R}^s = \delta(\mathbf{x}-\mathbf{x}_r, t-\tau)\left[\mathbf{E}^{syn}(\varepsilon,\sigma) - \mathbf{E}^{obs}\right]_{r,\tau} = \sum_{r}\sum_{\tau}\left[\Delta\mathbf{E}^s\right]_{r,\tau}. \quad (2\text{-}19)$$

This residual wavefield is back-propagated, as indicated in step I (Figure 2-1), from all receivers to the corresponding transmitters. The gradients of the cost function for the permittivity and conductivity are given by

$$\begin{bmatrix} \nabla C_\varepsilon(\mathbf{x}') \\ \nabla C_\sigma(\mathbf{x}') \end{bmatrix} = \sum_{s} \begin{matrix} (\delta(\mathbf{x}-\mathbf{x}')\partial_t\mathbf{E}^{syn})^T\hat{\mathbf{G}}^T\mathbf{R}^s \\ (\delta(\mathbf{x}-\mathbf{x}')\mathbf{E}^{syn})^T\hat{\mathbf{G}}^T\mathbf{R}^s \end{matrix}, \quad (2\text{-}20)$$

where $\partial_t\mathbf{E}^{syn}$ is the virtual source at position $\mathbf{x}'$ that generates the field $\mathbf{E}^{syn}$, which is the electric field for the current model at a source, s.

Through cross-correlation of the synthetic and back-propagated residual field and by summing over all transmitters and times, the gradient and therefore the update direction is obtained (Figure 2-1, steps J and K). The gradients indicate where and how the permittivity and conductivity must be updated to minimize the cost function. The gradients depend on the number of transmitters and receivers and therefore we apply gradient normalization by dividing by the number of transmitters times the number of receivers to allow comparability between different measurement setups (Yang et al., 2013). To avoid artifacts in the inversion near the boreholes due to the relatively high gradients in comparison to the region between boreholes, a gradient preconditioning operator is applied in step L to damp these transmitter and receiver artifacts (Klotzsche et al., 2019b). This operator uses the maximum values of the forward-propagated field and the back-propagated residual field and is defined as (Kurzmann et al., 2013; van der Kruk et al., 2015)

$$\mathbf{P}^k(\mathbf{x}) = \frac{\mathbf{b}(\mathbf{x})}{\max_x \mathbf{b}(\mathrm{x})}, \tag{2-21}$$

where

$$\mathbf{b}(\mathbf{x}) = \frac{1}{a(\mathbf{x}) + C_{stab}\overline{a}} \tag{2-22}$$

and

$$a(\mathbf{x}) = \max_t |\mathbf{E}^{syn}| + \max_t |\mathbf{R}^S|. \tag{2-23}$$

The parameter $\overline{a}$ indicates the spatial average of $a(\mathbf{x})$ and C_{stab} is a manually estimated coefficient for both ε_r and σ gradients that is often between 1-100 that stabilizes $\mathbf{P}^k$ by scaling its value and range. Additionally, a bleeding zone is defined close to the model borders where the gradients of these cells are set to the average of the neighbouring cell gradients. A Gaussian smoothing filter is also applied to the gradients over the entire domain.

To determine how far in the update directions models should be updated, the step lengths are calculated in step M as

$$\zeta_\varepsilon = \kappa_\varepsilon \frac{\sum_s \sum_r \sum_\tau \left[\mathbf{E}^{syn}(\varepsilon + \kappa_\varepsilon \nabla C_\varepsilon, \sigma) - \mathbf{E}^{syn}(\varepsilon, \sigma)\right]^T_{r,\tau} \delta(\mathbf{x} - \mathbf{x}_r, t - \tau) \left[\mathbf{E}^{syn}(\varepsilon, \sigma) - \mathbf{E}^{obs})\right]_{r,\tau}}{\sum_s \sum_r \sum_\tau \left[\mathbf{E}^{syn}((\varepsilon + \kappa_\varepsilon \nabla C_\varepsilon, \sigma) - \mathbf{E}^{syn}(\varepsilon, \sigma)\right]^T_{r,\tau} \delta(\mathbf{x} - \mathbf{x}_r, t - \tau) \left[\mathbf{E}^{syn}((\varepsilon + \kappa_\varepsilon \nabla C_\varepsilon, \sigma) - \mathbf{E}^{syn}(\varepsilon, \sigma)\right]_{r,\tau}} \tag{2-24}$$

and

$$\zeta_\sigma = \kappa_\sigma \frac{\sum_s \sum_r \sum_\tau \left[\mathbf{E}^{syn}(\varepsilon, \sigma + \kappa_\sigma \nabla C_\sigma) - \mathbf{E}^{syn}(\varepsilon, \sigma)\right]^T_{r,\tau} \delta(\mathbf{x} - \mathbf{x}_r, t - \tau) \left[\mathbf{E}^{syn}(\varepsilon, \sigma) - \mathbf{E}^{obs})\right]_{r,\tau}}{\sum_s \sum_r \sum_\tau \left[\mathbf{E}^{syn}((\varepsilon, \sigma + \kappa_\sigma \nabla C_\sigma) - \mathbf{E}^{syn}(\varepsilon, \sigma)\right]^T_{r,\tau} \delta(\mathbf{x} - \mathbf{x}_r, t - \tau) \left[\mathbf{E}^{syn}(\varepsilon, \sigma + \kappa_\sigma \nabla C_\sigma) - \mathbf{E}^{s}(\varepsilon, \sigma)\right]_{r,\tau}}, \tag{2-25}$$

where perturbation factors, κ_ε and κ_σ, should be chosen appropriately to avoid slow convergence or surpassing the FWI result. Separate step lengths for conductivity and permittivity are required because of their differences in sensitivities. The introduction of the simultaneous update results in a reduction of the total FDTD calculations in comparison to the previous approach by Ernst et al. (2007a), hence reducing computational costs. Finally, the updated permittivity and conductivity models are updated in step N (Figure 2-1) with the determined step lengths and directions with the following:

$$[\varepsilon_{upd}] = [\varepsilon] - \zeta_\varepsilon \left[\nabla C_\varepsilon\right], \tag{2-26}$$

$$[\sigma_{upd}] = [\sigma] - \zeta_\sigma \left[\nabla C_\sigma\right]. \tag{2-27}$$

Steps G-N are repeated in the loop shown in Figure 2-1 until the inversion stopping criteria as indicated by Klotzsche et al. (2019b) are reached. They showed that when these four criteria are satisfied, the FWI result is reliable: the root-mean-squared error (RMS) of the observed and modelled data changes less than 0.5% between subsequent iterations, the RMS is reduced by at least 50% from the ray-based inversion starting models, there is little to no remaining gradients, and the cross-correlation coefficient indicating the fit between the measured and modelled data is greater than 0.8.

Part I

Heat tracer

Chapter 3

Experimental setup

3-1 Krauthausen test site

The Krauthausen test site in northwest Germany located 10 km northwest of the city of Düren was set up by the research center Jülich in 1993 (Gueting et al., 2015). The site is situated in the Lower Rhine Embayment and covers an area of 200 by 70 m (Vereecken et al., 2000). There are over 70 wells at the site that are used for pumping and water sampling and they all reach depths of up to 9-12 m. Extensive field measurements, including crosshole GPR (Oberröhrmann et al., 2013; Gueting et al., 2015; Zhou et al., 2020, 2021), pumping and flowmeter tests (Li et al., 2007), ERT (Kemna et al., 2002; Müller et al., 2010), cone penetration tests (Tillmann et al., 2008), borehole velocity measurements (Englert, 2003), and tracer experiments (Vereecken et al., 2000; Müller et al., 2010), have been performed at the Krauthausen test site with the goal of characterizing the aquifer and subsequently studying aquifer parameters on solute transport. The extensive data and analysis that has been conducted at the Krauthausen test site provides an opportunity to test new methods in a well-understood geologic and hydrological setting.

Döring (1997) distinguished three layers in the aquifer: the base of the aquifer corresponds to the lower Rhine sediments, overlain by the upper Rhine sediments, and an upper layer of the Rur river sediments. The uppermost unconfined aquifer, deposited by a local braided river system of the Rur, is the zone of interest for the heat and heat-salt tracer tests; it extends to a depth of approximately 11-12 m and is limited below by a clay layer (Englert, 2003). In the generalized geologic cross-section of the uppermost aquifer from Tillmann et al. (2008) (Figure 3-1a), they identified a fining upwards sandy gravel layer with an intermediate hydraulic conductivity from approximately 6 to 11.5 m depth, a coarse well-sorted sand layer with a lower hydraulic conductivity from 4 to 6 m depth, and a medium gravel layer from 1 to 4 m depth with a high hydraulic conductivity. Above the aquifer is an approximately 1 m thick layer of loamy soil (Gueting et al., 2015). The aquifer has an average total porosity of 26% and an average clay content of 2% (Döring, 1997; Vereecken et al., 2000). The groundwater table depth varies seasonally between ∼1-3 m (Englert, 2003). The regional groundwater flow direction in the study area is 340°N, indicated by the blue arrow in Figure 3-1b, the mean flow magnitude is about 0.9 m/day (Müller et al., 2010), the mean hydraulic gradient is 0.002, and the average hydraulic conductivity is $3.8 \cdot 10^{-3}$ m/s (Vereecken et al., 2000). Previous studies have shown that GPR is a suitable geophysical method in the uppermost aquifer at the test site as the average electrical conductivity is relatively low, ranging from 10 to 25 mS/m (Zhou et al., 2021), and has a low average clay content.

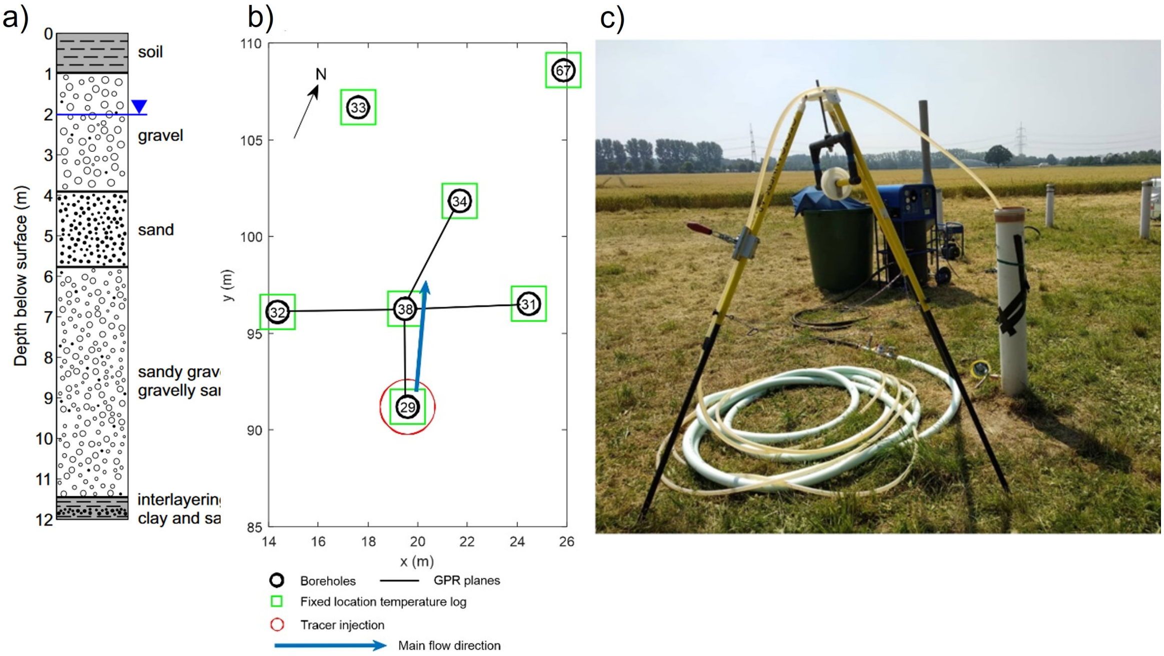

Figure 3-1: (a) General cross-section of the uppermost aquifer from Tillmann et al. (2008), b) map of the boreholes included in the heat tracer experiment at the Krauthausen test site in a site-defined coordinate system, and (c) field site photo showing the injection system.

3-2 Data acquisition and measurement setup

In this first heat tracer experiment, which took place in June and July 2019 at the Krauthausen test site, a set of 6 boreholes in the center of the test site was chosen (Figure 3-1b). In the southern-most well, B29, 36 m^3 of hot water with a temperature of 44°C, providing an approximate temperature anomaly of 34°C, was injected as depicted in Figure 3-1c. Higher temperatures were not possible due to the temperature rating of the PVC tube, which was screened to the aquifer between 3-11 m depth. The water source for the heat tracer was the groundwater at the test site, which supplied water to a heat pump during the injection. The heat pump was located near the injection borehole to avoid losses in the pipe prior to entering the borehole. The temperature sensor in the heat pump indicated constant temperatures throughout the injection period. The injection flow rate was 1.8 m^3/h and it took place over the course of nearly 21 h. Within the aquifer, the tracer travelled with the natural flow direction (Figure 3-1b, blue arrow). High resolution temperature loggers with 0.001°C accuracy were installed at different depths in injection well B29 and monitoring wells B31, B32, B38, B33, B34, and B67, as shown in Figure 3-1a and were monitored over a 54 day period.

Crosshole GPR data were acquired before (background) and after (time-lapse) the heat tracer injection, which took place on Day 1. Four crosshole plane configurations were measured using 200 MHz PulseEKKO borehole antennae (Sensors & Software Inc.). A total of 46 crosshole GPR datasets were acquired over the course of 36 days (Table 3-1). Each dataset, including background and time-lapse, is comprised of MOGs that were collected at approximately 3.3-10.3 m depth with a 0.4 m transmitter spacing from 3.3-7.7 m depth, a 0.2 m transmitter spacing from 8.1-10.3 m depth, and a constant 0.1 m receiver spacing in a semi-reciprocal setup according to Oberröhrmann et al. (2013) to obtain adequate ray coverage with an efficient acquisition time. The acquisition time is minimized to ensure that there is not significant tracer movement during the acquisition. This setup results in approximately 40 MOGs per crosshole dataset. WARR measurements in air were completed at the beginning, middle, and end of the acquisition for the time zero calibration. Additionally, ZOPs were measured at the middle and end of the acquisition with a 0.1 m spacing for the time zero correction and for 1D time-lapse ZOP analysis. Borehole deviations from the vertical were recorded prior to the experiment with a deviation log to obtain more accurate transmitter and receiver positions. The borehole tubes are georeferenced and the depth scale is normalized to the height of the highest borehole at the test site, as in Zhou et al. (2021) and Gueting et al. (2015).

Table 3-1: Acquisition details for all four crosshole planes measured during the heat tracer test. The number of transmitters/multi-offset gathers (trn) and the number of receivers (rec) are given for the background (BG) datasets and all time-lapse monitoring days.

Plane	**2938**		**3834**		**3238**		**3831**	
Day	trn	rec	trn	rec	trn	rec	trn	rec
BG	47	142	46	142	43	135	40	128
2	47	142						
3	47	142						
4	47	142			43	135	40	128
5	47	142			43	135	40	128
6	47	142			43	135	40	128
7	47	142			43	135	40	128
8	46	142			43	135	40	128
9					43	135	40	128
10	47	142			43	135	40	128
11					43	135	40	128
13					43	135	40	128
14	37	142	47	142	35	135	33	128
17	36	142	47	142	35	135	33	128
20					35	135	33	128
24					34	135	33	128
28					35	135	33	128
37					35	135	33	128

Chapter 4

Results

In this chapter, the temperature log data are presented, followed by the zero-offset profiles, and finally the FWI results. The FWI results of the background (before tracer injection) dataset for the injection plane (Plane 2938) are shown in detail. Time-lapse permittivity starting model strategies are tested and the optimal strategy is then applied for all time-lapse datasets for all four crosshole planes. Difference plots between the background and time-lapse FWI results are compared for different days and crosshole planes to recover the tracer distribution over the monitoring period. We expect a decrease in permittivity and an increase in conductivity (decrease in amplitude) with respect to the background FWI results for the time-lapse datasets in the presence of the heat tracer.

4-1 Temperature logging data

High resolution temperature logs were measured at various depths and the results are shown in Figure 4-1 for boreholes B29, B38, B34, B31, and B32, in which the GPR crosshole data were measured. Note that raw data are presented and measurements at depths shallower than 5 m are higher due to the high air temperature in the summer. Borehole B29, the injection borehole, has data for depths of 3.6, 4.5, 7, 8, and 8.9 m and has a starting temperature of 44°C during injection, after which the temperature exponentially decreases with time to 11°C at day 10-20, depending on the depth of the sensor. At 3.6 and 4.5 m depth, the temperature decreases slower than other depths and approaches 12°C. Borehole B38 has temperature data at only 8.9 m depth, however, this borehole is not screened to the aquifer and therefore the heat was transported through the PVC tube. It shows a peak in temperature on day 9, with a temperature increase of 7.5°C relative to the temperature on day 1. Borehole B34 is located the farthest from the injection borehole and shows an increase from day 2 to day 37 at 3.6 m depth, which levels out at 13°C, a 2.5°C increase relative to the temperature before injection. The temperature does not increase until day 9 for depths of 4.5, 7, and 8.9 m and peaks at approximately day 22-25. The temperature at these depths does not reach higher than 11°C. Borehole B31, in the East, only shows a temperature change up to 0.6°C over the entire monitoring period. At 4.5 m depth, the temperature increases from 10.4 to 11°C right after injection up until day 30. At 8.9 m depth, there is an increase from 10.5 to 10.7°C until day 16, after which there are minimal changes observed. The western-most borehole, B32, shows a linearly increasing temperature at 4.5 m depth from 11 to 13.5°C over the entire monitoring period. At 8.9 m depth, the temperature only rises to 10.7°C until day 16, after which the curve flattens out.

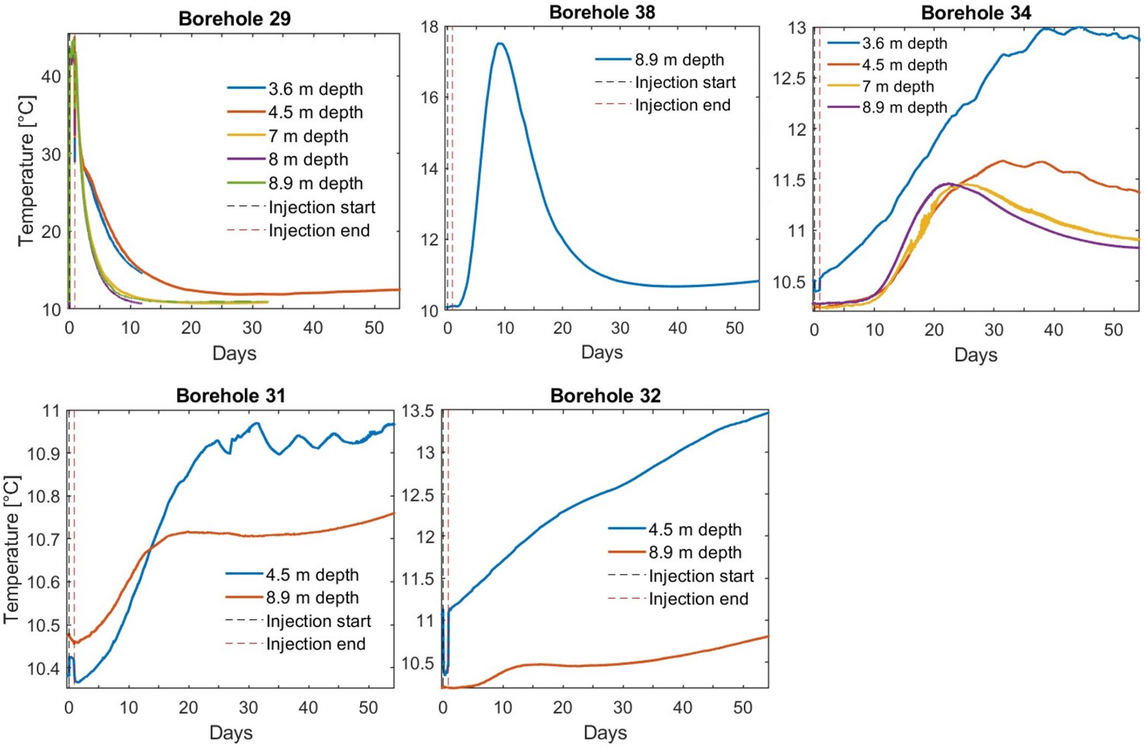

Figure 4-1: Raw temperature breakthrough curves at different depths for boreholes B29, B38, B34, B31, and B32. Note that borehole B38 is not screened to the aquifer and therefore the heat was transported through the PVC tube. Temperature axis are scaled to the maximum value of each borehole.

4-2 Zero-offset profiles

To obtain an initial estimate of the changing permittivity and conductivity of the subsurface over the course of the heat tracer experiment, zero-offset profiles (ZOP) are analyzed (Looms et al., 2008). By picking the first arrival time for each trace of the ZOP measurement, the velocity and therefore the permittivity can be calculated using Eq. (2-13). Information about the attenuation can be obtained by investigating maximum amplitudes, derived from the ZOP measurements, which can be related to the conductivity distribution according to Eq. (2-14). Each ZOP is corrected with the time of the closest WARR measurement, which can cause small differences in the permittivity profiles. The profiles for each time-lapse dataset can indicate the influence of the tracer when compared to the background. Note that these profiles provide averaged properties across the entire plane and therefore should not be over-interpreted, but they provide initial insight into the change in permittivity and amplitude with depth due to the heat tracer.

First, we investigate the ZOP of Plane 2938 parallel to the injection where we expect larger contrasts in permittivity and conductivity due to the proximity to the injection location (Figure 4-2a). The profiles show an overall decrease in permittivity from the background (ε_r=15-25) of up to $\Delta\varepsilon_r$=5 for the entire depth range. The time-lapse amplitude profiles also all show a decrease with respect to the background for the entire depth range. The maximum amplitude profiles show decreasing values from day 2 until day 5 or 6, after which the amplitudes start to increase again to approach the background amplitudes. The difference between the background and the time-lapse permittivity profiles is more prominent deeper than 5.5 m and is much smaller for the shallow measurements at 3.5 m to 4.5 m depth. The permittivity profiles show a decrease from day 2 to day 5 or 6, but do not show a similarly clear increasing pattern after day 7 as the amplitude profiles. An anomalous permittivity profile is day 8, which is unexpectedly similar to the background. This should be considered later during the inversion processing for day 8, i.e., if the ray-based and full-waveform inversions also show similar behaviour as the ZOP permittivity. Note that pre-processing of the data has been double-checked and no errors should be caused by time zero corrections.

There are only 3 datasets for Plane 3834, which is parallel to the injection but farther from the injection borehole: background, day 14, and day 17 (Figure 4-2b). Both the time-lapse permittivity and amplitude profiles are similar and show a decrease relative to the background. The time-lapse permittivity profiles are similar and show a maximum decrease from the background of $\Delta\varepsilon_r$=1.3. Both maximum amplitude profiles also show a decrease relative to the background over the entire depth range.

Plane 3238 is perpendicular to tracer injection, but in the west, where we expect lower tracer flow due to the regional groundwater flow direction as indicated in Figure 3-1b. Similarly to Plane 2938, Plane 3238 has high permittivity profiles for day 8 and especially day 9 (Figure 4-2c). Other than these two anomalous days, the permittivity profiles for day 6 to day 14 are lower than the background and day 28 starts to show recovery towards the background permittivity. The time-lapse trend from the permittivity profiles is unclear for Plane 3238, but the maximum amplitude profiles have a more clear trend. The maximum amplitudes show an initial increase for day 4, decreasing from day 5 to 10, and an increase between days 14, 28, and 37.

The permittivity ZOPs for Plane 3831, perpendicular to tracer flow, shown in Figure 4-2d show a background permittivity lower than the time-lapse profiles. This is the opposite of what is expected, as the presence of the heat tracer should decrease the permittivity. After looking into the details of the dataset, it is concluded that the ZOP for the background dataset of Plane 3831 is unreliable. One explanation for this discrepancy could be measurement errors. Nevertheless, it does not affect the inversion as the MOG data seems to be consistent with the expected response. Similar to Plane 2938 and 3238, the permittivities of day 8 and day 9 are anomalously high. Note that borehole filling effects that may cause a shift in time of the signals are not considered in any ray-based approaches. The maximum amplitude profiles, however, show a similar decrease in amplitude in comparison to the background as Plane 2938, but less prominent. All maximum amplitude profiles for all four planes show 5-6 clear peaks in amplitude indicating some layering in the subsurface.

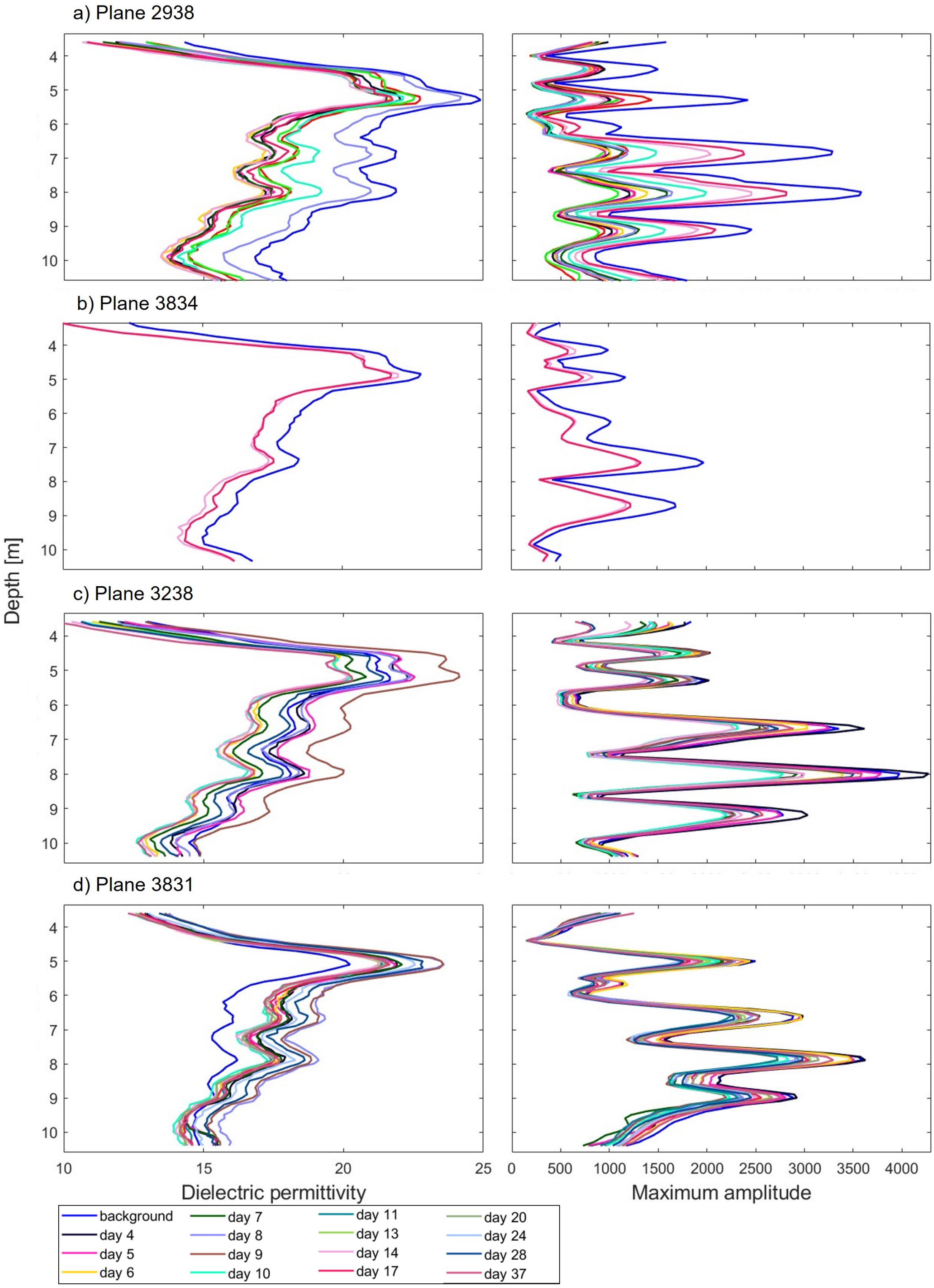

Figure 4-2: Zero offset profiles for the background and all time-lapse datasets for a) Plane 2938, b) Plane 3834, c) Plane 3238, and d) Plane 3831.

4-3 Background FWI

As described in Section 2-2, defining a starting model with ray-based inversion is the first step after filtering and time-zero correcting the data. Note that details for the ray-based inversion and other pre-processing steps are not shown here. It is necessary to test various permittivity starting models to ensure the half-wavelength criterion is met. Since a high contrast in the upper part of the aquifer is expected, we performed the amplitude analysis for the upper layer, where there is low ray coverage, to modify the starting model to improve the FWI fit for the first three transmitters. Starting model tests were first carried out for the background dataset of Plane 2938, which is parallel to the tracer flow and includes the injection borehole (B29).

4-3-1 Amplitude analysis

The amplitude analysis (AA) approach proposed by Klotzsche et al. (2014) and further refined by Zhou et al. (2020) is implemented for the Krauthausen heat tracer experiment for the background data for all four planes to identify any low velocity high permittivity layers that could have caused problems for the ray-based results. As there is minimal clay present at the site, there are no obvious type II waveguides observed and therefore distinction between type I and II is not necessary.

First, the dewowed data are inspected for elongated wave trains and regions of diminished amplitudes and transmitters (MOGs) with identified waveguide characteristics are selected. A trace energy profile for each of these transmitters is plotted in a different colour in Figure 4-3 along with the picked maxima (black crosses) in Figure 4-3a and minima (blue crosses) in Figure 4-3b. The maximum and minimum amplitude picks are then plotted in Figure 4-3c according to the transmitter and receiver depths such that waveguiding layer boundaries can be interpreted. The trace energy maximum picks use an energy threshold of 10^8 and the minimum picks are at least one order of magnitude lower than the maxima, in this case below trace energies of 10^7.

For the 29-38 configuration, where the transmitters are located in B29, two upper boundaries are identified in Figure 4-3c: the first around 3.8 m depth for shallower transmitters that levels out to 3.5 m depth for the deeper transmitters and the second around 3.8-3.9 m that is present for transmitters deeper than 8.7 m. The lower boundary is at 5.0-5.1 m depth. The trace energy maxima range from depths of 3.8-5.8 m for transmitters at 4.1-5.7 m depth. The results are slightly different for the 38-29 configuration in Figure 4-3f: there are two identified boundaries in this upper layer based on the minimum picks. The uppermost boundary is at 3.8 m depth and the other boundary is at 4.4 m depth. The trace energy maxima range from 3.8-5.5 m depth for transmitters at 4-6 m depth. The differences in the AA between reciprocal configurations suggest that the layers are not necessarily horizontal or laterally continuous.

For both semi-reciprocal configurations, the maxima suggest that there are two low velocity layers in this upper region from 4-6 m depth: one at 3.8-4.5 m depth and the other at 4.6-5.6 m depth. These trace energy maxima are seen in all of the transmitters between 3.99 and 5.99 m depth and therefore it is difficult to distinguish separate layers as the waveguiding events are likely interfering with one another. Furthermore, there is some uncertainty with the boundaries for the upper layer minima as they range from receiver depths of 3.5-3.8 m

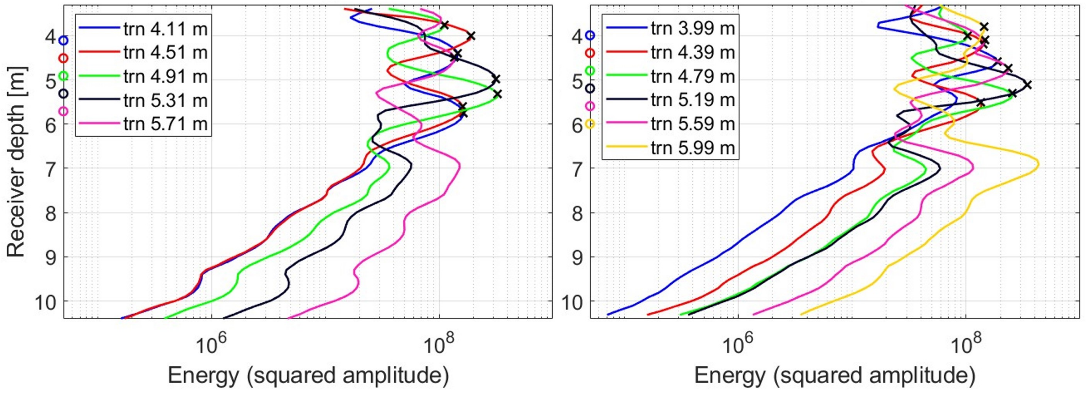

a) Maxima locations, position 29-38

d) Maxima locations, position 38-29

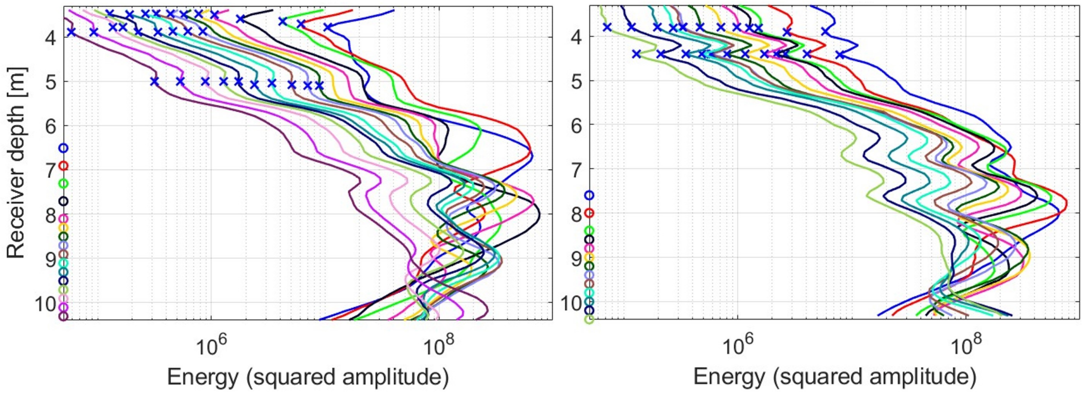

b) Minima locations, position 29-38

e) Minima locations, position 38-29

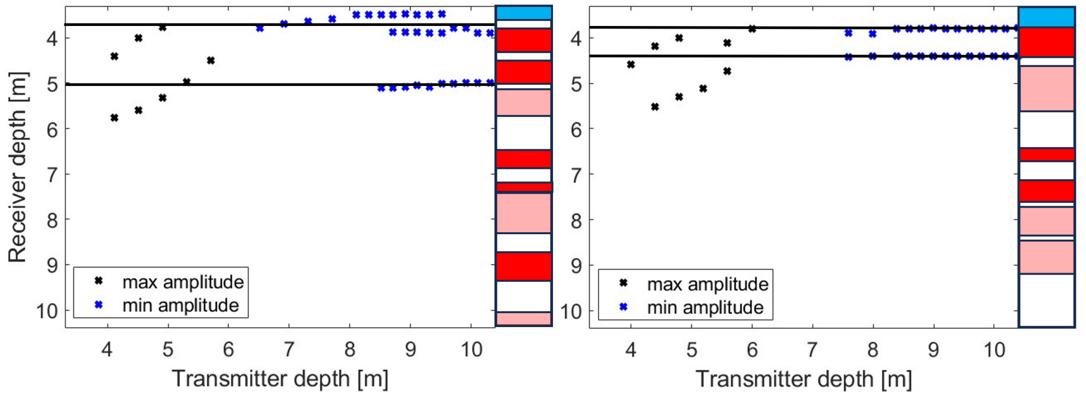

c) Position 29-38, maximum and minimum picks

f) Position 38-29, maximum and minimum picks

Figure 4-3: Amplitude analysis for the background dataset of Plane 2938 in the upper layer. Trace energy profiles for different transmitter depths (colours) in borehole B29 that show clear (a) trace energy maxima and (b) minima. Note that the transmitter depth is plotted as a circle with the corresponding colour. c) Transmitter vs receiver depth plot for the maximum and minimum picks with an interpreted waveguide column including findings from Figure A-1, where blue indicates the upper low permittivity layer, solid red indicates low velocity waveguides constrained with both maximum and minimum picks, and transparent red indicates less constrained low velocity waveguides. d)-f) show the maxima and minima picks for the opposite configuration, with the transmitters in borehole B38.

and 3.8-3.9 m. In these shallow regions, observations might be significantly influenced by waveguiding interference and/or low ray coverage. The latter suggests that the FWI starting model should be tested by adding a layer that potentially extends to 3.5-3.9 m depth.

There are four additional waveguiding structures identified at greater depths using this same approach and the results are shown in Appendix A in Figure A-1. The results from the different semi-reciprocal configurations are again slightly different, indicating non-horizontal or discontinuous waveguides. Some minima that are evident in the 29-38 configuration are not observed in the 38-29 configuration. These structures could be preferential pathways for the heat tracer, which will be confirmed with the FWI results. For the starting model tests, only the findings from the upper layer amplitude analysis are used to improve the data fit for the first few transmitters.

4-3-2 Background starting model tests

In addition to the optimization of the starting models, the FWI perturbation factors and stabilization factors for the ε_r and σ need to be defined to stabilize the inversion. The perturbation factors, which are used in the simultaneous step length calculation (Eq. (2-24) and (2-25)), are first optimized. The ε_r perturbation factor is first tested from 10^{-5} to 10^{-3} while all other parameters are kept constant. The optimal value is determined to be 10^{-4} as the inversion steadily converges with an RMS reduction of around 60% from the starting model within 30 iterations, although changing the values only has a minor effect on the result. The σ perturbation factor is then tested from 0.1 to 10. An optimal value of 10 is chosen since the inversion converges within 20-30 iterations, has a low RMS, and high R^2 values, while factors of 0.1 and 1 need at least 30 iterations and have a higher RMS. Stabilization factors are needed for both the permittivity and conductivity for the gradient preconditioning, which prevent artifacts near the antennae (Klotzsche et al., 2019b). An optimal value of 50 is determined for both the permittivity and conductivity stabilization factors, however, only minor differences are observed between tests, similar to the findings of Klotzsche et al. (2019b). Note that the following starting model tests are performed with the optimized input parameters as described above. The unsaturated zone is included in all starting models with ε_r=4.969 above 2.52 m.

We test five different starting models using the information from the AA for the Plane 2938 background dataset (Figure 4-4). For each starting model, an update of the effective source wavelet is performed since changes in the permittivity model cause small effects in the 2D transformed data and the source wavelet (Eq. (2-17) and Figure 4-5). This effective source wavelet now accounts for borehole filling, antennae coupling, and finite length antennae, which was not possible for the ray-based approaches, including the ZOP analysis and the ray-based starting models. Note that a homogeneous conductivity starting model of $\sigma = 14$ mS/m is used for all inversions as this was identified by Haruzi (2023), Klotzsche et al. (2010), and Zhou et al. (2021) as the optimal conductivity starting model strategy.

First, the ray-based permittivity inversion result is used as the starting model without the addition of any layers; this is referred to as SM1 (Figure 4-4). For SM1, there were some differences between the observed and the FWI modelled data, particularly at early times for the first few transmitters (not shown). The starting model was then refined (SM2) in an attempt to better fit the observed data for these shallow transmitters by including two

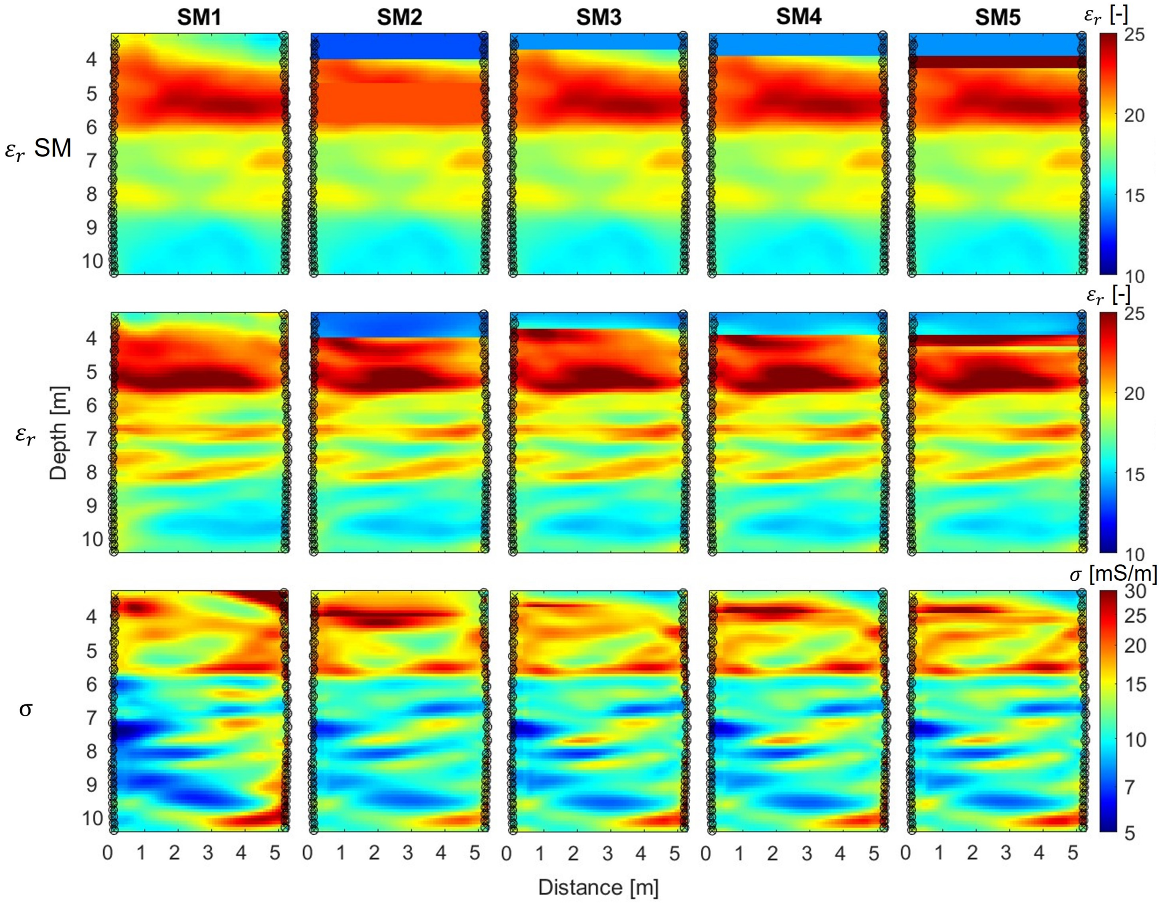

Figure 4-4: FWI results for the background dataset of Plane 2938 with different layers added to the starting model. The top row shows the different adapted permittivity starting models, the middle row the final FWI permittivity, and the bottom the final FWI conductivity result. Note the logarithmic scale for the conductivity. The transmitter and receiver locations are indicated with circles and crosses, respectively.

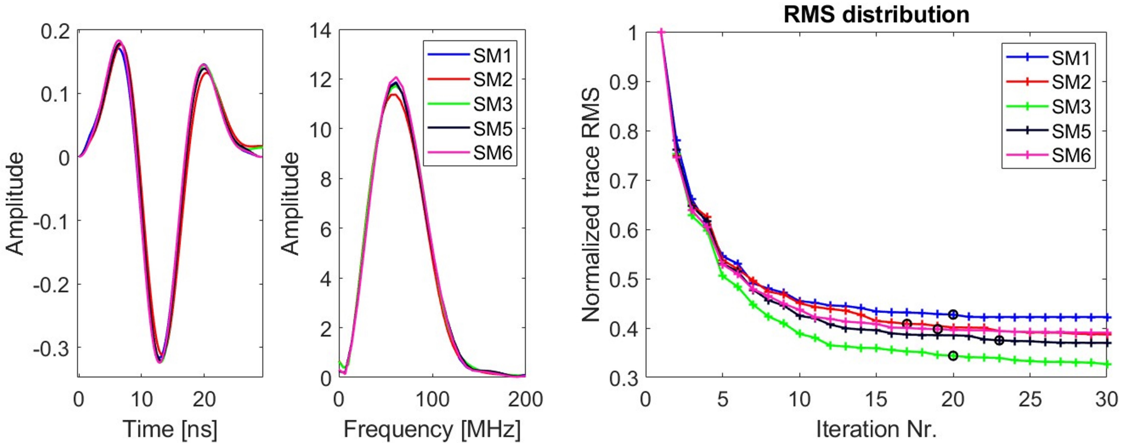

Figure 4-5: Source wavelets (left), corresponding amplitude spectra (middle), and root-mean-squared error (RMS) distributions (right), normalized to 1, for each of the starting model tests for the background dataset of Plane 2938. The black circles in the RMS distributions indicate the final iterations chosen for each result based on the stopping criteria.

homogeneous layers: an upper layer extending to 3.96 m with $\varepsilon_r = 13$ and a layer from 4.77-5.85 m with $\varepsilon_r = 22$. The high permittivity layer in SM2 was added to test if the high permittivity zone at approximately 5.5 m in the FWI result with SM1 is being driven by the starting model. The FWI permittivity result using SM2 shown in Figure 4-4 again contains the high permittivity zone near 5.5 m depth, which suggests that it is not being driven by the starting model. The upper low permittivity layer is still present in the FWI result and it has improved the RMS, as shown in Figure 4-5, but it is a higher permittivity of 14-15. Interesting in this result is that with the addition of the low permittivity layer, there seem to be two more distinct high permittivity layers at approximately 4.5 and 5.5 m. This is also seen in the amplitude analysis as two waveguides were observed at these depths (Figure 4-3). To investigate this feature further, the starting model is again modified to have a homogeneous layer with a permittivity of 14 that extends only to a depth of 3.69 m (SM3) rather than 3.96 m (SM2). In the corresponding result, the two high permittivity layers between 4 and 6 m are still observed but are less distinct as with SM2. The result using SM3 (Figure 4-4) has a much lower RMS (Figure 4-5 and Table 4-1) than with SM1 or SM2. This reduction in the RMS could originate from the permittivity change or the reduced thickness of the homogeneous layer. Due to the ambiguity in picking the trace energy minima, more upper layer thicknesses are tested. SM4 extends this ε_r=14 layer to 3.87 m but has a higher RMS and a lower correlation coefficient, R^2, than SM3 (Table 4-1). The FWI results for all of the layer thicknesses tested still show some differences between the measured and full-waveform modelled data for the first three transmitters. To try to fit this data, we test an additional high permittivity layer (ε_r=25) directly below the top layer where the low velocity waveguide is present. This is implemented for three different thickness combinations of the two layers, however, as no improvements are observed with these two-layer models, only one realization is presented for illustrative purposes (SM5).

These starting model tests conclude that the FWI result using SM3 is the best as it has the lowest RMS, the highest R^2, the lowest mean permittivity remaining gradient (Table 4-

Table 4-1: Comparison of FWI results for different starting models for the background dataset of Plane 2938. The remaining gradients are the mean of the absolute value of the smoothed permittivity and conductivity gradients of the final iteration model. The trace root-mean-squared error (RMS), the RMS normalized to the starting model, as well as the correlation coefficient (R^2) between the observed and FWI modelled data are given for the final iteration.

Starting model	Final iteration	Grad. ε mean $*10^4$	Grad. σ mean $*10^{-5}$	Final RMS $*10^{-6}$	Final RMS norm. (%)	R^2
SM1	20	6.85	8.74	1.36	42.2	0.900
SM2	17	6.40	10.4	1.38	40.8	0.900
SM3	**20**	**5.07**	**9.92**	**1.07**	**34.1**	**0.939**
SM4	23	5.91	19.2	1.19	37.4	0.924
SM5	19	7.42	11.8	1.21	39.6	0.922

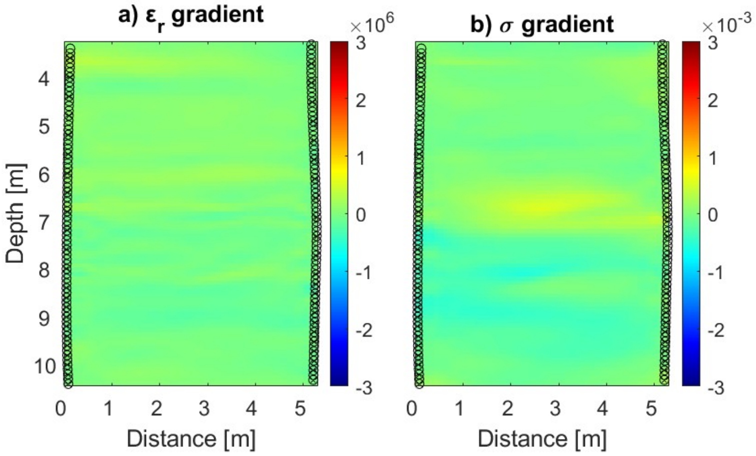

Figure 4-6: Smoothed gradient for the a) relative permittivity and b) electrical conductivity of the final FWI result for the background dataset of Plane 2938 using SM3.

1), and fits the observed data in the first few transmitters the best of all tested starting model strategies. The smoothed gradients at the final iteration (20) for ε_r and σ show minimal remaining gradients (Figure 4-6). It is clear that the FWI modelled data for the best result is fitting the measured data well with correlation coefficients higher than 0.84 for each MOG (Figure 4-7 for transmitters at 3.99 m, 6.79 m, and 9.99 m depth in B29). Note the waveguiding event for the transmitter at 6.79 m depth showing an elongated wavetrain is well fitted with the modelled data based on the FWI results. This homogeneous layer with ε_r=14 extending to 3.69 m depth is also implemented in the starting models for the time-lapse datasets. For the other planes, similar tests are performed (not shown) with various thicknesses of this layer for the background datasets and then implemented for all time-lapse datasets from each plane. For Plane 3831, the layer extends slightly deeper and therefore there is a higher ray coverage allowing the layer to be recovered in the FWI. Therefore, no additional layer is added for this plane.

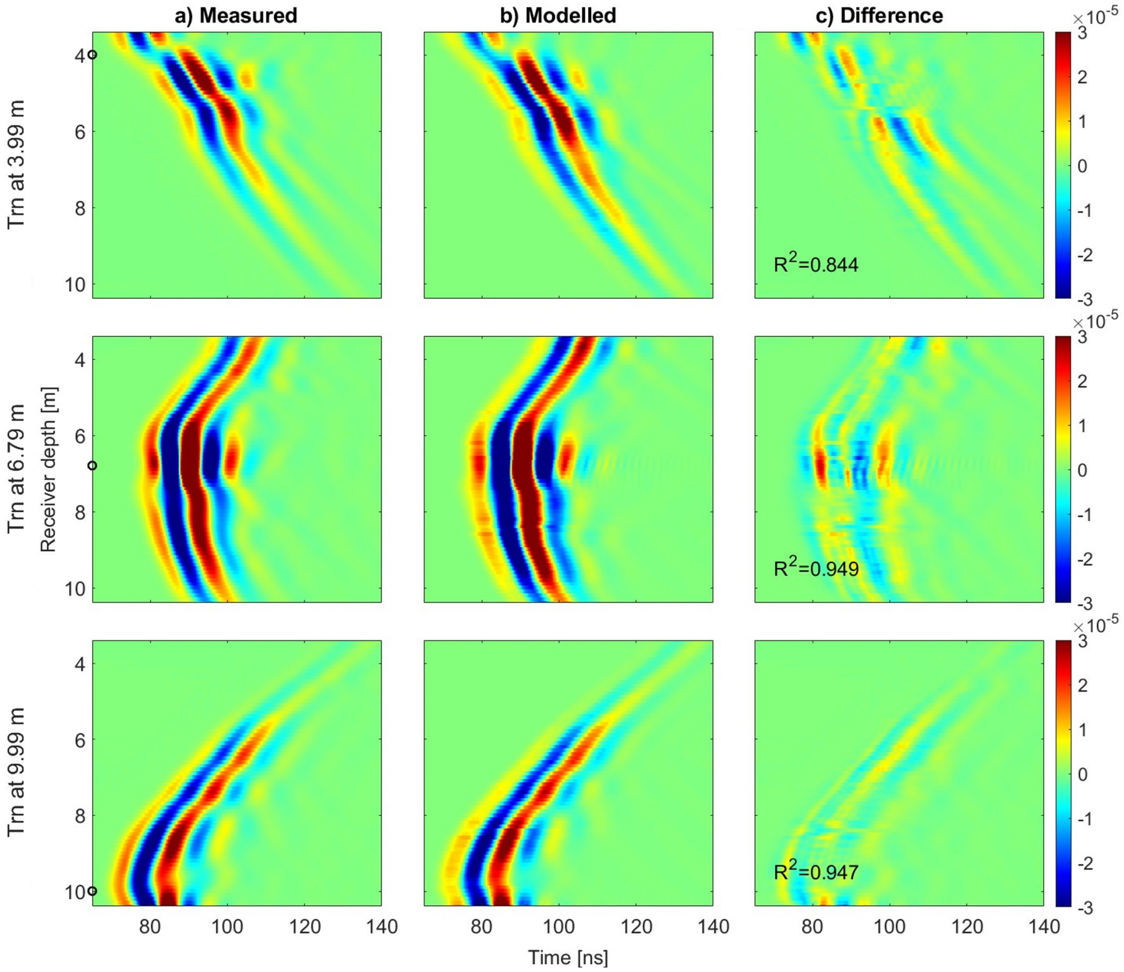

Figure 4-7: a) Measured data, b) modelled data based on the final FWI results, and c) the difference between the measured and modelled data for 3 different transmitters in the background dataset of Plane 2938 using SM3. The black circles on the depth axes indicate the depth of each transmitter. The R^2 values between the measured and modelled data are indicated in the difference plots.

4-4 Time-lapse FWI

4-4-1 Time-lapse starting model tests

In a study conducted by Haruzi (2023) with a salt tracer at the Krauthausen test site, the optimal starting model for the time-lapse datasets was the background FWI permittivity model and a homogeneous conductivity model with σ=14 mS/m. With a salt tracer, the expected changes in properties are mostly related to the conductivity and should have little to no effect on the permittivity over the course of the experiment and therefore taking the background as the starting model is appropriate. In this heat tracer experiment, however, changes in both the permittivity and the conductivity are expected in time-lapse datasets. It therefore might not be feasible to use the background FWI as a starting model as it might not satisfy the half-wavelength criterion. The optimal time-lapse starting model strategy is determined by performing tests for Plane 2938, which includes the injection borehole and should therefore have the greatest contrast in properties over the course of the experiment in comparison to the other planes. We assume that this strategy is then applicable to all remaining planes.

For the time-lapse datasets, the traces are normalized to the global maximum of the background dataset to avoid instrument differences reflected in the source wavelets. The same inversion settings as for the background FWI are used: $\delta\varepsilon$ of 10^{-4}, $\delta\sigma$ of 10^{1}, and stabilization factors of 50. Since Haruzi et al. (2022) showed that it is always best to use a homogeneous starting model for conductivities, we keep this constant similar to the background dataset and only investigate the effect of the permittivity starting model.

Three starting models for the first time-lapse dataset are tested, acquired the day after injection on day 2 (Figure 4-8). First, the ray-based permittivity of day 2 (S1) is tested with the same upper layer determined for the background dataset added. Second, the FWI permittivity result of iteration 4 of the background is tested. Finally, the FWI permittivity result (iteration 20) of the background, similar to the approach used by Haruzi (2023) is tested. The results for S1 show proper convergence (Figure 4-9) and the R^2 value of 0.909 suggests a good agreement between observed and FWI modelled traces (Table 4-2). The permittivity result for S2 is almost identical to the starting model. The inversion converges after only 4 iterations and the RMS error is only reduced from the starting model by 14%, although one of the criterion for stopping the inversion is a reduction of 50% (Figure 4-9). S3 shows a similar behaviour: the FWI permittivity is the same as the starting model, it converges after 4 iterations, and the RMS error is only reduced by 18% (Figure 4-8 and Figure 4-9). However, the total trace RMS error is comparably low, suggesting that the inversion converged to a local minimum (Table 4-2). This is most likely due to the starting model not producing synthetic traces that fit the observed traces within half of a wavelength. The source wavelets for S2 and S3 are slightly shifted in time and have a lower amplitude than the source wavelet for S1 (Figure 4-9). Note that other perturbation factors are tested for S2 and S3, however, they still fail to converge. S1 produces the only feasible result and is the best starting model strategy. For the S1 strategy, two different source wavelets are also tested: the first determined using two source wavelet corrections, as described in Section 2-2-2, and the second determined by applying only one source wavelet correction with the final background (Plane 2938) source wavelet as input. We found that both source wavelets are identical and therefore we use the latter method for the rest of the time-lapse datasets as it saves significant processing time.

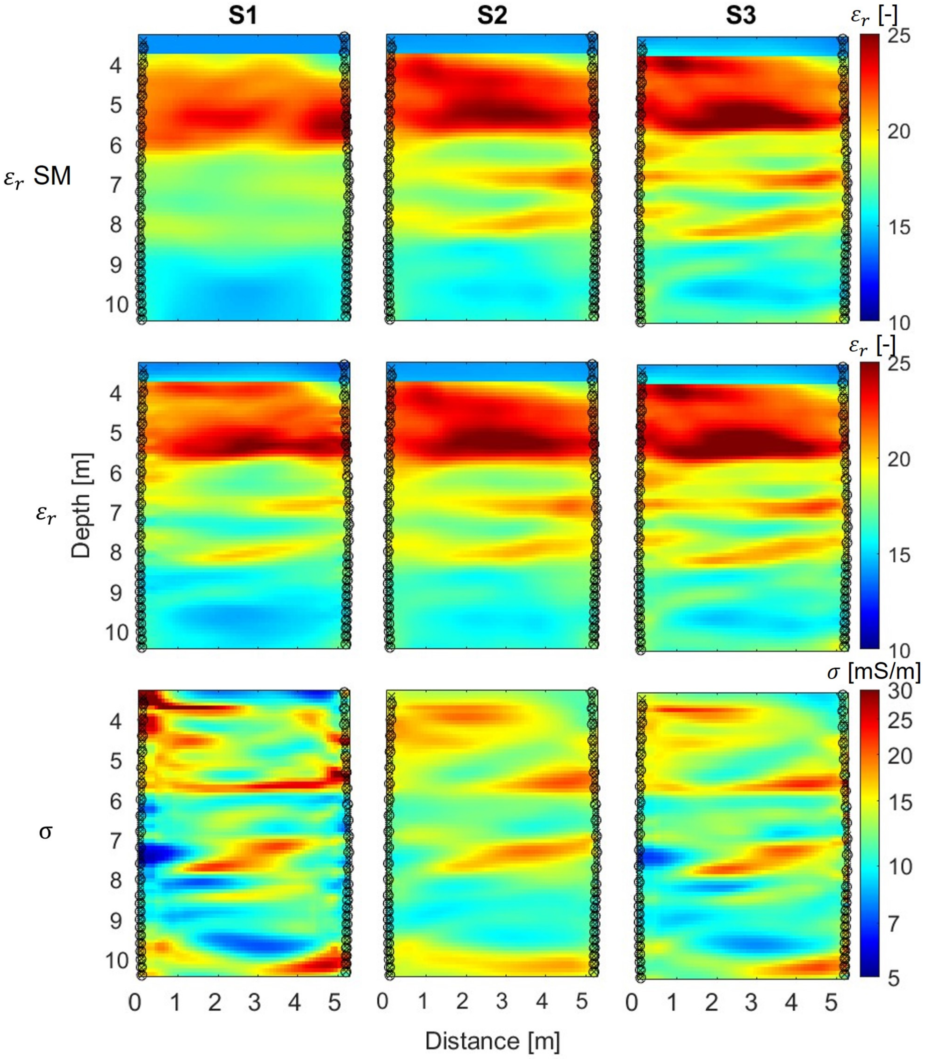

Figure 4-8: FWI results for the day 2 dataset of Plane 2938 using three different starting model strategies. The top row shows the different starting models: S1 is the ray-based permittivity for day 2, S2 is the background FWI permittivity result at iteration 4, and S3 is the background FWI permittivity result at the final iteration. The middle row shows the final FWI permittivity and the bottom the final FWI conductivity result. Note the logarithmic scale for the conductivity. The transmitter and receiver locations are indicated with circles and crosses, respectively.

Since the heat tracer is introducing changes in both permittivity and conductivity, we have found that it is not feasible to use the background FWI permittivity as the time-lapse starting model because the half-wavelength criterion is not met. Additionally, the results with the ray-based starting model show a decrease in permittivity, indicating an increase in velocity, in the high porosity waveguiding layers that were identified in the background FWI result and the amplitude analysis. This behaviour is in accordance with the expected response of the heat tracer. This concludes that the ray-based inversion results for the permittivity of each time-lapse dataset with the addition of the homogeneous ε_r=14 upper layer will therefore be used as starting models for the FWI of each time-lapse dataset.

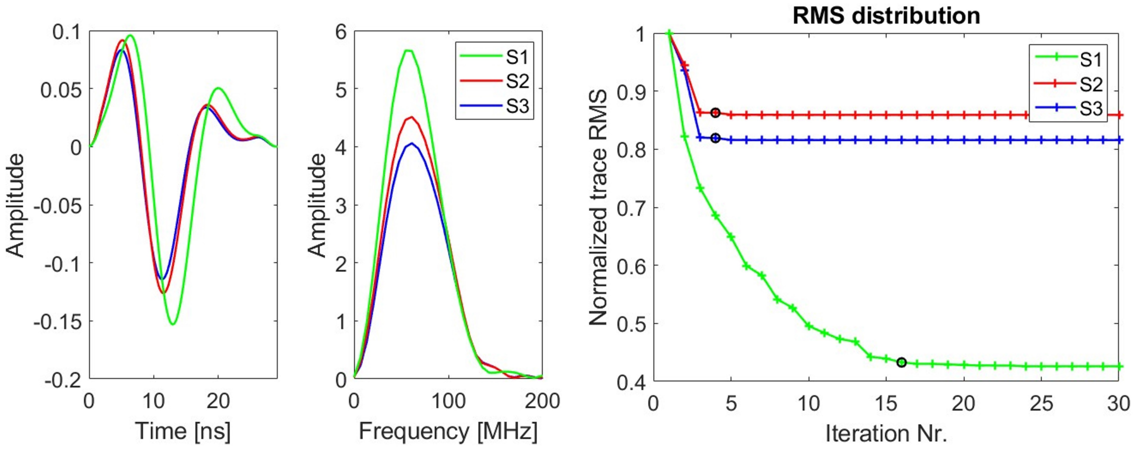

Figure 4-9: Source wavelets (left), corresponding amplitude spectra (middle), and RMS distributions (right), normalized to 1, for each of the starting model tests for the day 2 dataset of Plane 2938. The black circles in the RMS distributions indicate the final iterations chosen for each result based on the stopping criteria.

Table 4-2: Comparison of FWI results for different starting model strategies for the day 2 dataset of Plane 2938. The remaining gradients are the mean of the absolute value of the smoothed permittivity and conductivity gradients of the final iteration model. The trace root-mean-squared error (RMS), the RMS normalized to the starting model, as well as the correlation coefficient (R^2) between the observed and FWI modelled data are given for the final iteration.

Starting model	Final iteration	Grad. ε mean $*10^4$	Grad. σ mean $*10^{-5}$	Final RMS $*10^{-6}$	Final RMS norm. (%)	R^2
S1	**16**	**2.93**	**2.52**	**0.541**	**43.0**	**0.909**
S2	4	4.31	3.87	0.710	86.0	0.843
S3	4	8.38	6.33	0.598	81.6	0.885

4-4-2 Time-lapse FWI results

As shown in Section 4-4-1, we need to consider the ray-based starting model strategy with adaptations using the AA for time-lapse datasets. This starting model strategy is applied to the rest of the time-lapse datasets for Plane 2938 (Figure 4-10). The perturbation and stabilization factors needed to be adapted for the time-lapse datasets such that the FWI convergence criteria were fulfilled for all results (Table A-1). The source wavelet correction is applied once for each time-lapse dataset using the final source wavelet from the background (Plane 2938) as input, as established in Section 4-4-1.

From the ray-based results of the different days, shown in the top row of Figure 4-10, there is a generally decreasing trend in permittivity with respect to the background over time (the results for the other planes can be found in Appendix A). The time-lapse FWI permittivity results in the middle row of Figure 4-10 show an overall decrease in permittivity with time, prominently in the upper layer from 4-6 m depth and in the waveguiding layers at around 6.7-7.0 m depth and at 7.6-8.1 m depth. The FWI permittivity result for day 8 is anomalously high, similar to its permittivity ZOP in Figure 4-2. The result is similar to the background FWI result and does not align with the time-lapse trend expected and observed with the other datasets. This could potentially be caused by systematic equipment problems, by other external conditions in the field that were not noted, or by borehole filling effects. However, the exact reason could not be identified within this study, while processing errors are excluded (they have been double-checked). Therefore, we adapted this issue by using the ray-based starting model from day 7 for day 8. The new effective source wavelet for day 8 using the day 7 starting model is shifted in time in comparison to all other datasets (Figure 4-11) indicating that the updated source wavelet compensates for the time shift in the data. The updated FWI results (Figure 4-10) now follow the overall trend caused by the tracer. Note that this effect was observed for all day 8 and 9 datasets for the other planes and therefore we applied this approach to all of them. The time-lapse FWI conductivity results for Plane 2938 (Figure 4-10) show an overall increase with respect to the background, as expected. The largest increases in conductivity are observed at around 5.6-6.0 m depth, and below 7 m depth in the center of the plane.

The three other planes (3834, 3238, and 3831) were processed using the same workflow, with the same source wavelet correction and starting model strategy as described for Plane 2938. All results fulfill the FWI convergence criteria (Table A-2-A-4). Similarly to Plane 2938, the other planes also show an overall decrease in permittivity and an increase in conductivity with respect to the background over time (Figure A-2 to A-5). The time-lapse FWI permittivity and conductivity results do show a decrease and increase, respectively, relative to the background, but do not show strong differences between each time-lapse day. Therefore, the analysis of the FWI results is more qualitative.

To better visualize and quantify the changes over time, we subtract the background from the time-lapse FWI models. Differences due to the presence of the heat are negative for permittivity and positive for conductivity. Plane 2938 shows negative differences in permittivity of up to $\Delta\varepsilon_r$=5 in the upper layer from 4-5.6 m that appear to increase in magnitude from day 3 to 10, after which the magnitude decreases from day 14 to 17 (Figure 4-12). There is a thin layer with a positive permittivity anomaly ($\Delta\varepsilon_r$=1) directly below the upper layer at approximately 5.6 to 5.9 m depth. Below this thin layer, there is an overall negative difference in permittivity to 10.5 m depth over the entire plane of up to $\Delta\varepsilon_r$=3, with some layers exhibiting a stronger decrease than others. The conductivity differences for Plane 2938 (Figure 4-12) show a strong increase from day 2 to 7 at 5.7 to 6 m depth (up to $\Delta\sigma$=15 mS/m), after which the magnitude of the anomaly decreases. There is also layering of positive conductivity anomalies from 6 m to depth (up to $\Delta\sigma$=5 mS/m). Plane 3834, parallel to tracer flow, shows an overall negative difference in permittivity over the entire plane for both days 14 and 17 and a maximum decrease of up to $\Delta\varepsilon_r$=2 at around 5 m depth (Figure A-6). The conductivity difference shows a positive conductivity anomaly of up to $\Delta\sigma$=5 mS/m from 5.5-9 m depth

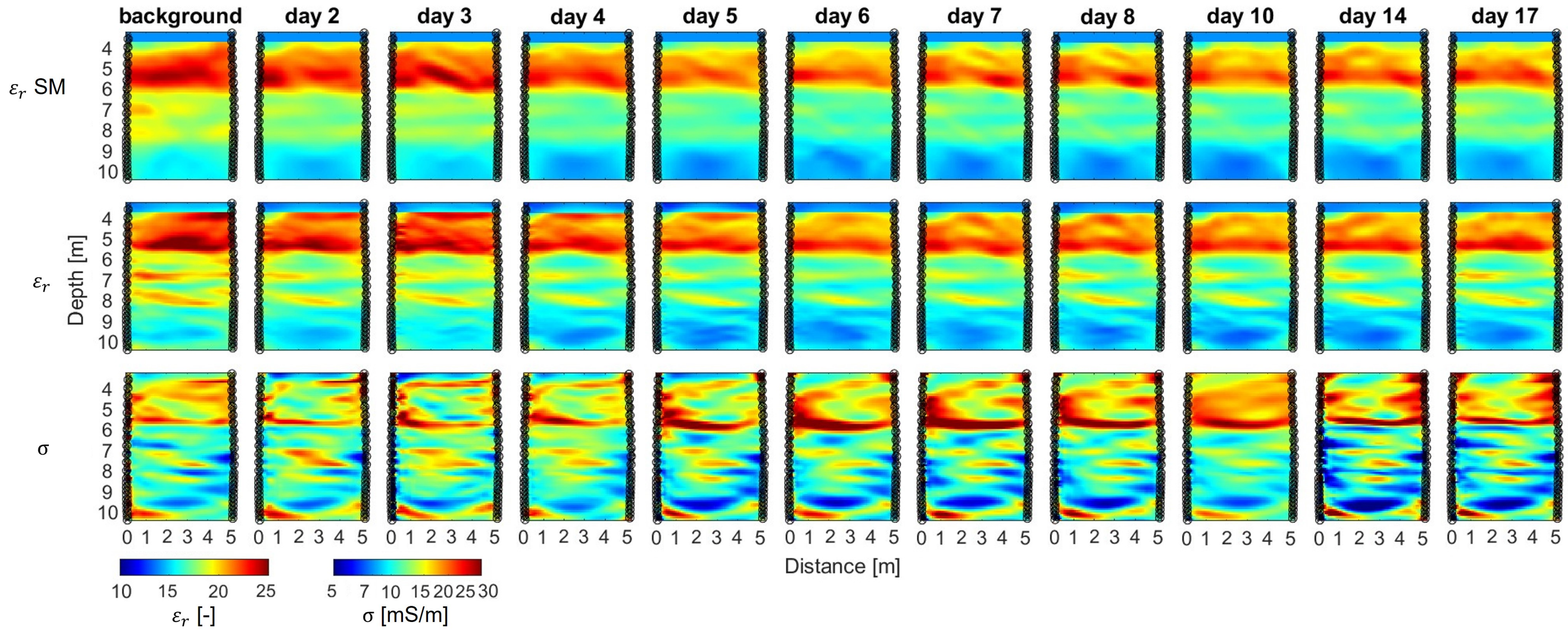

Figure 4-10: FWI results for all datasets of Plane 2938. The top row shows the permittivity starting model for the background and each time-lapse dataset, the middle row the final FWI permittivity, and the bottom the final FWI conductivity result. Note the logarithmic scale for the conductivity. The transmitter and receiver locations are indicated with circles and crosses, respectively.

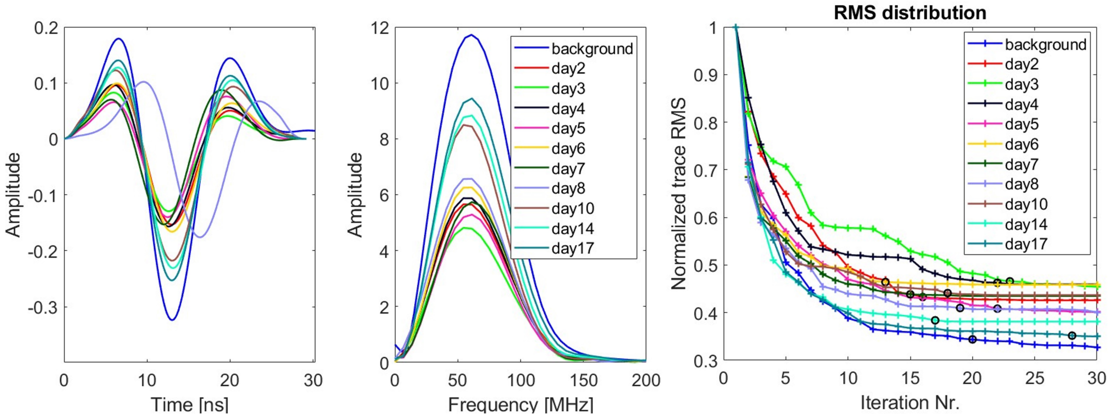

Figure 4-11: Source wavelets (left), corresponding amplitude spectra (middle), and RMS distributions (right), normalized to 1, for each of the time-lapse datasets for Plane 2938. The black circles in the RMS distributions indicate the final iterations chosen for each result based on the stopping criteria.

in the center of the plane. Both Plane 3238 and 3831, perpendicular to tracer flow, show similar anomalies. Plane 3238 has an overall negative permittivity difference over the entire plane of up to $\Delta\varepsilon_r$=2, with minimal differences in magnitude between time-lapse days, while the conductivity difference is mainly in the center of the plane from 6.2-9.2 m depth with magnitudes of around $\Delta\sigma$=5 mS/m and the largest difference on day 10 with $\Delta\sigma$=10 mS/m (Figure A-7). Additionally to the anomalies observed for Plane 3238, Plane 3831 also has an increase in conductivity in the upper layer until 3.8 m depth, which is especially strong for day 6 and 7 (up to $\Delta\sigma$=15 mS/m) (Figure A-8). The time-lapse data for Plane 3831 were measured until day 37 and we observe decreased magnitudes in the permittivity differences for days 24 and 28 (Figure A-9). Overall, the structure of the anomalies in the difference plots for each plane are consistent and mainly show differences in the magnitude between time-lapse datasets.

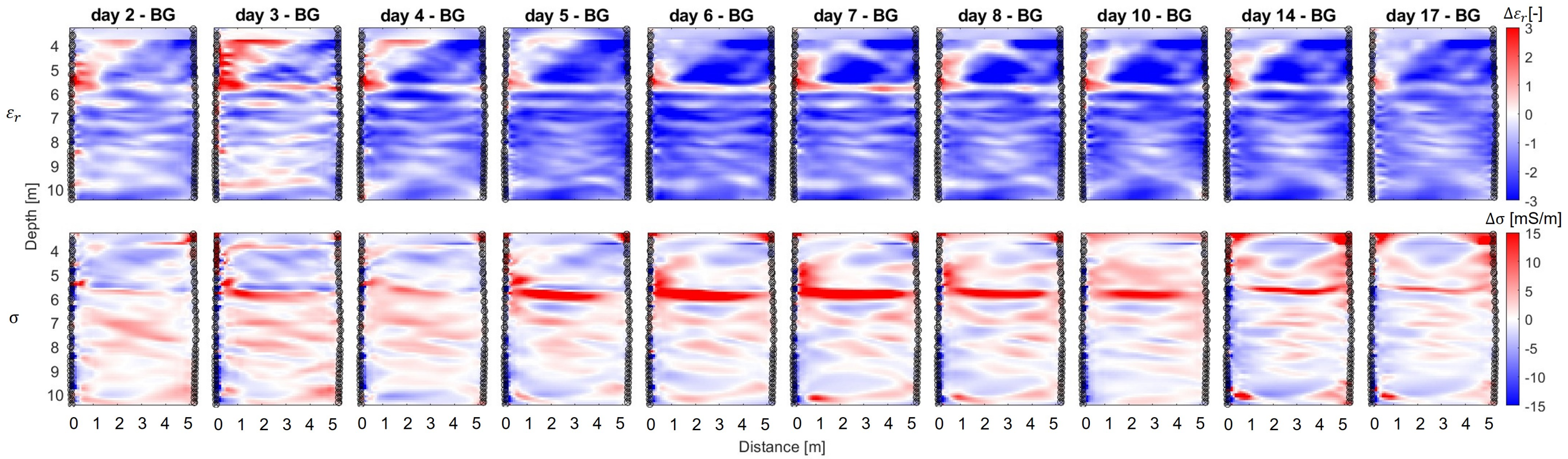

Figure 4-12: Time-lapse difference FWI results with respect to the background for Plane 2938. The top row shows the FWI permittivity and the bottom row the FWI conductivity with the background FWI subtracted for each time-lapse dataset (columns).

4-5 Comparison of results

The FWI background permittivity and conductivity models for all four planes are visualized in 3D (Figure 4-13). There are several layers observed in the permittivity sections that appear to be laterally continuous between all planes. These layers coincide with the identified waveguides at around 6.7-7.0 m and 7.6-8.1 m depth (Figure A-1). The conductivity models show a higher conductivity layer extending to approximately 5.6 m depth. The results are consistent with previous studies (Zhou et al., 2021), confirming the used workflow.

a) Permittivity

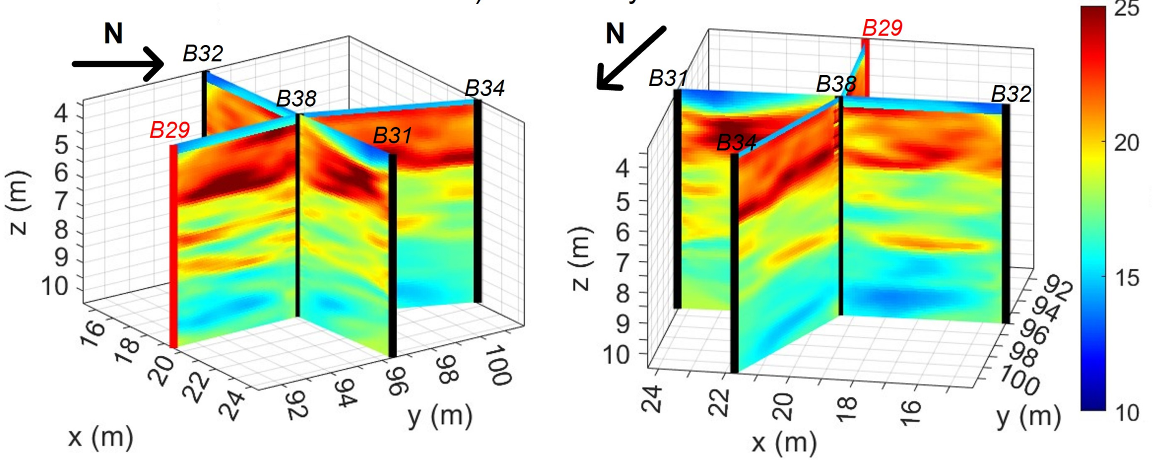

b) Conductivity

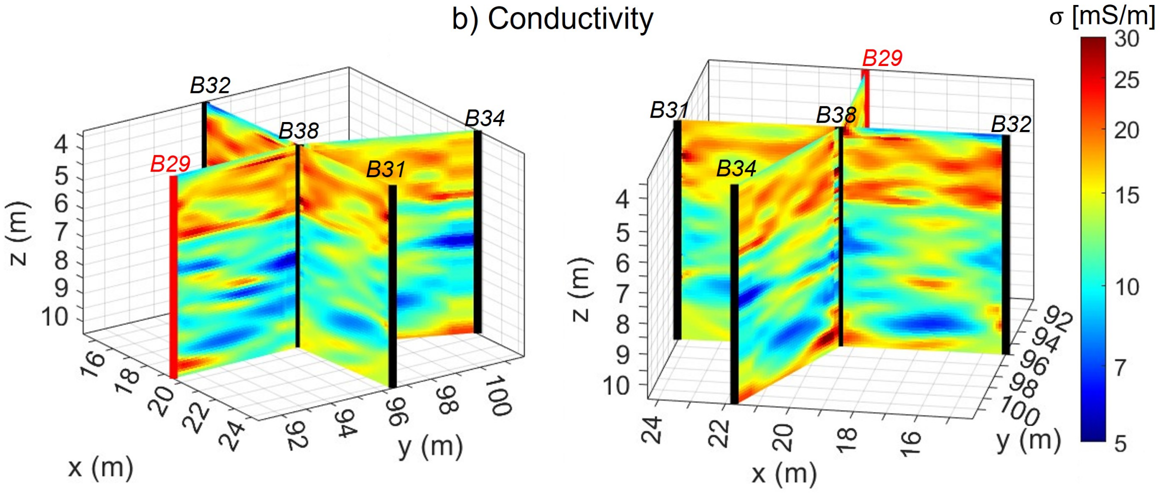

Figure 4-13: Three-dimensional plot in the Krauthausen reference coordinate system of the a) permittivity and b) conductivity FWI results for the background datasets of all four planes. The red vertical line indicates the injection borehole (B29) and the black vertical lines indicate the other boreholes with their corresponding numbers.

Comparing the difference plots for days 5, 7, and 10 (Figure 4-14), only minor differences between time-lapse datasets are observed. Note that differences due to the presence of the heat are negative for permittivity and positive for conductivity. The 32-38-31 cross-section (Figure 4-14) shows minor changes in permittivity between time-lapse datasets; they all show an overall decrease across the entire plane of up to $\Delta\varepsilon$=3 with respect to the background. The

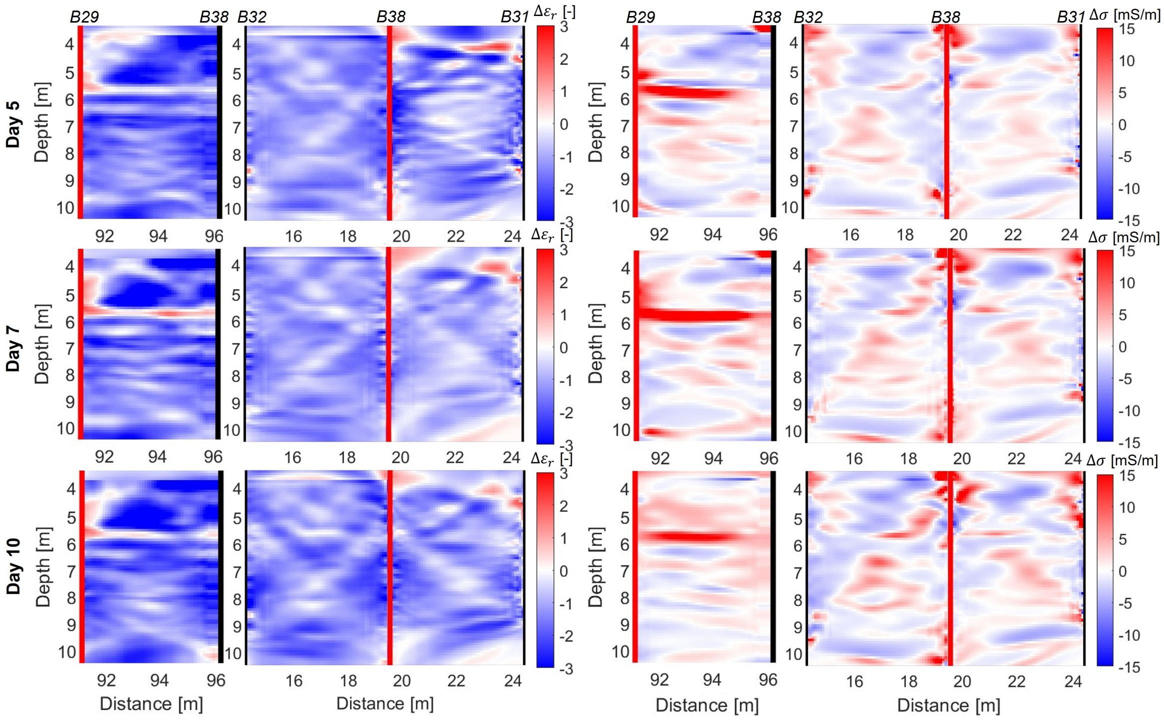

Figure 4-14: Time-lapse FWI difference results with respect to the background for permittivity (left) and conductivity (right) for days 5, 7, and 10 (rows). The cross-sections are 29-38 and 32-38-31, with the borehole names indicated at the top. Note that the background FWI model has been subtracted from every time-lapse FWI model.

differences in permittivity are primarily observed in Plane 2938, where a stronger decrease in the upper layer from 4-5.8 m depth can be observed. At day 7, the negative anomaly seems to split into two layers, following the waveguiding layers that were identified in this upper layer. The anomaly does not seem to be connected to B29. A thin layer is located at 5.8-6 m depth that shows a positive difference, underlain by layers with slightly negative to no difference. Similarly to the permittivity, the conductivity cross-section with B32-B38-B31 shows minor changes between days. The region with the highest increase in conductivity for this cross-section is in the middle of each plane at depths from 6-9 m, with an increase of up to $\Delta\sigma$=5 mS/m. There is also an increase of up to $\Delta\sigma$=8 mS/m in the upper 4-6 m layer closer to the boreholes for all three time-lapse days. For Plane 2938, there is a strong horizontal positive conductivity anomaly at around 5.8 m depth that does not reach B38 at day 5, but seems to connect to B38 at day 7. The anomaly then weakens again at day 10. With the presence of the heat, we would expect a decrease in permittivity in that region, but this is not observed in the data. This is further discussed in the following section.

Chapter 5

Discussion

On the basis of the FWI time-lapse data, we were able to detect changes in permittivity and conductivity over time. Nevertheless, some aspects must be considered in more detail before the final interpretation of the results.

5-1 Investigation of Plane 2938 anomaly

The high conductivity anomaly located at approximately 5.6-6 m depth observed in the difference plots for Plane 2938 in Figure 4-14 and in Figure 4-12 corresponds to an increase in permittivity, which is opposite to the expected behaviour caused by the heat tracer. To understand the cause of this discrepancy, the data are investigated in more detail and various tests are performed.

As a first step, we take a closer look at the traces related to this domain. Note that for the inversion a high correlation coefficient was achieved (Table A-1), however, this is calculated for the entire dataset. To ensure that the FWI results provide modelled data that also fit the measured data well in this region, we calculated the difference between the measured and FWI modelled data for transmitters in this region (5.31-6.11 m depth) for both the background and day 5 datasets (Figure 5-1). The measured data for day 5 show a significant decrease in amplitude overall, especially at depths from 5.5-6 m where the high conductivity anomaly is observed (black dotted lines). Interestingly, the background FWI modelled data have R^2 values higher than 0.9, while for day 5 the transmitter at 5.71 m has an R^2 of 0.651. This suggests that the FWI modelled data have a good fit in this region for the background dataset and the introduction of the heat tracer causes a misfit in this region for the time-lapse datasets.

Since the heat tracer causes this anomaly, we check for cycle skipping for these transmitters and for the reciprocal transmitters for day 5 (Figure 5-2). There is a significant misfit between the modelled and measured traces, indicated by the blue ellipses, for transmitters at 5.31 and 5.71 m depth in B29 and at 5.593 and 5.993 m depth in B38. This misfit is observed at

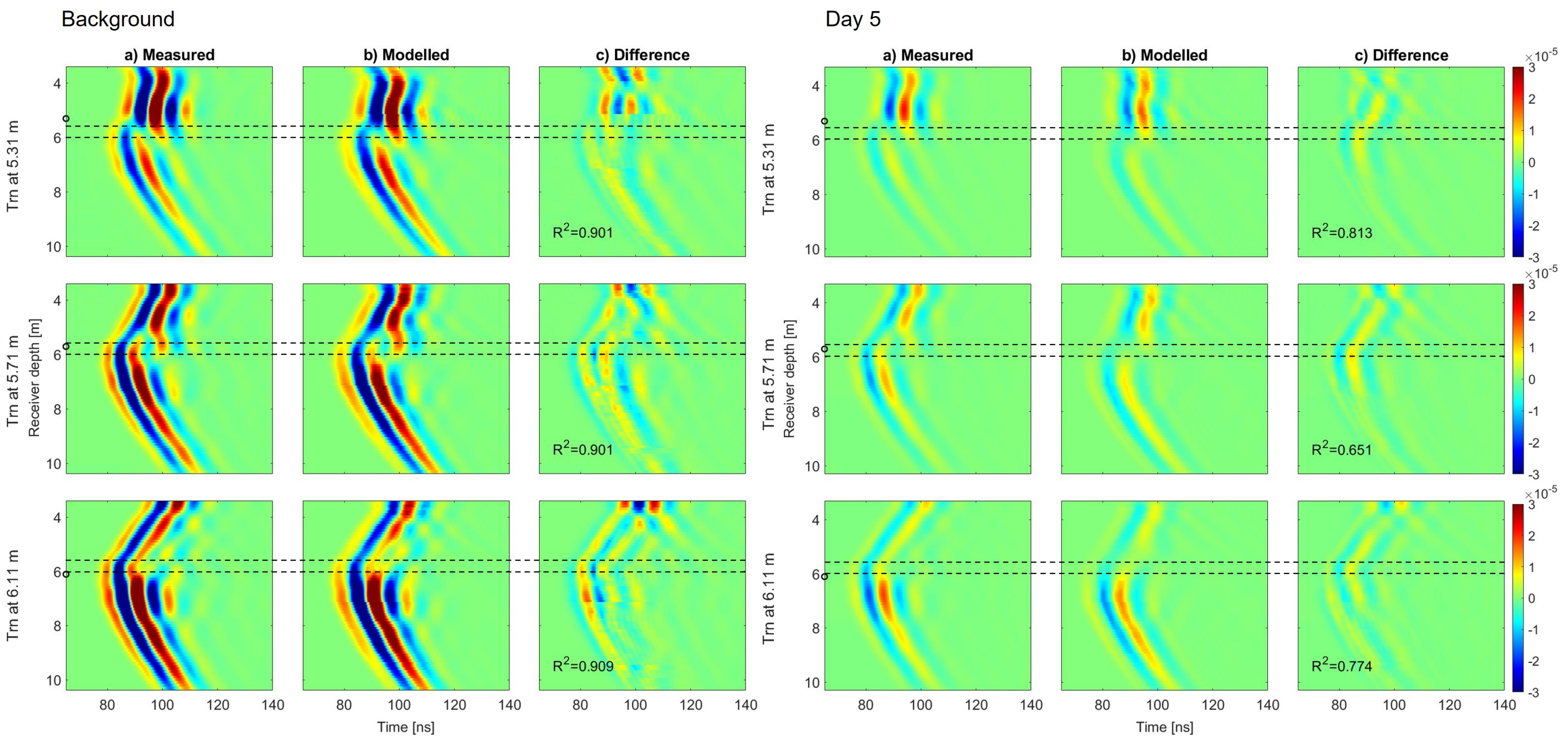

Figure 5-1: a) Measured data, b) modelled data based on the final FWI results, and c) the difference between the measured and modelled data for 3 different transmitters located in B29 in the background (left) and the day 5 (right) dataset of Plane 2938. The black circles on the depth axes indicate the depth of each transmitter and the black dashed lines indicate the location of the high conductivity anomaly. The R^2 between the measured and modelled data is indicated in the difference plots.

receiver depths ranging from 4.8-6.3 m. The amplitudes are significantly lower for the time-lapse datasets in comparison to the background and therefore the misfit in this region, which is only present for less than 15 traces at four transmitters, does not significantly affect the overall RMS, gradient calculation, or R^2 value. The misfit was therefore not detected during the inversion of each dataset and this anomaly is only clearly recognized in the difference plots where the increase in conductivity is not corresponding to a decrease in permittivity. When the inversion fails to fit the permittivity, it overshoots the conductivity to compensate since the amplitudes are quite low, resulting in a strong positive conductivity anomaly for all of the time-lapse datasets. The inversion algorithm could be improved by implementing an adaptive cost function that weights high amplitudes higher than low amplitudes to avoid over-shooting the conductivity.

The misfit observed in this region for day 5 and other time-lapse datasets for Plane 2938 is not present for the background data (Figure 5-3). The measured data for transmitters a), b), and d) in Figure 5-2 and Figure 5-3 show high frequency multiples, indicating reverberations in a waveguiding structure. Furthermore, the data differences between semi-reciprocal measurements indicate a laterally discontinuous feature (Figure 5-2). Since these multiples are fit well for the background data and no clear events in previous studies were observed (Zhou et al., 2021; Haruzi, 2023), the presence of the heat tracer is likely changing the characteristics of the waveguide and the FWI then fails to fit them. To better understand the physical cause of this, we test adding different features in the starting model at 5.8-6 m for day 5. Layers with thicknesses of 9, 18, 27, and 36 cm and permittivities of 12, 15, and 25 are tested in addition to a lense structure with a permittivity of 15; the results are shown in Appendix A in Figure A-10. The misfit is only slightly improved by adding a layer from 5.85-6.21 m depth (Test 1) and by adding the lens (Test 5), however, the structure is likely more complex. If the layer or feature is very thin with a high contrast in properties directly below the high permittivity sand layer, the FWI might not be able to resolve it. The data have a central frequency of 60 MHz (Figure 4-11), which translates to wavelengths between 1-1.3 m for typical permittivities of ε_r=15-25 ($\lambda = v/f_c$ and Eq. (2-13)). Additionally, there is a lack of vertically travelling rays with crosshole GPR and therefore separate features can, in some cases, be recovered as horizontally continuous. This occurs in the numerical salt tracer study by Haruzi (2023), where Figure 4.4 shows the true model with two separate features at similar depths that are not connected to either borehole and the FWI reconstructed model for the conductivity shows a horizontally continuous layer.

We are unable to explain the data with our limitations in 2D, which might be related to the contribution of 3D effects in the data. For example, a 3D waveguiding structure such as an asymmetrical channel with a high contrast in properties could act as a pathway for the tracer, which introduces an even higher contrast in properties. 3D modelling is necessary to confirm any speculations.

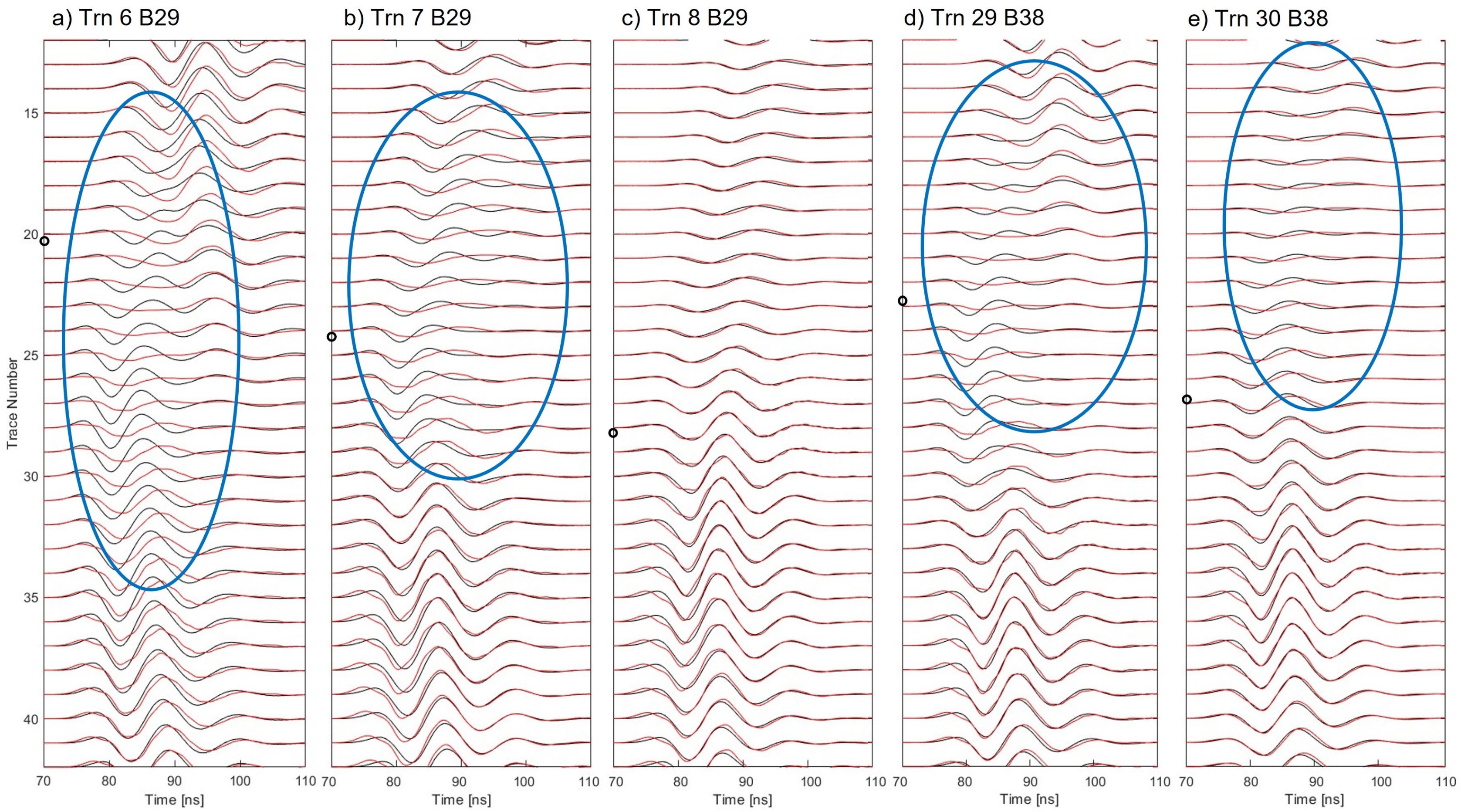

Figure 5-2: Plane 2938 day 5 traces for the measurements of transmitters located in B29 at a) 5.31 m, b) 5.71 m, and c) 6.11 m depth and in B38 at d) 5.593 m and e) 5.993 m depth. Traces are normalized to the global maximum of the background traces. Black traces are the measured data and red traces are the FWI modelled data at the final iteration. Blue ellipses indicate regions of misfit. The black circle on the y-axis indicates the transmitter depth location. Traces 12-42 for B29 and 84-114 for B38 are shown, corresponding to receiver depths of 4.493-7.493 m and 4.51-7.51 m, respectively.

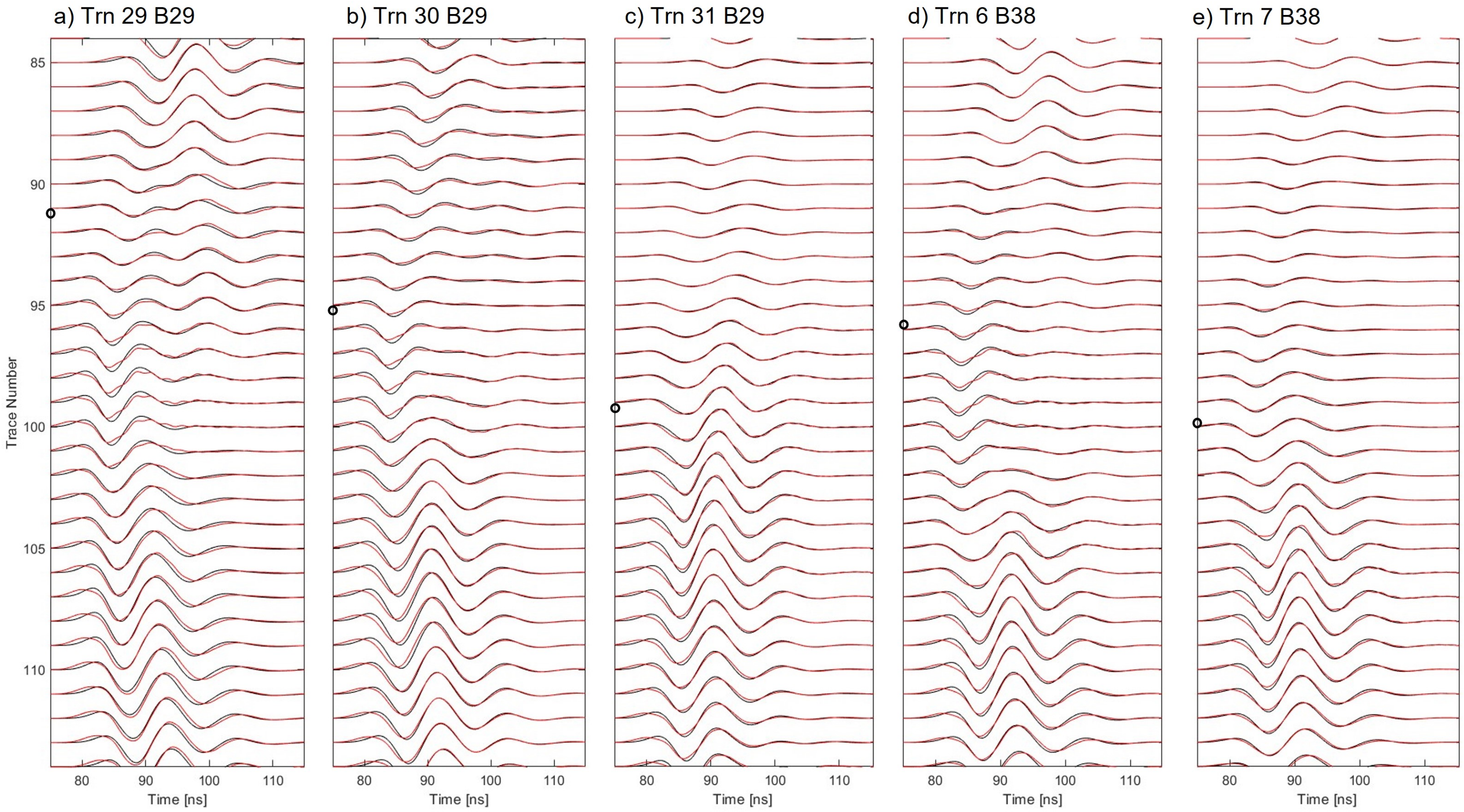

Figure 5-3: Plane 2938 background traces for the measurements of transmitters located in B29 at a) 5.31 m, b) 5.71 m, and c) 6.11 m depth and in B38 at d) 5.593 m and e) 5.993 m depth. Black traces are the measured data and red traces are the FWI modelled data at the final iteration. The black circle on the y-axis indicates the transmitter depth location. Traces 12-42 for B29 and 84-114 for B38 are shown, corresponding to receiver depths of 4.493-7.493 m and 4.51-7.51 m, respectively.

5-2 Repeatability of GPR crosshole measurements

The datasets for days 8 and 9 appeared to be anomalous for all crosshole planes measured. We are unable to explain a physical cause for this, while we exclude processing errors. The arrival times of the data are all delayed, resulting in higher permittivities that are similar to the background and unlike the other time-lapse data. Also anomalous was the background permittivity ZOP of Plane 3831, which had a lower permittivity than all of the time-lapse datasets. Currently, we are unable to identify the source of this behaviour, but possible explanations could be a systematic problem with the equipment or an issue with the WARR measurements for the time-zero corrections, such as the mispositioning of the antennae. Borehole filling effects could also be an explanation for the anomalous data. These effects have been investigated for air- and water-filled boreholes (Mozaffari et al., 2021), but further modelling is needed to understand the behaviour with a hot water borehole filling. Using the day 7 ray-based permittivity starting model for the day 8 and 9 anomalous datasets compensates for this discrepancy, however, further investigation is needed to determine if the anomaly is physical and related to the heat tracer.

Overall, Plane 2938 has the largest contrast in properties for the time-lapse datasets, which are not entirely continuous between boreholes. This poses more challenges for tracer reconstruction due to the heterogeneous heat distribution and therefore caused troubles with fitting as discussed in the previous section. The difference plots for the other three planes (Figure A-6-A-9) located farther from the injection borehole do not show significant changes between subsequent time-lapse datasets. The increase in temperature observed in the temperature logging data in Figure 4-1 is only 0.2°C at 8.9 m depth and 0.6°C at 4.5 m depth for B31, 1°C for B34, which is likely not large enough for the farther planes to show a significant contrast in properties due to the heat. The data was measured for the planes perpendicular to the groundwater flow direction (Plane 3238 and 3831) for many consecutive days starting from day 4, which was not needed. Nevertheless, the almost identical FWI results for the time-lapse datasets demonstrate the repeatability of GPR crosshole measurements and subsequent inversions. A ray-based travel time inversion is completed for each time-lapse dataset and used as the starting model for the FWI; the results are therefore independently obtained. Results in this study are also consistent with the FWI results from Zhou et al. (2021) for Plane 3831. This geophysical method is therefore applicable for time-lapse studies as reliable results can be reproduced without significant artifacts.

Part II

Heat-salt tracer

Chapter 6

Data acquisition and measurement setup

Within the framework of this thesis, a second heat-salt tracer experiment was performed in May 2023 at the Krauthausen test site at the same boreholes as the heat tracer experiment. In addition to the different type of tracer, this time forced-gradient pumping is used. Note that in the previous experiment, the flow followed the natural gradient of the groundwater, while here a defined flow direction with a high flow rate was generated. Careful consideration of the acquisition time is therefore needed to ensure that tracer movement during acquisition, which could potentially cause smearing in the FWI, is not significant.

In this experiment, 20 m^3 of hot salt water with a temperature of 44°C, a calcium concentration of 1800 mg/L, and a chloride concentration of 3200 mg/L was injected in B29 (see Figure 3-1b) at a rate of 2 m^3/h for 10 hours, resulting in an injection total of 20,000 L of the hot salt water mixture. This was attained by dissolving 100 kg of $CaCl_2$, resulting in an electrical conductivity of 1 mS/m. The groundwater has an average temperature of approximately 11°C and Ca^{2+} and Cl^- concentrations of 135 mg/L and 76 mg/L, respectively. The forced-gradient was created between B29, the injection borehole, and B34, the extraction borehole (Figure 3-1b). Pumping at a rate of 2 m^3/h and draining into a nearby stream from B34 took place over the entire injection period and subsequent monitoring days such that the forced gradient was maintained throughout the experiment. High resolution temperature loggers (RBR solo and duet temperature and depth logger, RBR Global) were installed in B31, B32, and B38 at various depths, and a conductivity logger (HOBO salt water conductivity logger, Onset Computer Corporation) in B31 for the entirety of the experiment.

Crosshole GPR data were acquired before (background) and after (time-lapse) the injection of the heat-salt tracer, which started one day after the injection. One crosshole plane configuration, where the majority of the tracer transport is expected to occur, Plane 3831, was measured with 200 MHz PulseEKKO borehole antennae (Sensors & Software Inc.) for four time-lapse days. Three ZOP and three WARR measurements were acquired at the beginning, middle, and end of the experiment for the time zero correction and to monitor tracer movement during acquisition. In addition, ZOP data were acquired for Plane 3238 for the background and each time-lapse dataset. Measurements in B34 were not possible in this experiment due to the permanently installed pump that maintained the forced gradient. As in the heat tracer experiment acquisition, the data were collected in a semi-reciprocal configuration according to Oberröhrmann et al. (2013). Because of the faster transport and to minimize the time that the temperature loggers were removed from the boreholes for GPR acquisition, the acquisition time needed to be minimized. The time-lapse datasets were acquired with double the transmitter spacing (0.4 m) as the background (0.2 m) to optimize the trade-off between the resolution and therefore recovery of the tracer and acquisition time according to Keskinen et al. (2021). This results in 35 total MOGs per time-lapse dataset. Note that the system was warmed up for 15 minutes prior to the measurements to guarantee that amplitudes and pulses are stable.

The time-lapse datasets are noisy due to the generator that was running for the constant pumping and draining into the stream to the East. The generator was located approximately 20 m away from B31. This caused noisier data for the semi-reciprocal configuration with the transmitters located in B31, which was closer to the generator. Additional frequency filtering was necessary for some datasets to remove the high frequency noise present in the data.

Chapter 7

Results

In this chapter, the temperature logging data are given, followed by the zero-offset profile results for each time-lapse dataset, and finally the time-lapse FWI results. We expect a strong increase in conductivity and little to no effect on the permittivity with the presence of the salt and a minor decrease in permittivity and an increase in conductivity with the presence of the heat over the course of the monitoring period as discussed in Chapter 1 (Revil et al., 1998; Archie, 1942; Catenaccio et al., 2003; Seyfried and Grant, 2007).

7-1 Temperature logging data

High resolution temperature logs were measured at 6.5, 7.5, 8.4, and 9.4 m depth in B31 and at 5.5, 6.5, 7.5, 8.5, 9.5, and 10.5 m depth in B38 (Figure 7-1). Directly after the GPR data are measured, the loggers show a deviation from the trend because of the mixing of the fluid in the borehole, which takes approximately 2 hours for the temperature gradient to recover. For B31, the temperature does not start to increase until three days after injection, labelled as day 4. Before it increases, there is an initial decrease of up to 0.1-0.2°C for depths of 6.5, 7.5, and 8.4 m. This is interesting and not related to systematic errors because all sensors show this decrease and it occurs before the GPR measurements. The log at 8.4 m depth has the fastest increase and reaches up to 11.7°C before it decreases again on day 6 to 11.5°C. Also shown for borehole B31 is the electrical conductivity log at 7.97 m, which starts to increase on day 2 and reaches a maximum of 140 mS/m on day 4. It then decreases to approximately 90 mS/m before abruptly increasing again on day 6. This increase in conductivity coincides with the decrease in temperature at 8.4 m depth. For B38, the temperature at all depths starts to increase on day 2. The maximum temperature of 15.2°C is reached at 8.5 m depth on day 4 before it decreases to 11.5°C at the end of the experiment (day 7). The GPR measurements were timed well according to the temperature log results; they were measured at the temperature decrease in B31 on day 4, at the highest temperature in B38 on day 4, and also at the important peaks for the B31 conductivity log.

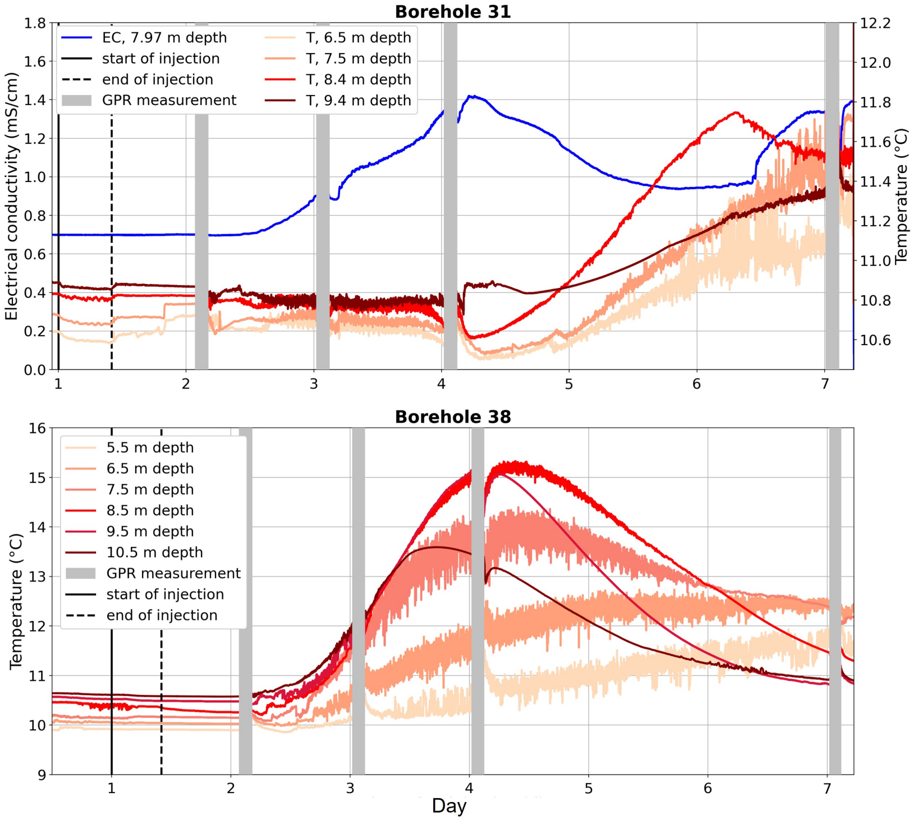

Figure 7-1: Raw temperature breakthrough curves at different depths for boreholes 31 and 38 (B31 and B38). B31 also shows the electrical conductivity at 7.97 m depth (left vertical axis) in addition to the temperature at four depths (right vertical axis). The start and end of the injection are indicated by black vertical lines and the GPR measurements, during which the loggers were removed, are marked by grey vertical lines.

7-2 Zero-offset profiles

Three ZOPs are recorded for each time-lapse dataset over the course of the acquisition to determine if any changes in properties during the acquisition are present, indicating smearing (Figure 7-2). For day 2, there are no changes in the permittivity profiles and a slight decrease in amplitude for the second profile is visible. For day 3, there are differences in the permittivity profiles, with the second ZOP having a higher permittivity than the first, which is the opposite response expected with the presence of the tracer. The amplitude profiles for day 3 show a decreasing behaviour between the first, second, and third ZOPs. This could indicate the presence of more salt over the course of the experiment. Day 4 shows similar relative changes between the three permittivity and amplitude profiles as day 3. For the last day, day 7, a significant decrease in permittivity is apparent for the third profile, which was acquired at 11:15 with the noisier configuration, in comparison to the first two. There do not seem to be significant differences in the amplitude profiles for day 7. The differences in ZOP profiles are potentially caused by heat transport occurring during the acquisition, the mixing of the water in the boreholes between ZOP measurements, or picking errors for the permittivity of the noisy data. The changed properties during the acquisition time can lead to difficulties in the processing and should be taken into consideration during the processing and subsequent interpretation.

To investigate changes over the monitoring period, we use the second ZOP (red profiles in Figure 7-2) of each day, since it provides a representation in the middle of the acquisition time and is always acquired with the configuration with less noise (the transmitter in B38). While crosshole MOGs were only measured for Plane 3831, we measured additional ZOPs for Plane 3238. The permittivity profiles show an increase over the course of the experiment with respect to the background profile, which is the opposite of what is expected in the presence of heat (Catenaccio et al., 2003). This increase occurs at day 3 for Plane 3831 and at day 4 for Plane 3238. For both planes, the presence of salt is evident with the attenuated signal below 5 m depth for all time-lapse days (Figure 7-3). Day 2 already shows some attenuation mainly below 7 m depth. Day 3 shows even more attenuation between 6 and 7 m depth than day 2. Day 4 shows the highest attenuation, where it is completely attenuated below approximately 5 m depth for Plane 3831 and 5.5 m depth for Plane 3238. Day 7 already shows recovery of the amplitudes toward the background, with almost full recovery at Plane 3238. These ZOPs suggest that the presence of salt is observed at the measurement locations before effects from the heat are observed.

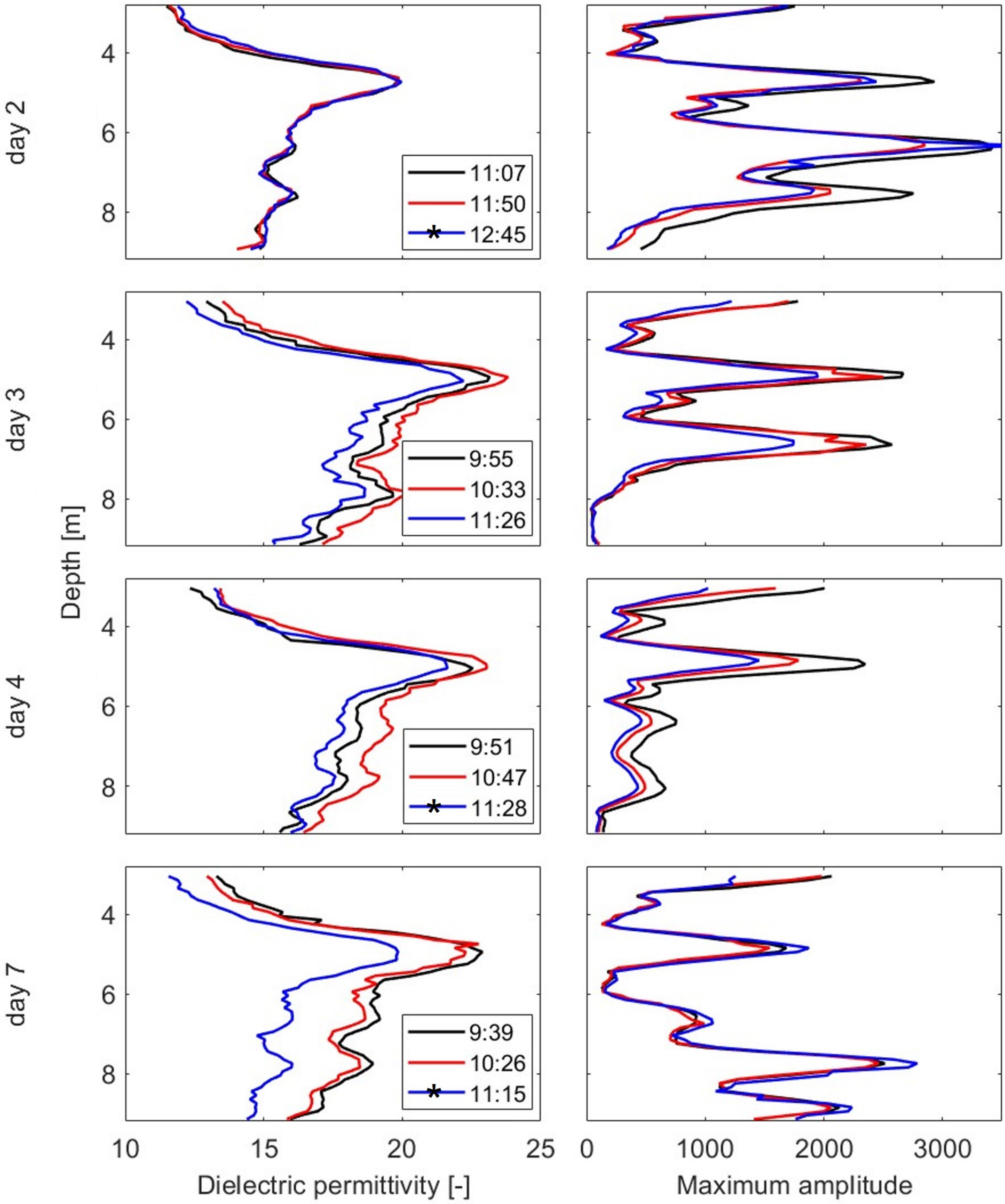

Figure 7-2: Zero-offset profiles (ZOP) for Plane 3831 for all time-lapse days. There are three zero-offset measurements over the course of the experiment for each time-lapse day. The legend entries indicate the time the ZOP was acquired. The legend entries marked with a black star indicate the noisy configuration (transmitter in B31, closer to the generator).

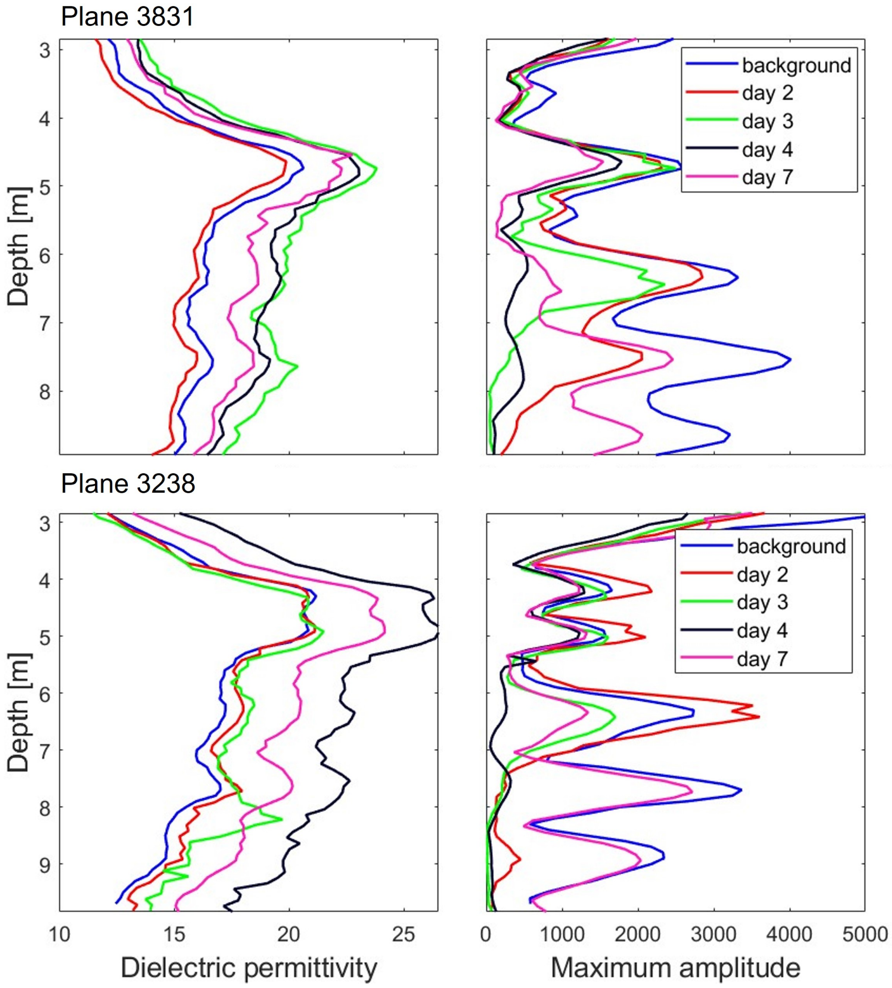

Figure 7-3: Zero-offset profiles for Planes 3831 and 3238 for all time-lapse days. Note that the depth for Plane 3238 extends further than for Plane 3831.

7-3 Time-lapse FWI results

The heat-salt GPR data are relatively noisy because of the generator as mentioned in Chapter 6 and therefore a trapezoidal bandpass filter with corner frequencies of 10-30-200-250 MHz is applied to the data after the dewow for days 3 and 4. Since the noise generated high frequency artifacts in the data, most of this noise could be reduced by this filtering (Figure B-1). Similar to the heat tracer experiment, the starting models used for the FWI are the ray-based permittivity model for the respective dataset and a homogeneous conductivity model of σ=14 mS/m. As the heat-salt GPR data are only measured at Plane 3831, no homogeneous upper layer of ε_r=14 needs to be added to the starting model because this upper layer is well recovered in the FWI for this plane (Figure 7-4). The same FWI processing workflow is then followed similar to the heat tracer experiment, with the source wavelet correction applied once for each time-lapse dataset using the background source wavelet as the input. The traces for the time-lapse datasets are normalized to the global maximum of the background dataset as in Subsection 4-4-2 to ensure comparability of the effective source wavelets. The inversion settings are optimized and determined to be the same as for the heat tracer experiment: a permittivity perturbation factor of 10^{-4}, a conductivity perturbation factor of 10, and conductivity and permittivity stabilization factors of 50. Note that all FWI results have no remaining gradients and the FWI convergence criteria are satisfied except for the RMS reduction from the starting model of at least 50% for the time-lapse datasets.

The final FWI permittivities for days 2 and 3 do not show significant differences relative to the background besides minor differences at around 6 m depth (Figure 7-4). Day 4 shows an overall increase and day 7 an overall decrease, particularly at 5.6-7.5 m depth. The results for day 4 are particularly noisy and the permittivity values in the ray-based inversion and the FWI model are higher than the background (Figure 7-4). Using the ray-based permittivity starting model from day 3 for day 4 is therefore tested, similar to days 8 and 9 in the heat dataset (Figure B-3). The cause of this is further discussed in Chapter 8 and the original result for day 4 is kept. The final FWI conductivity results increase to above 30 mS/m below 8 m depth until day 4 (Figure 7-4), likely caused by the salt. Day 2 shows an increase in conductivity in the upper layer above 3.6 m depth. An increase in conductivity is also observed between 5.5-7.5 m depth for days 4 and 7, likely caused by the heat. The FWI conductivity results for day 7 no longer show the increased conductivity below 8 m from the salt. The source wavelets in Figure 7-5 have the same shape for all datasets and have a decreasing amplitude from day 2 to 4 and an increase in amplitude for day 7, which is the same behaviour as observed in the ZOP data. Note that because of the higher noise level, the FWI convergence criteria are not completely met (Figure 7-5 and Table 7-1). The time-lapse FWI results do not have a reduction in RMS from the starting model of at least 50%, but a reduction of 45.1%, 44.3%, 30.0%, and 40.2% for days 2, 3, 4, and 7, respectively. The FWI performance results in Table 7-1 show that day 4 has the lowest R^2, while all other datasets have an R^2 of at least 0.8.

To analyze the changes in permittivity and conductivity over the course of the experiment, the background permittivity and conductivity FWI results are subtracted from each time-lapse FWI result (Figure 7-6). Similar to the heat tracer experiment difference plots, red indicates an increase and blue a decrease in permittivity and conductivity with respect to the background. There is a high permittivity anomaly for day 2 at the top of the plane extending to approximately 3.7 m depth in the left, close to B38, which is not observed for

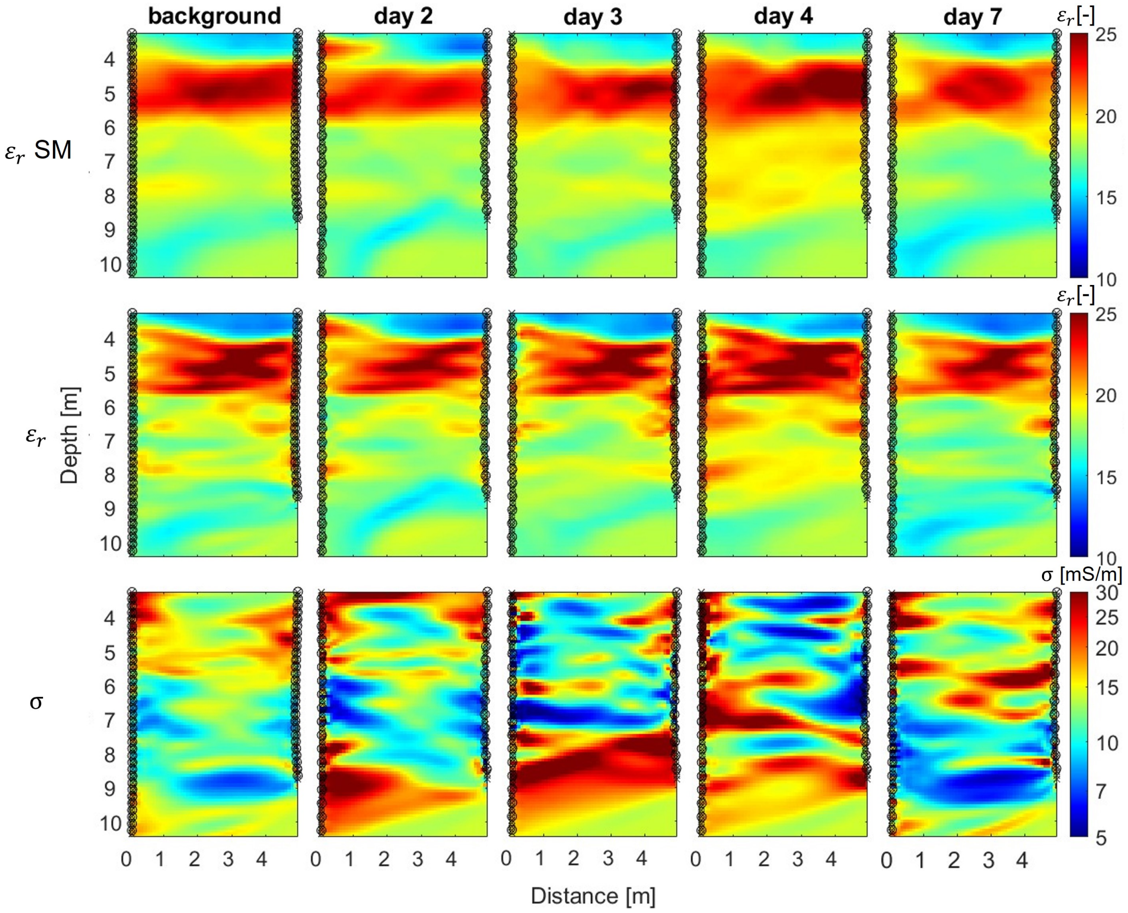

Figure 7-4: Time-lapse FWI results for all datasets of the heat-salt tracer experiment (Plane 3831). The top row shows the permittivity starting model, the middle the final FWI permittivity, and the bottom row the FWI conductivity result for each time-lapse dataset (columns). Note the logarithmic scale for the conductivity. The transmitter and receiver locations are indicated with circles and crosses, respectively.

subsequent days. For day 3, there is an increase of $\Delta\varepsilon$=1 below 8 m depth. Day 4 has an increase of around $\Delta\varepsilon$=3 over the entire plane and up to $\Delta\varepsilon$=4 close to B38. Also shown in Figure 7-6 is the FWI difference plot for the day 4 result using the day 3 starting model (day 4 update). The permittivity shows FWI results more consistent with the time-lapse trend, but it is unclear if the increase in permittivity for the original day 4 FWI is physical. Day 7 shows a decrease in permittivity of up to $\Delta\varepsilon$=2 over the entire plane. An increase in conductivity below 8 m is already evident on day 2 and is also present for days 3 and 4, which is likely caused by the salt. Day 2 also has a high conductivity anomaly at the top of the plane extending to approximately 3.6 m, which appears to be an isolated event during day 2. It is possible that the tracer is travelling in the upper high hydraulic conductivity layer on day 2. Day 4 has a higher conductivity anomaly at depths of 5.8-7.4 m which is also present on day 7 closer to B31, likely caused by the heat.

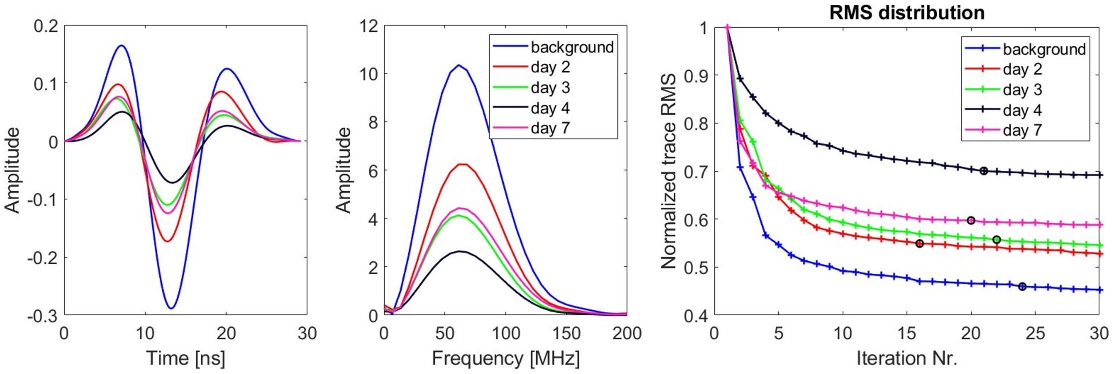

Figure 7-5: Source wavelets (left), corresponding amplitude spectra (middle), and normalized RMS distribution (right) for each of the background and time-lapse datasets for Plane 3831. The black circles in the RMS distributions indicate the final iterations chosen for each result based on the stopping criteria.

Table 7-1: Comparison of FWI results for the background and time-lapse datasets for the heat-salt tracer experiment. The remaining gradients are the mean of the absolute value of the smoothed permittivity and conductivity gradients of the final iteration model. The root-mean-squared error (RMS), the RMS normalized to the starting model, as well as the correlation coefficient between the observed and FWI modelled data are given for the final iteration.

Dataset	Final iteration	Grad. ε mean $*10^4$	Grad. σ mean $*10^{-5}$	Final RMS $*10^{-6}$	Final RMS norm. (%)	R^2
BG	24	6.46	13.76	1.260	45.9	0.928
day 2	16	4.27	4.77	1.070	54.8	0.871
day 3	22	2.86	1.66	0.829	55.4	0.844
day 4	21	1.13	1.88	0.711	70.0	0.775
day 7	20	2.03	4.60	1.012	59.4	0.807

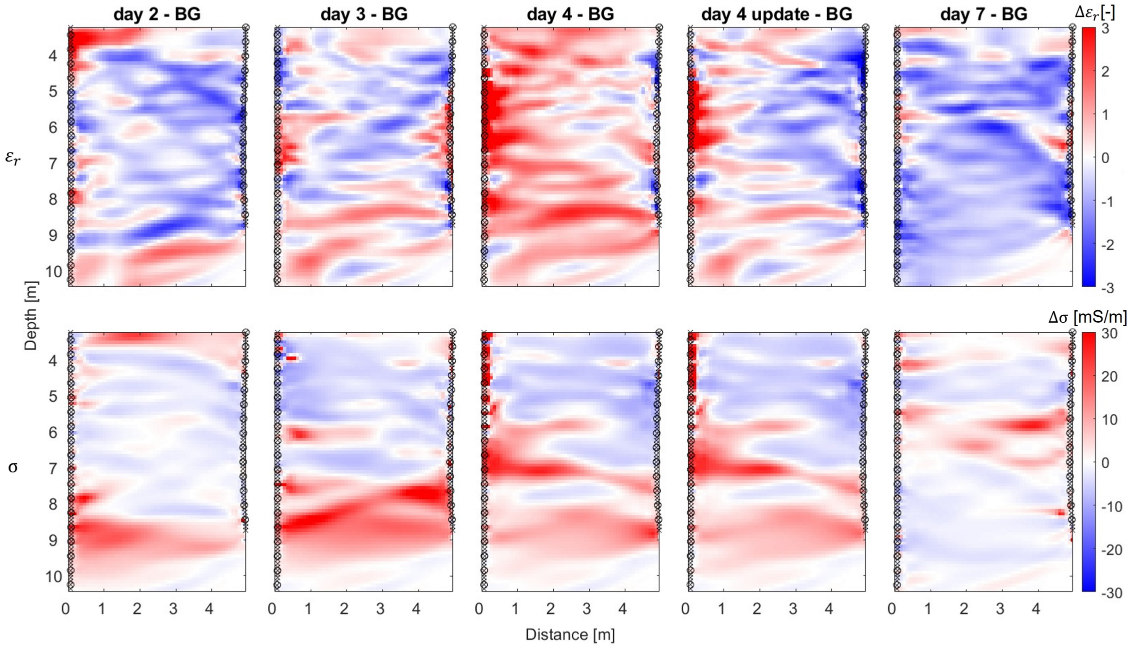

Figure 7-6: Time-lapse FWI difference results for the heat-salt tracer experiment, Plane 3831. The background FWI model is subtracted from each time-lapse FWI model. The top row shows the FWI permittivity difference and the bottom row the FWI conductivity difference for each time-lapse dataset and for day 4 using an updated starting model (columns).

7-4 Comparison of results

The difference plots in Figure 7-6 and the ZOP results in Figure 7-3 show signs of the heat-salt tracer, despite the low signal-to-noise ratio of the GPR data. The data in these figures suggest the presence of salt at depths deeper than 7.5 m at day 2 in both the 3831 and 3238 maximum amplitude ZOP data and below 8 m in the FWI conductivity model, with values up to 20 mS/m higher than the background. The effect of the salt in the data is stronger for day 3, with the maximum amplitude ZOP being almost completely attenuated from 7 m to depth and the FWI conductivity having an even stronger positive anomaly with respect to the background of up to 40 mS/m. The ZOP maximum amplitude profiles for day 4 show almost complete attenuation below 5.5 m. The FWI conductivity results for day 4 also show higher conductivities below 5.8 m, with two separate anomalies potentially reflecting the presence of heat closer to B38 from 5.8-7.4 m depth with a positive anomaly of up to 20 mS/m and salt below 8 m depth with a positive anomaly of up to 10 mS/m. For day 7, the maximum amplitude ZOP shows recovery towards the background except between 5.5-7 m depth where more attenuation is observed. This is similar to the FWI conductivity result for day 7, where there is a positive difference from approximately 5.8-7.4 m depth across the entire plane of up to $\Delta\sigma$=25 mS/m. This is interpreted as the effects from the heat, while the effects from the salt (increases in conductivity at depth in the aquifer) are no longer observed after day 4. This is consistent with the electrical conductivity log that shows a peak in conductivity at day 4, after which it decreases until day 6 (Figure 7-1). The temperature increase is first observed at B38 after the GPR measurements on day 2, while it is not observed in B31 until day 4 according to the temperature logging data (Figure 7-1). This is reflected in the FWI conductivity results as there is a positive difference close to B38 on day 3, which seems to enlarge and travel closer to B31 on day 4 and day 7.

Chapter 8

Discussion

The three ZOP measurements per time-lapse day in Figure 7-2 show some changes in permittivity and conductivity during the acquisition time. However, error from the time zero correction could be the cause of the varying permittivity profiles. More attention to which WARR measurement is used for the correction is needed to ensure the least error in the time zero correction. Noise levels in the time-lapse data are also significant and cause more uncertainty in first-break picking for the permittivity profiles. The maximum amplitude profiles on each day also show some discrepancies. To ensure that tracer movement during acquisition is not significant, two effective source wavelets for day 4 were computed using only measurements from B31 and then from B38. The wavelets did not show significant differences (Figure B-2) and therefore it is assumed that tracer movement during acquisition was not significant. Note that we capture the salt effects in the crosshole plane, however, we also expect out-of-plane effects due to the 3D nature of the salt plume.

It is unclear whether the high permittivity FWI result for day 4 is due to physical causes or a result of systematic errors in the data for this day. Since the logging data also shows an initial decrease in temperature before the acquisition of this dataset, it is possible that the permittivity increase is caused by a decrease in temperature. Directly before the injection of the tracer, water with a lower temperature than the groundwater was injected from an external source, the nearby stream, to generate the forced-gradient flow field. The amount of this initial water injection could be significant enough to cause a cold front before the heat arrives at the measurement locations. The forced-gradient flow field is also different than the natural groundwater flow as pumping creates flow towards the extraction borehole from all directions. This could potentially cause more complex and heterogeneous heat transport. The increase in permittivity is observed over the entire plane and is unlike other time-lapse datasets, while the conductivity result fits the trend to other time-lapse datasets, showing results consistent with an increase in temperature from 6-8 m depth. A decrease in temperature therefore does not completely explain this anomaly. There is also significant noise in the data for day 4, which is not completely removed by applying the bandpass filter. This causes more errors in the time zero correction and in the travel time inversion due to the ambiguous first-break picking. In turn, this could cause the observed high permittivities in the ray-based starting model due to a time shift. Similar to days 8 and 9 in the heat tracer dataset, this can be compensated for by using the ray-based permittivity starting model from the previous day, such that the corrected source wavelet is then shifted to compensate for the time shift in the data. The FWI results for day 4 using the starting model from day 3 (Figure B-3, day 4 update) show a permittivity result consistent with the time-lapse trend and a nearly unchanged conductivity result when compared to the original day 4 result (Figure 7-4). Another contributing factor to this anomalous dataset could be borehole filling effects as discussed in section 5-2. Note that this effect is observed in both the heat and heat-salt tracer data and more studies on the effects of borehole filling are needed to confirm that it is related.

Part III

Chapter 9

Conclusions and outlook

We have applied time-lapse crosshole GPR FWI to monitor both a heat and a heat-salt tracer at the Krauthausen test site. We showed the ability of GPR FWI to monitor variations in both permittivity and conductivity in the presence of a heat tracer and to separately detect the effects of salt and heat, which exhibit different transport mechanisms, for a combined heat-salt tracer.

9-1 Comparison of three field tracer tests

GPR FWI has now been applied to three tracer tests conducted at the Krauthausen test site: a salt tracer (Haruzi, 2023), a heat tracer, and a heat-salt tracer. The FWI and logging results of the salt tracer indicate solute transport at depth in the aquifer, deeper than 8 m, as a result of the tracer having a higher density than the groundwater. In the heat tracer results, a high conductivity anomaly appeared at 5.5-6 m depth in the injection plane (2938) and is suspected to be an artifact of the FWI failing to fit the complex waveguiding structure for transmitters and receivers in this depth range. This anomaly was not observed in the salt tracer study. Since the FWI had a reasonable data fit for the background dataset in this region, this anomaly is expected to be caused by the introduction of heat in a complex waveguiding structure. The heat tracer time-lapse FWI results show minor negative contrasts in permittivity of up to $\Delta\varepsilon_r$=5 with respect to the background and positive conductivity contrasts of up to $\Delta\sigma$=10-15 mS/m. The permittivity showed an overall decrease over the entire plane for all planes other than the injection plane, while the conductivity showed both increases and decreases in different regions. The conductivity indicates the presence of the heat primarily at depths of 6-8.5 m. This demonstrates that the heat tracer is transported in different regions and has different density effects than the salt tracer. For all planes other than 2938, which includes the injection borehole, only minor differences between subsequent time-lapse days are observed. Consequently, there might not be a strong enough contrast in conductivity or permittivity to recover heat tracers for natural gradient field tracer tests on larger scales. Nevertheless, the FWI results in regions where little to no changes from the tracer were detected demonstrate the repeatability of the GPR measurements and inversion.

The heat-salt tracer used a forced-gradient, in which pumping from an extraction borehole took place. This accelerated the tracer flow and therefore the time scales for solute and heat transport are not comparable to the salt and heat tracers, which were natural gradient experiments. Additionally, the forced-gradient flow field is different than the natural groundwater flow as pumping creates flow towards the extraction borehole from all directions. We were able to detect the effects of both the salt and the heat with the permittivity and conductivity FWI results. Similar to the salt tracer test, the salt was primarily transported at depths deeper than 8 m. The effects of the heat were detected two days after the salt and it was primarily detected at depths of 5.5-7.5 m. This is partly consistent with the heat tracer, where the heat was detected with conductivity for the same plane, which is perpendicular to flow, at depths of 6-8.5 m as well as in the upper layer until 3.7 m depth. The positive contrast in conductivity at 6-8.5 m depth was not laterally continuous across the plane for the heat tracer, while the contrast for the heat-salt tracer in this region was a continuous layer connecting both boreholes at the end of the experiment on day 7. Considering all three tracer experiments, salt and heat tracers are complementary because they provide information on different parts of the aquifer due to their different transport mechanisms and their opposite density effects.

In contrast to the maximum amplitude ZOPs, the permittivity ZOPs did not always show consistent trends with the FWI results between time-lapse datasets for both the heat and the heat-salt tracer tests. The cause of this is unclear, but it could be explained by the ZOPs only indicating averaged properties over the span of the plane or by acquisition errors. They should therefore not be over-interpreted and should not be stand-alone results. For the salt tracer, only the maximum amplitude profiles show changes from the salt and therefore problems were not encountered with the ZOP analysis.

9-2 Outlook

In this thesis, only geophysical parameters, namely, ε_r and σ, were obtained and analyzed. Additionally, we expected a decrease in permittivity in the presence of the heat tracer by only considering the relationship between temperature and the permittivity of water. However, heat transport also occurs through conduction in the matrix and the relationship between temperature and permittivity is different for various sediments, soils, water contents, and measurement frequencies (Seyfried and Grant, 2007). This should be considered in further analyses. The analysis of the FWI results of the tracer tests will be taken a step further by using empirical petrophysical relations to transform the results into temperature (Seyfried and Grant, 2007), allowing for a more in-depth comparison of the logging data and the FWI results.

To our knowledge, this is the first study that has monitored a heat tracer, which provides changes in conductivity in addition to permittivity, with crosshole GPR. We were able to detect changes in permittivity, however, testing a tracer that provides a higher contrast in permittivity could further improve monitoring capabilities. For example, ethanol has a relative permittivity of 25 (Shakas et al., 2017) and would therefore provide a stronger contrast in permittivity with respect to the groundwater (ε_r=80 for water at 20°C) than the heat tracer. A synthetic study conducted by Haruzi et al. (2022) has shown the feasibility of such a tracer. An ethanol tracer is therefore of interest for future experiments.

There are many sources of error contributing to the final FWI results. Axtell et al. (2016) have already evaluated and quantified errors for determining velocities with ray-based techniques, including, antennae positioning error, first-break picking, and the time-zero correction. Although first-break picking is not needed anymore in FWI, it still remains important to minimize any measurement error during acquisition and to apply accurate time zero corrections. Besides the measurement and picking errors, uncertainty quantification for GPR FWI requires further investigation.

Borehole filling effects have been investigated for air- and water-filled boreholes, where the velocity contrast at the subsurface-borehole interface can produce refractions along the interface and higher apparent velocities than the true velocities are present for higher ray angles (Mozaffari et al., 2021). Further investigation and modelling of these effects are needed to understand the behaviour, which could be different for hot or salt water borehole filling. Current developments in 2.5D and 3D FWI will allow for more accurate modelling in the future (Mozaffari et al., 2020; Mozaffari, 2022). This would permit 3D modelling of a circular waveguide structure to investigate whether borehole effects could explain the observed phenomena. This 3D code would also allow for more accurate modelling of the anomaly in Plane 2938 of the heat dataset, interpreted as an artifact of our current limitations in 2D.

Appendix A

Heat tracer additional results

Table A-1: Comparison of FWI results for all datasets of Plane 2938. The remaining gradients are the mean of the absolute value of the smoothed permittivity and conductivity gradients of the final iteration model. The trace root-mean-squared error (RMS), the RMS normalized to the starting model, as well as the correlation coefficient between the observed and FWI modelled data are given for the final iteration. Note that stabilization factors of 50 and a permittivity perturbation factor, $\delta\varepsilon$, of 10^{-4} are used for all datasets.

Dataset	$\delta\sigma$	Final iteration	Grad. ε mean $*10^4$	Grad. σ mean $*10^{-5}$	Final RMS $*10^{-6}$	Final RMS norm. (%)	R^2
BG	10^1	16	5.07	9.92	1.069	34.1	0.939
day 2	10^1	16	2.93	2.52	0.541	43.0	0.909
day 3	10^1	23	3.23	1.99	0.546	46.5	0.887
day 4	10^0	22	5.49	3.27	0.586	46.0	0.891
day 5	10^1	22	1.57	1.62	0.511	40.7	0.903
day 6	10^1	13	3.10	2.63	0.617	46.3	0.883
day 7	10^1	15	3.49	3.00	0.632	43.7	0.886
day 8	10^1	19	1.70	3.13	0.650	40.7	0.900
day 10	10^0	18	5.15	3.97	0.849	43.9	0.883
day 14	10^1	17	4.55	5.45	0.847	38.2	0.915
day 17	10^1	28	3.15	5.81	0.852	35.1	0.930

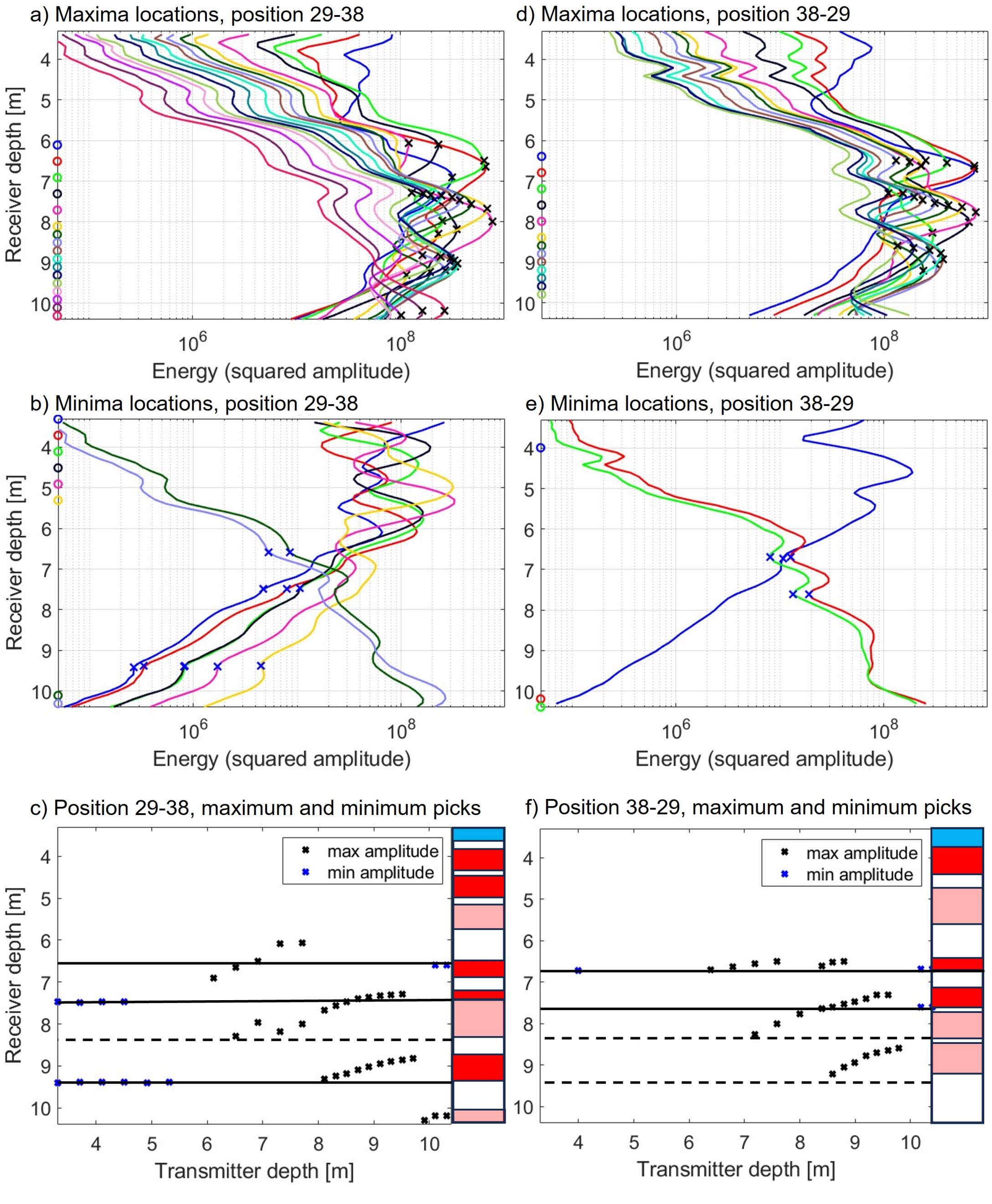

Figure A-1: Amplitude analysis for the background dataset of Plane 2938 in the lower aquifer. Trace energy profiles for different transmitter depths (colours) in borehole B29 that show clear (a) trace energy maxima and (b) minima. Note that the transmitter depth is plotted as a circle with the corresponding colour. c) Transmitter vs receiver depth plot for the maximum and minimum picks with an interpreted waveguide column including findings from Figure 4-3, where blue indicates the upper low permittivity layer, solid red indicates low velocity waveguides constrained with both maximum and minimum picks, and transparent red indicates less constrained low velocity waveguides. d)-f) show the maxima and minima picks for the opposite configuration, with the transmitters in borehole B38.

Table A-2: Comparison of FWI results for all datasets of Plane 3834. The remaining gradients are the mean of the absolute value of the smoothed permittivity and conductivity gradients of the final iteration model. The trace root-mean-squared error (RMS), the RMS normalized to the starting model, as well as the correlation coefficient between the observed and FWI modelled data are given for the final iteration. Note that stabilization factors of 50, a permittivity perturbation factor, $\delta\varepsilon$, of 10^{-4}, and a conductivity perturbation factor, $\delta\sigma$, of 10 are used for all datasets.

Dataset	Final iteration	Grad. ε mean $*10^4$	Grad. σ mean $*10^{-5}$	Final RMS $*10^{-6}$	Final RMS norm. (%)	R^2
BG	20	6.95	8.84	0.921	32.8	0.949
day 14	22	2.62	3.63	0.777	37.2	0.934
day 17	25	2.76	2.78	0.764	36.4	0.932

Table A-3: Comparison of FWI results for all datasets of Plane 3238. The remaining gradients are the mean of the absolute value of the smoothed permittivity and conductivity gradients of the final iteration model. The trace root-mean-squared error (RMS), the RMS normalized to the starting model, as well as the correlation coefficient between the observed and FWI modelled data are given for the final iteration. Note that stabilization factors of 50, a permittivity perturbation factor, $\delta\varepsilon$, of 10^{-4}, and a conductivity perturbation factor, $\delta\sigma$, of 10 are used for all datasets.

Dataset	Final iteration	Grad. ε mean $*10^4$	Grad. σ mean $*10^{-5}$	Final RMS $*10^{-6}$	Final RMS norm. (%)	R^2
BG	26	3.89	7.87	0.787	32.7	0.964
day 4	29	5.24	8.02	1.099	38.9	0.936
day 5	29	6.21	9.79	1.129	41.9	0.925
day 6	24	3.94	1.07	0.996	40.8	0.932
day 7	24	3.39	4.16	0.874	43.2	0.927
day 8	28	7.56	10.31	1.002	45.8	0.924
day 9	28	4.53	5.67	0.910	43.6	0.931
day 10	22	2.85	4.63	0.936	43.7	0.921
day 14	28	3.60	6.79	0.980	44.3	0.911

Table A-4: Comparison of FWI results for all datasets of Plane 3831. The remaining gradients are the mean of the absolute value of the smoothed permittivity and conductivity gradients of the final iteration model. The trace root-mean-squared error (RMS), the RMS normalized to the starting model, as well as the correlation coefficient between the observed and FWI modelled data are given for the final iteration. Note that stabilization factors of 50, a permittivity perturbation factor, $\delta\varepsilon$, of 10^{-4}, and a conductivity perturbation factor, $\delta\sigma$, of 10 are used for all datasets.

Dataset	Final iteration	Grad. ε mean $*10^4$	Grad. σ mean $*10^{-5}$	Final RMS $*10^{-6}$	Final RMS norm. (%)	R^2
BG	17	9.34	7.96	1.089	34.4	0.952
day 4	25	6.71	10.52	1.066	32.9	0.957
day 5	29	5.39	10.74	0.973	30.0	0.962
day 6	24	7.39	9.01	1.298	41.5	0.932
day 7	21	4.23	5.47	0.940	35.5	0.949
day 8	14	8.16	8.77	1.009	37.5	0.944
day 9	15	6.18	6.74	1.030	37.3	0.944
day 10	24	5.30	7.01	1.193	42.3	0.926
day 11	23	4.17	5.38	0.841	34.6	0.951
day 13	26	5.97	6.86	1.085	36.6	0.941
day 14	25	5.63	8.72	1.057	37.9	0.940
day 17	26	4.33	7.33	0.963	34.1	0.950
day 20	25	6.40	5.07	1.024	35.9	0.943
day 24	21	4.43	5.80	1.050	35.3	0.945
day 28	22	4.44	6.45	1.015	34.9	0.947
day 37	22	4.94	6.32	1.198	37.8	0.938

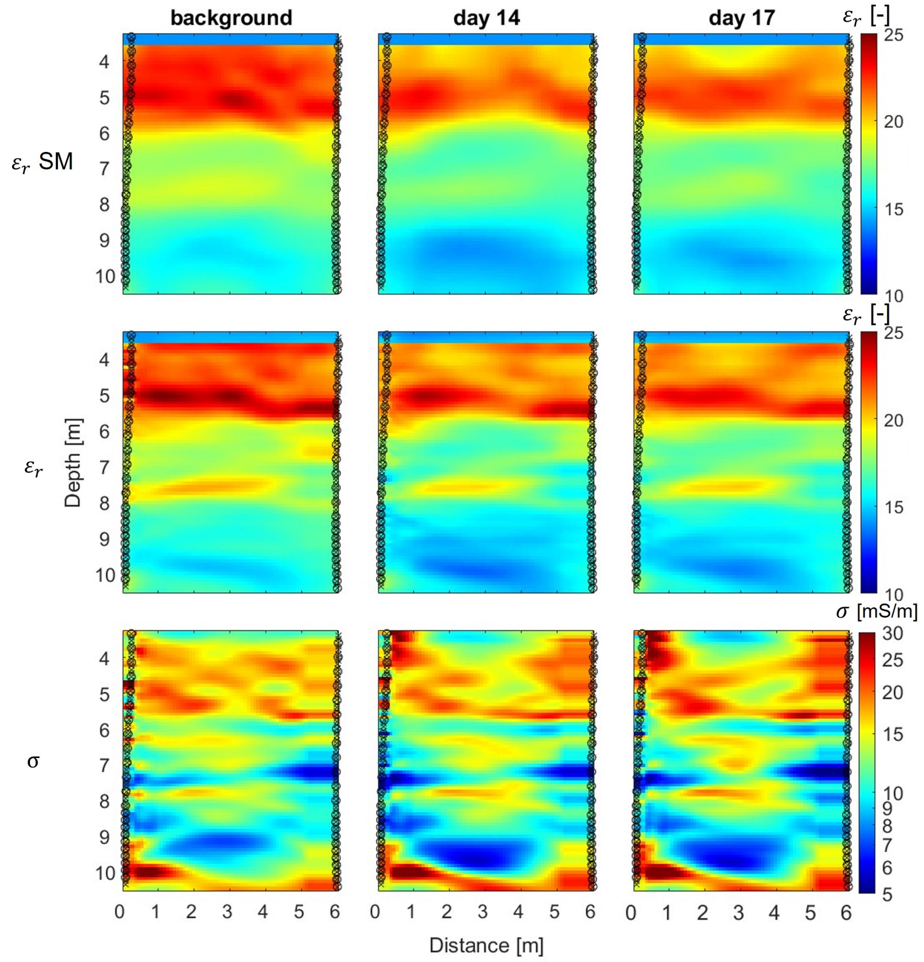

Figure A-2: FWI results for all datasets of Plane 3834. The top row shows the starting model for the background and each time-lapse dataset, the middle row the final FWI permittivity, and the bottom the final FWI conductivity result. Note the logarithmic scale for the conductivity. The transmitter and receiver locations are indicated with circles and crosses, respectively.

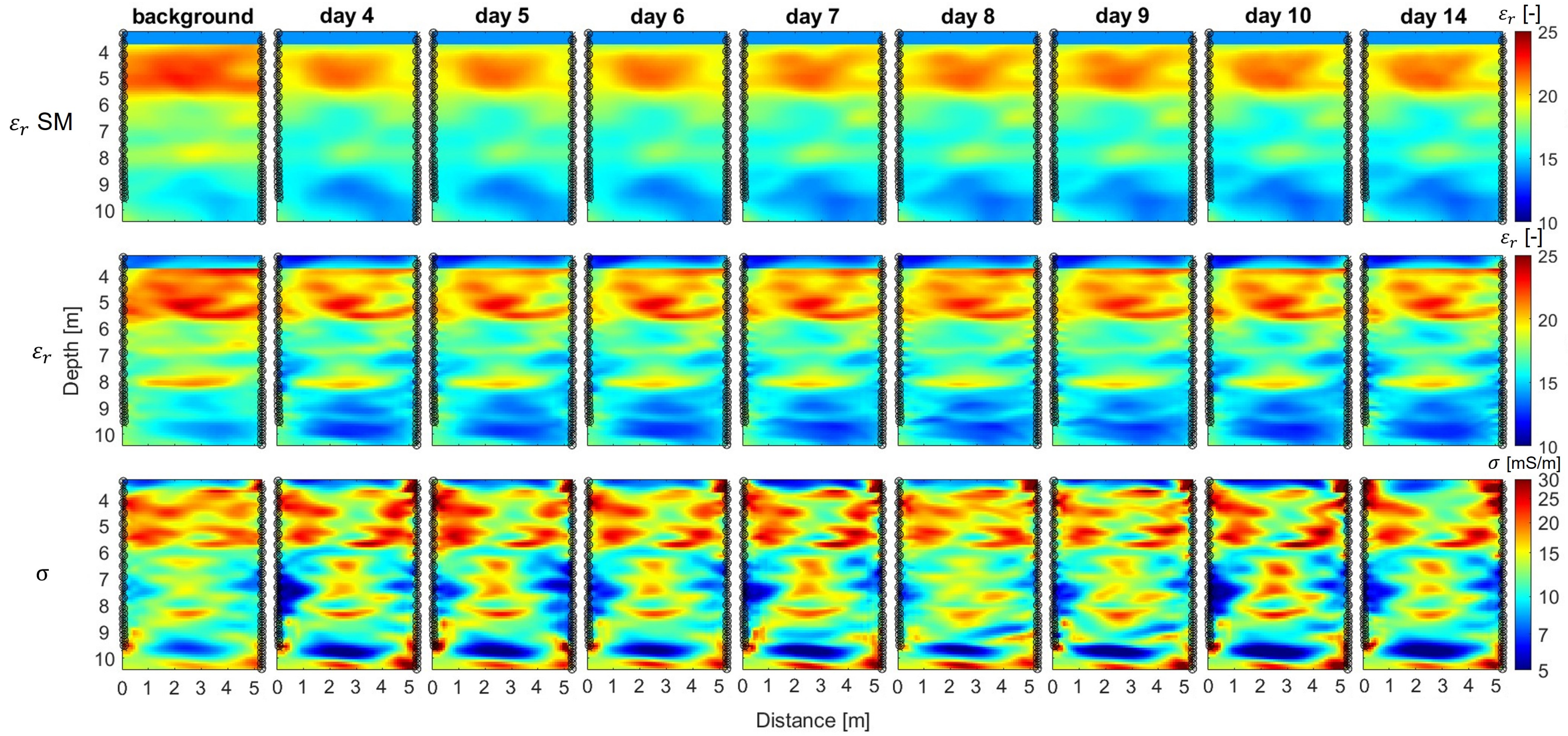

Figure A-3: FWI results for all datasets of Plane 3238. The top row shows the starting model for the background and each time-lapse dataset, the middle row the final FWI permittivity, and the bottom the final FWI conductivity result. Note the logarithmic scale for the conductivity. The transmitter and receiver locations are indicated with circles and crosses, respectively.

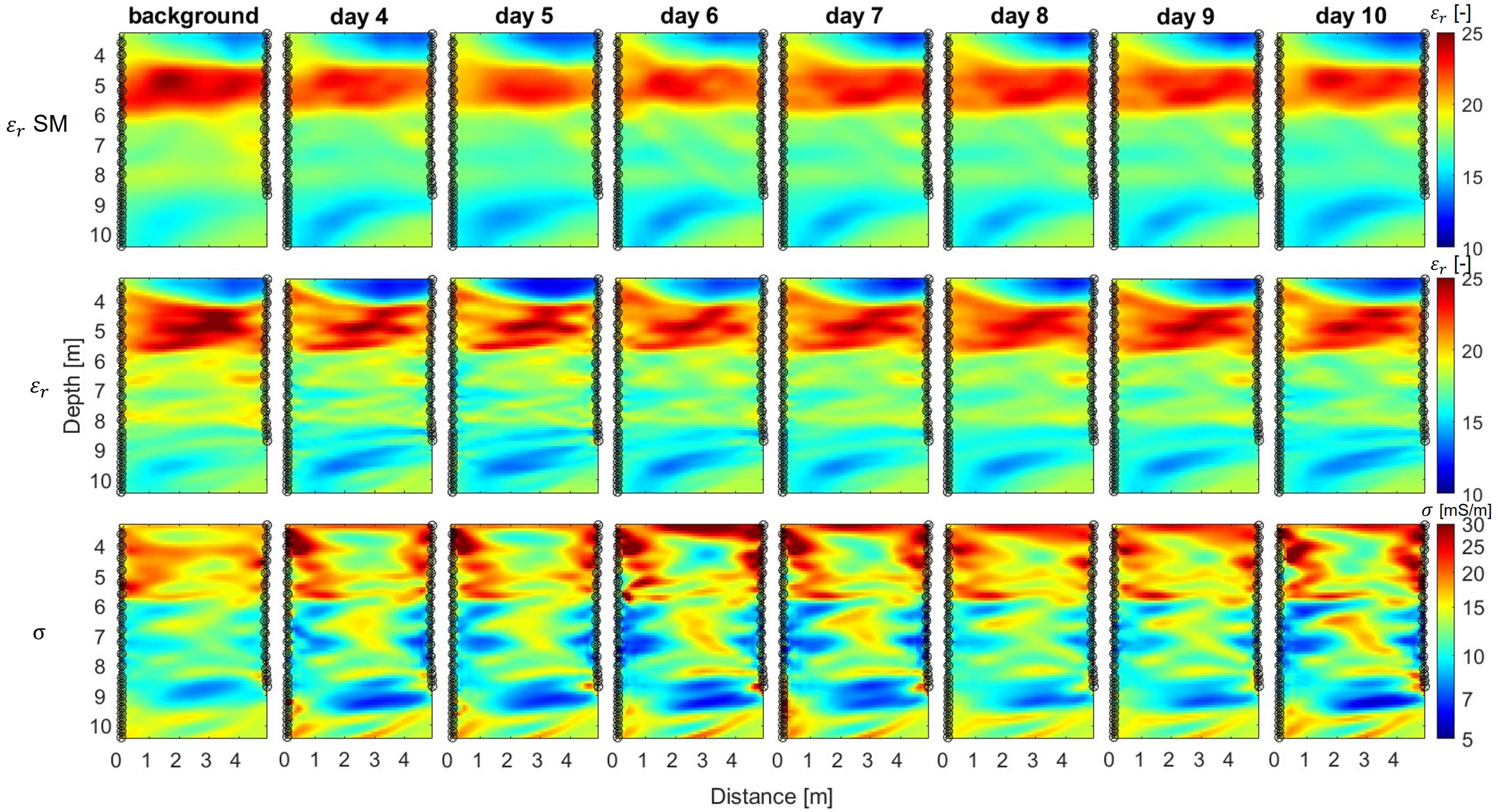

Figure A-4: FWI results for the datasets of Plane 3831 until day 10. The top row shows the starting model for the background and each time-lapse dataset, the middle row the final FWI permittivity, and the bottom the final FWI conductivity result. Note the logarithmic scale for the conductivity. The transmitter and receiver locations are indicated with circles and crosses, respectively.

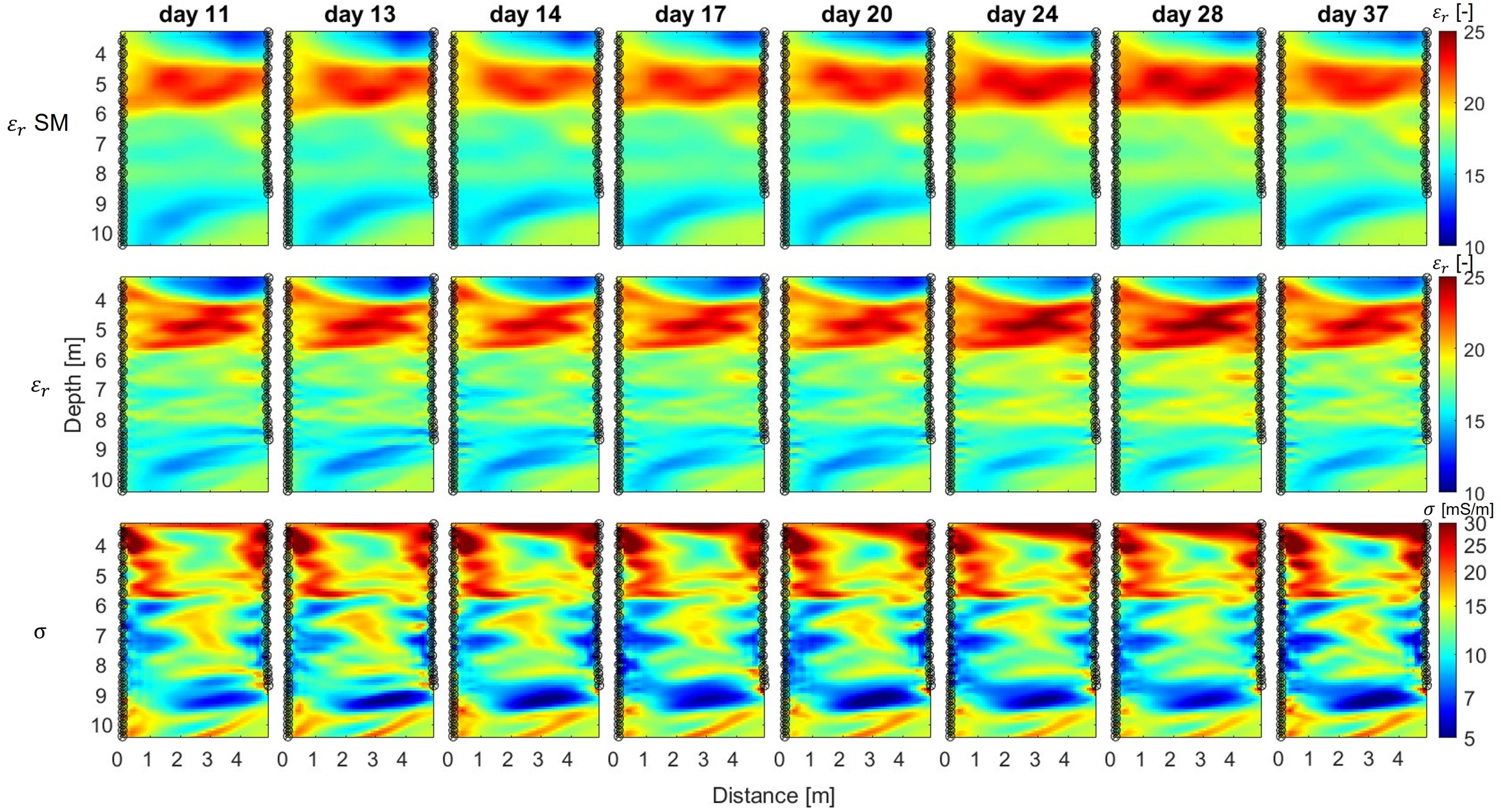

Figure A-5: FWI results for day 11-37 datasets of Plane 3831. The top row shows the starting model for the background and each time-lapse dataset, the middle row the final FWI permittivity, and the bottom the final FWI conductivity result. Note the logarithmic scale for the conductivity. The transmitter and receiver locations are indicated with circles and crosses, respectively.

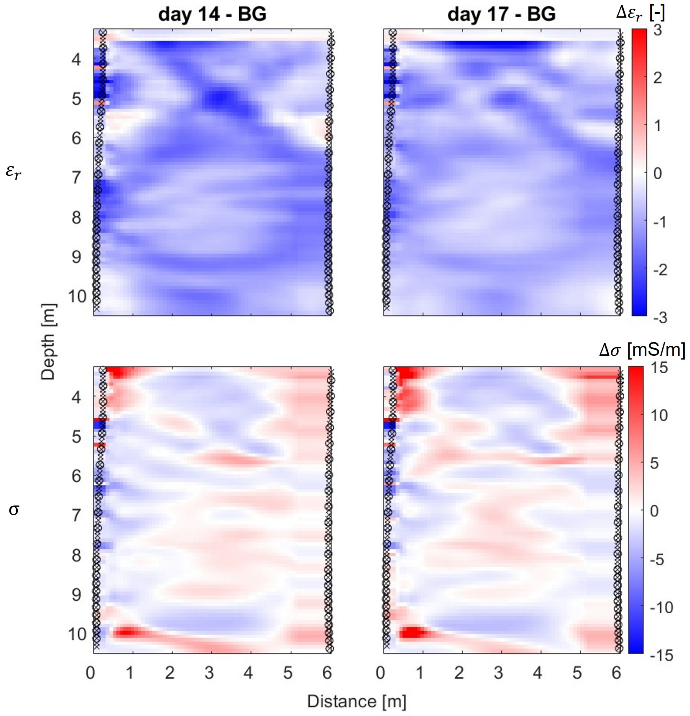

Figure A-6: Time-lapse FWI results with respect to the background for Plane 3834.The top row shows the FWI permittivity and the bottom row the FWI conductivity with the background FWI subtracted for each time-lapse dataset (columns).

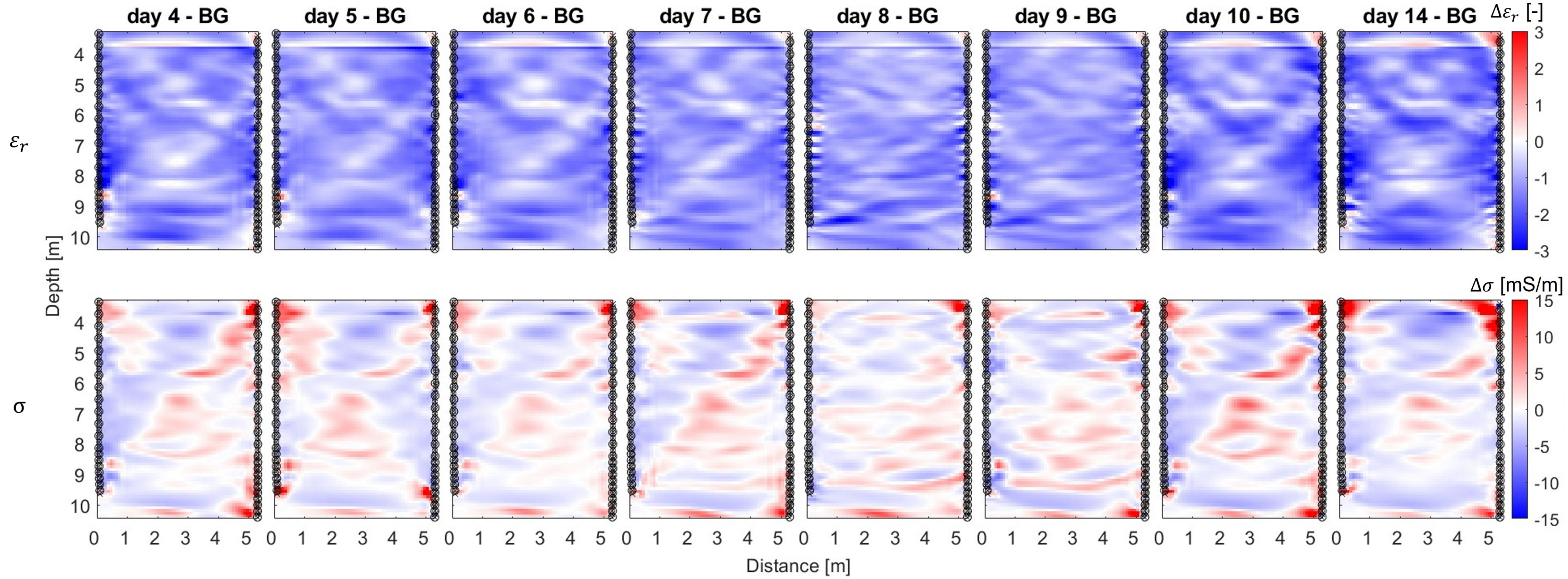

Figure A-7: Time-lapse difference FWI results with respect to the background for Plane 3238. The top row shows the FWI permittivity and the bottom row the FWI conductivity with the background FWI subtracted for each time-lapse dataset (columns).

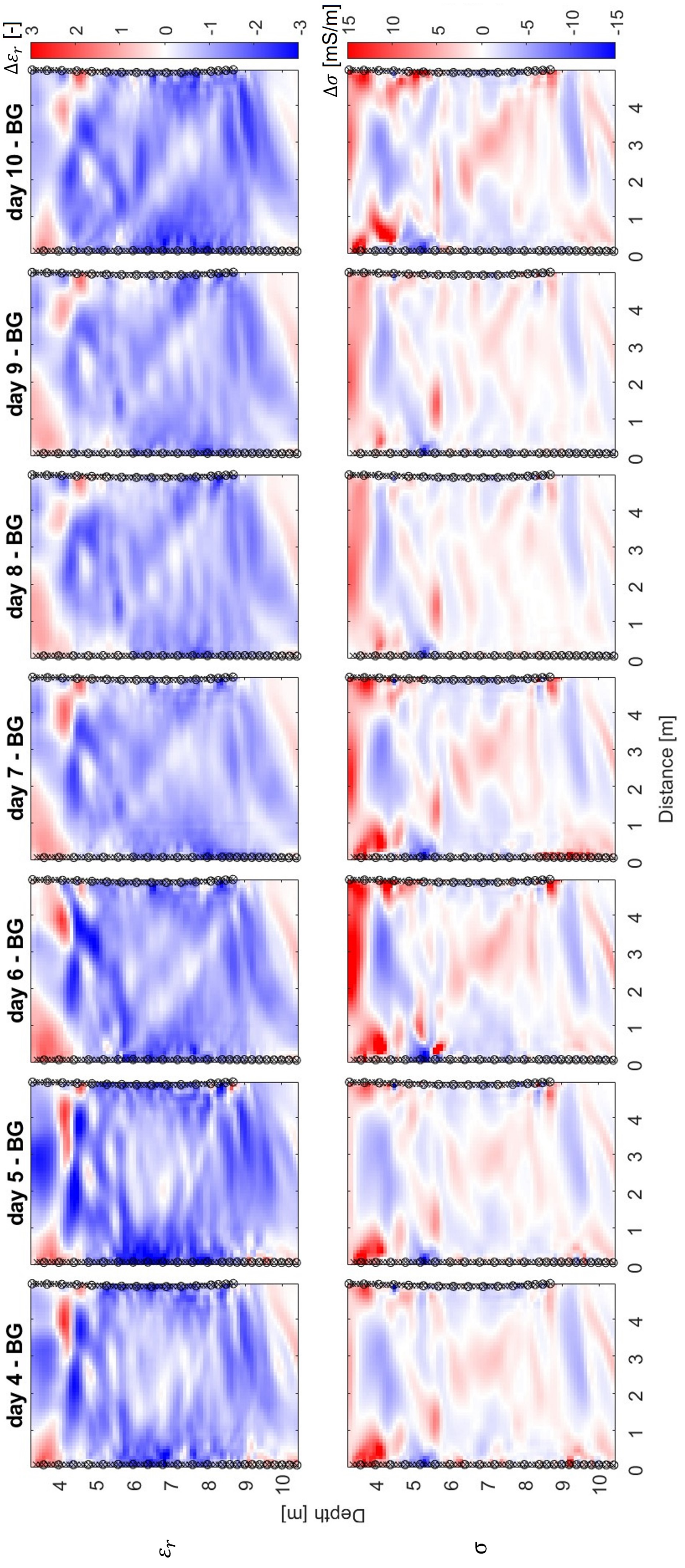

Figure A-8: Time-lapse difference FWI results with respect to the background until day 10 for Plane 3831. The top row shows the FWI permittivity and the bottom row the FWI conductivity with the background FWI subtracted for each time-lapse dataset (columns).

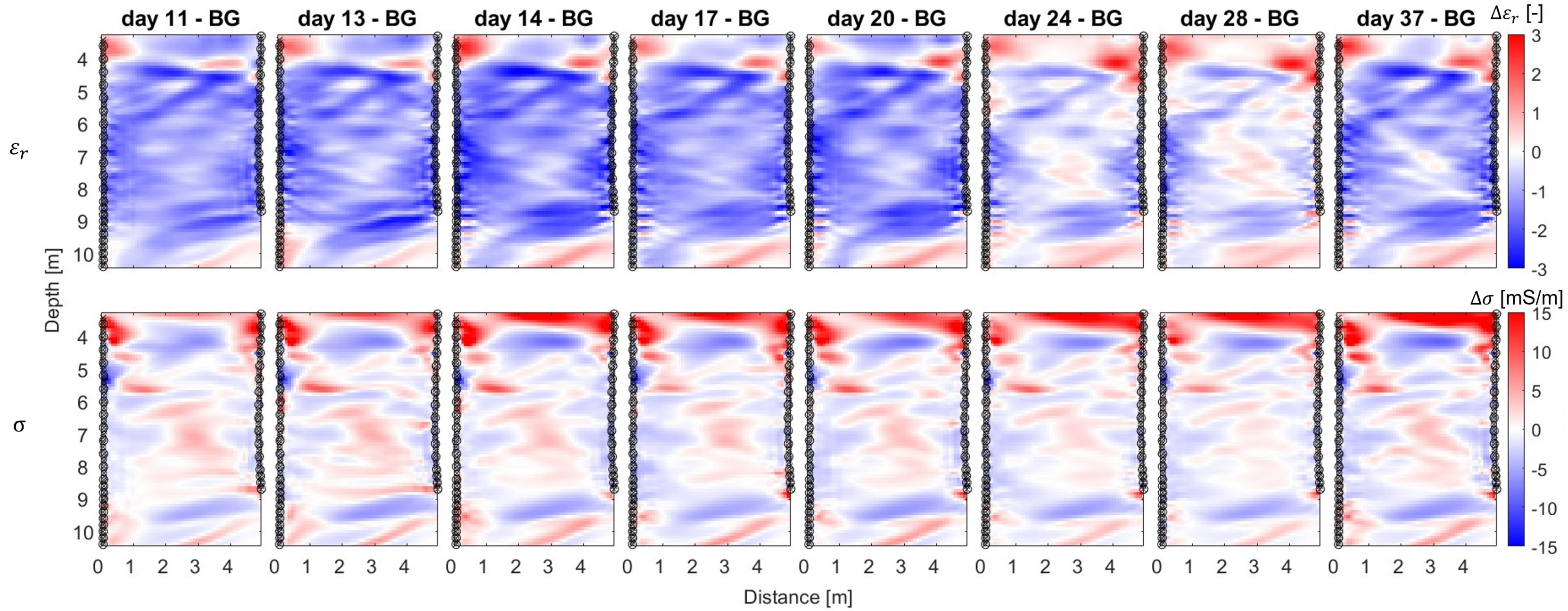

Figure A-9: Time-lapse difference FWI results with respect to the background for day 11-37 for Plane 3831. The top row shows the FWI permittivity and the bottom row the FWI conductivity with the background FWI subtracted for each time-lapse dataset (columns).

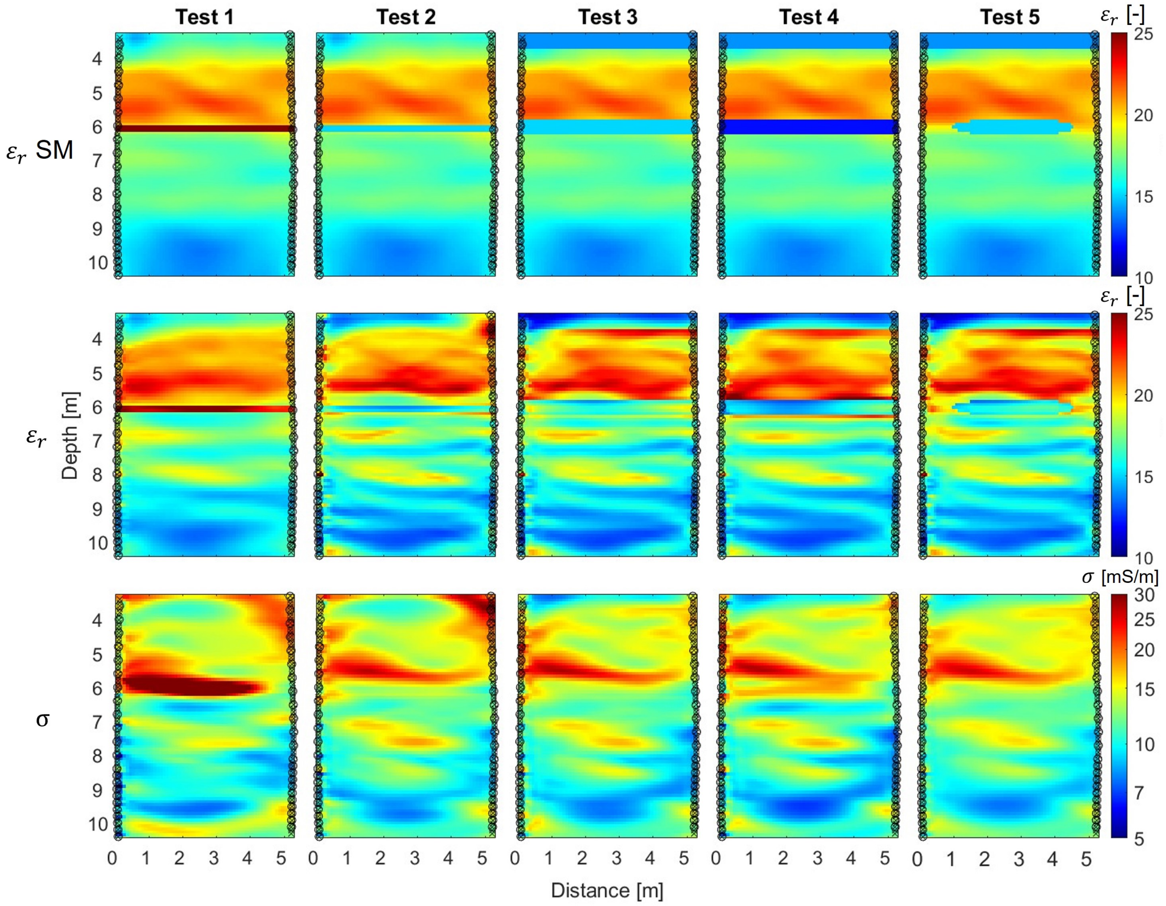

Figure A-10: FWI results for the day 5 dataset of Plane 2938 with different layers added to the starting model. The top row shows the different adapted starting models, the middle row the final FWI permittivity, and the bottom the final FWI conductivity result. Note the logarithmic scale for the conductivity. The transmitter and receiver locations are indicated with circles and crosses, respectively.

Appendix B

Heat-salt tracer additional results

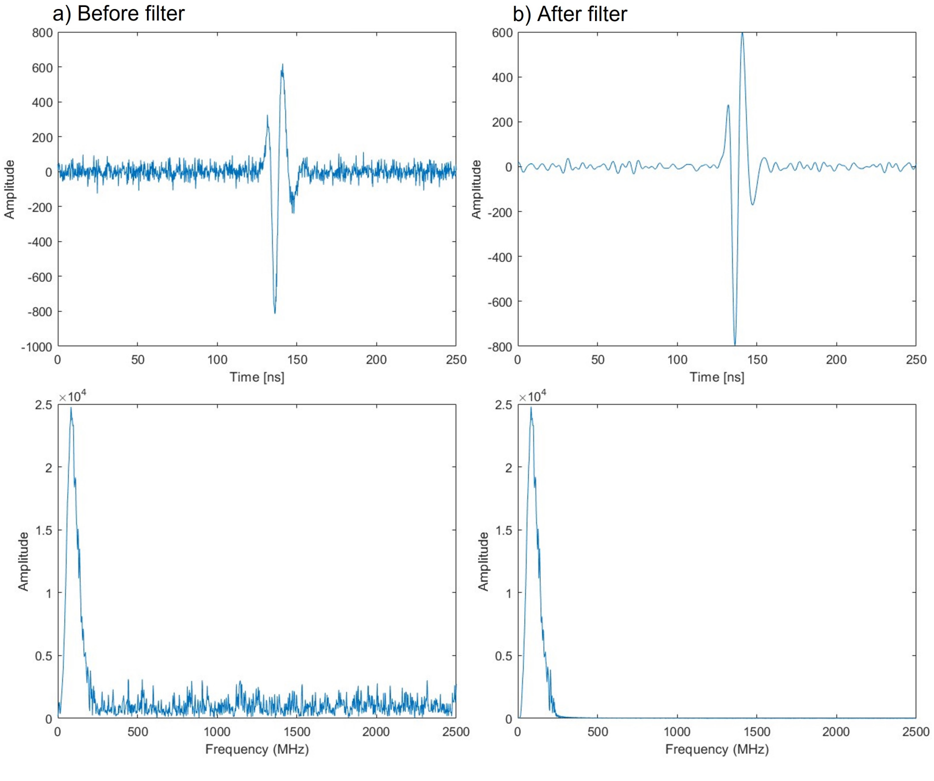

Figure B-1: Day 3 trace 40 from MOG with transmitter at 4.44 m in B31 and the corresponding amplitude spectrum a) before and b) after applying a bandpass filter.

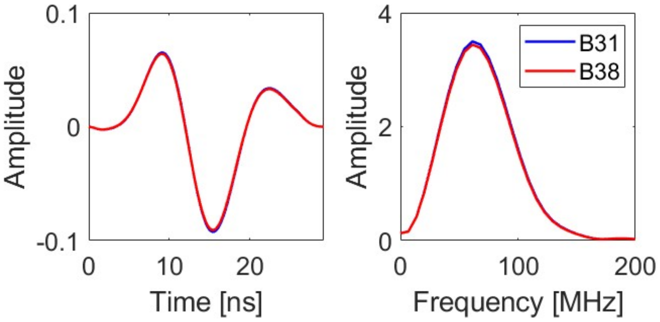

Figure B-2: Comparison of effective source wavelets for day 4 estimated using only data with transmitters in B31 and B38.

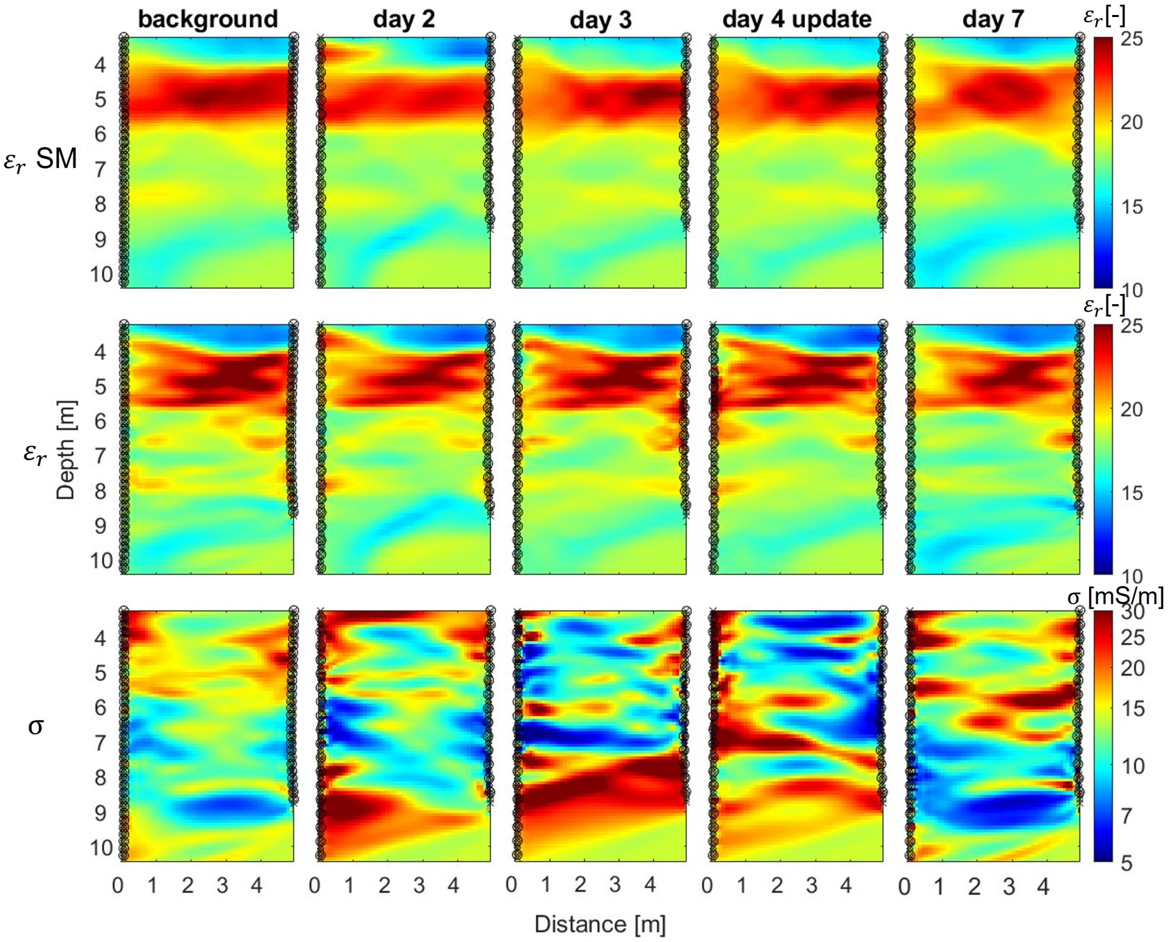

Figure B-3: Time-lapse FWI results for the heat-salt tracer experiment with the updated day 4 starting model, Plane 3831. The background FWI model is subtracted from each time-lapse FWI model. The top row shows the FWI permittivity difference and the bottom row the FWI conductivity difference for each time-lapse dataset and for day 4 using an updated starting model (columns). The left of the plane is B38 and the right is B31, where data are only measured until 8.84 m depth.

Bibliography

Amirabdollahian, M. and Datta, B. (2013). Identification of contaminant source characteristics and monitoring network design in groundwater aquifers: An overview. *Journal of Environmental Protection*, 4:26–41.

Annan, A. (2005a). Ground-penetrating radar. In *Near-surface geophysics*, pages 357–438. Society of Exploration Geophysicists.

Annan, A. P. (2005b). GPR methods for hydrogeological studies. In *Hydrogeophysics*, pages 185–213. Springer.

Archie, G. E. (1942). The electrical resistivity log as an aid in determining some reservoir characteristics. *Transactions of the AIME*, 146(01):54–62.

Axtell, C., Murray, T., Kulessa, B., Clark, R. A., and Gusmeroli, A. (2016). Improved accuracy of cross-borehole radar velocity models for ice property analysis. *Geophysics*, 81(1):WA203–WA212.

Binley, A., Cassiani, G., Middleton, R., and Winship, P. (2002). Vadose zone flow model parameterisation using cross-borehole radar and resistivity imaging. *Journal of Hydrology*, 267(3-4):147–159.

Binley, A., Hubbard, S. S., Huisman, J. A., Revil, A., Robinson, D. A., Singha, K., and Slater, L. D. (2015). The emergence of hydrogeophysics for improved understanding of subsurface processes over multiple scales. *Water resources research*, 51(6):3837–3866.

Bleistein, N. (1986). Two-and-one-half dimensional in-plane wave propagation. *Geophysical prospecting*, 34(5):686–703.

Bradford, J. H., Clement, W. P., and Barrash, W. (2009). Estimating porosity with ground-penetrating radar reflection tomography: A controlled 3-D experiment at the Boise Hydrogeophysical Research Site. *Water Resources Research*, 45(4).

Cassidy, N. J. and Jol, H. (2009). Ground penetrating radar data processing, modelling and analysis. *Ground penetrating radar: theory and applications*, pages 141–176.

Catenaccio, A., Daruich, Y., and Magallanes, C. (2003). Temperature dependence of the permittivity of water. *Chemical physics letters*, 367(5-6):669–671.

Chen, J., Hubbard, S. S., Gaines, D., Korneev, V., Baker, G., and Watson, D. (2010). Stochastic estimation of aquifer geometry using seismic refraction data with borehole depth constraints. *Water Resources Research*, 46(11).

Cirpka, O. A., Leven, C., Schwede, R., Doro, K., Bastian, P., Ippisch, O., Klein, O., and Patzelt, A. (2014). Tomographic methods in hydrogeology. *Tomography of the Earth's Crust: From Geophysical Sounding to Real-Time Monitoring: GEOTECHNOLOGIEN Science Report No. 21*, pages 157–176.

Coscia, I., Greenhalgh, S. A., Linde, N., Doetsch, J., Marescot, L., Günther, T., Vogt, T., and Green, A. G. (2011). 3D crosshole ERT for aquifer characterization and monitoring of infiltrating river water. *Geophysics*, 76(2):G49–G59.

Dafflon, B., Irving, J., and Barrash, W. (2011). Inversion of multiple intersecting high-resolution crosshole GPR profiles for hydrological characterization at the Boise Hydrogeophysical Research site. *Journal of Applied Geophysics*, 73(4):305–314.

Doetsch, J., Linde, N., Vogt, T., Binley, A., and Green, A. G. (2012). Imaging and quantifying salt-tracer transport in a riparian groundwater system by means of 3d ERT monitoring. *Geophysics*, 77(5):B207–B218.

Döring, U. (1997). Transport der reaktiven Stoffe Eosin, Uranin und Lithium in einem heterogenen Grundwasserleiter. *BERICHTE-FORSCHUNGSZENTRUM JULICH JUL*.

Dorn, C., Linde, N., Le Borgne, T., Bour, O., and Baron, L. (2011). Single-hole GPR reflection imaging of solute transport in a granitic aquifer. *Geophysical Research Letters*, 38(8).

Englert, A. (2003). *Measurement, estimation and modelling of groundwater flow velocity at Krauthausen test site*. PhD thesis, Bibliothek der RWTH Aachen.

Ernst, J. R., Green, A. G., Maurer, H., and Holliger, K. (2007a). Application of a new 2D time-domain full-waveform inversion scheme to crosshole radar data. *Geophysics*, 72(5):J53–J64.

Ernst, J. R., Maurer, H., Green, A. G., and Holliger, K. (2007b). Full-waveform inversion of crosshole radar data based on 2-D finite-difference time-domain solutions of Maxwell's equations. *IEEE transactions on geoscience and remote sensing*, 45(9):2807–2828.

Giertzuch, P.-L., Doetsch, J., Jalali, M., Shakas, A., Schmelzbach, C., and Maurer, H. (2020). Time-lapse ground penetrating radar difference reflection imaging of saline tracer flow in fractured rock. *Geophysics*, 85(3):H25–H37.

Goldscheider, N., Meiman, J., Pronk, M., and Smart, C. (2008). Tracer tests in karst hydrogeology and speleology. *International Journal of speleology*, 37(1):3.

Gueting, N., Klotzsche, A., van der Kruk, J., Vanderborght, J., Vereecken, H., and Englert, A. (2015). Imaging and characterization of facies heterogeneity in an alluvial aquifer using GPR full-waveform inversion and cone penetration tests. *Journal of hydrology*, 524:680–695.

Gueting, N., Vienken, T., Klotzsche, A., van der Kruk, J., Vanderborght, J., Caers, J., Vereecken, H., and Englert, A. (2017). High resolution aquifer characterization using crosshole GPR full-waveform tomography: Comparison with direct-push and tracer test data. *Water Resources Research*, 53(1):49–72.

Haruzi, P. (2023). *High-resolution imaging of transport processes with GPR full-waveform inversion*. PhD thesis, Universität zu Köln.

Haruzi, P., Schmäck, J., Zhou, Z., van der Kruk, J., Vereecken, H., Vanderborght, J., and Klotzsche, A. (2022). Detection of tracer plumes using full-waveform inversion of time-lapse ground penetrating radar data: A numerical study in a high-resolution aquifer model. *Water Resources Research*, 58(5):e2021WR030110.

Hermans, T., Wildemeersch, S., Jamin, P., Orban, P., Brouyère, S., Dassargues, A., and Nguyen, F. (2015). Quantitative temperature monitoring of a heat tracing experiment using cross-borehole ert. *Geothermics*, 53:14–26.

Holliger, K., Musil, M., and Maurer, H. (2001). Ray-based amplitude tomography for crosshole georadar data: A numerical assessment. *Journal of Applied Geophysics*, 47(3-4):285–298.

Huisman, J. A., Hubbard, S. S., Redman, J. D., and Annan, A. P. (2003). Measuring soil water content with ground penetrating radar: A review. *Vadose zone journal*, 2(4):476–491.

Jol, H. M. (2008). *Ground penetrating radar theory and applications*. elsevier.

Kaatze, U. (1989). Complex permittivity of water as a function of frequency and temperature. *Journal of Chemical and Engineering Data*, 34(4):371–374.

Kearey, P., Brooks, M., and Hill, I. (2002). *An introduction to geophysical exploration*, volume 4. John Wiley & Sons.

Kemna, A., Vanderborght, J., Kulessa, B., and Vereecken, H. (2002). Imaging and characterisation of subsurface solute transport using electrical resistivity tomography (ERT) and equivalent transport models. *Journal of hydrology*, 267(3-4):125–146.

Keskinen, J., Looms, M. C., Klotzsche, A., and Nielsen, L. (2021). Practical data acquisition strategy for time-lapse experiments using crosshole GPR and full-waveform inversion. *Journal of Applied Geophysics*, 191:104362.

Klepikova, M., Wildemeersch, S., Hermans, T., Jamin, P., Orban, P., Nguyen, F., Brouyère, S., and Dassargues, A. (2016). Heat tracer test in an alluvial aquifer: Field experiment and inverse modelling. *Journal of Hydrology*, 540:812–823.

Klotzsche, A., Jonard, F., Looms, M. C., van der Kruk, J., and Huisman, J. A. (2018). Measuring soil water content with ground penetrating radar: A decade of progress. *Vadose Zone Journal*, 17(1):1–9.

Klotzsche, A., van der Kruk, J., Bradford, J., and Vereecken, H. (2014). Detection of spatially limited high-porosity layers using crosshole GPR signal analysis and full-waveform inversion. *Water Resources Research*, 50(8):6966–6985.

Klotzsche, A., van der Kruk, J., Meles, G., and Vereecken, H. (2012). Crosshole gpr full-waveform inversion of waveguides acting as preferential flow paths within aquifer systems. *Geophysics*, 77(4):H57–H62.

Klotzsche, A., van der Kruk, J., Meles, G. A., Doetsch, J., Maurer, H., and Linde, N. (2010). Full-waveform inversion of cross-hole ground-penetrating radar data to characterize a gravel aquifer close to the Thur River, Switzerland. *Near surface geophysics*, 8(6):635–649.

Klotzsche, A., Vereecken, H., and van der Kruk, J. (2019a). GPR full-waveform inversion of a variably saturated soil-aquifer system. *Journal of Applied Geophysics*, 170:103823.

Klotzsche, A., Vereecken, H., and van der Kruk, J. (2019b). Review of crosshole ground-penetrating radar full-waveform inversion of experimental data: Recent developments, challenges, and pitfalls. *Geophysics*, 84(6):H13–H28.

Kurzmann, A., Przebindowska, A., Köhn, D., and Bohlen, T. (2013). Acoustic full waveform tomography in the presence of attenuation: A sensitivity analysis. *Geophysical Journal International*, 195(2):985–1000.

Lavoué, F., Brossier, R., Métivier, L., Garambois, S., and Virieux, J. (2014). Two-dimensional permittivity and conductivity imaging by full waveform inversion of multioffset gpr data: A frequency-domain quasi-newton approach. *Geophysical Journal International*, 197(1):248–268.

Li, W., Englert, A., Cirpka, O. A., Vanderborght, J., and Vereecken, H. (2007). Two-dimensional characterization of hydraulic heterogeneity by multiple pumping tests. *Water Resources Research*, 43(4).

Linde, N., Binley, A., Tryggvason, A., Pedersen, L. B., and Revil, A. (2006). Improved hydrogeophysical characterization using joint inversion of cross-hole electrical resistance and ground-penetrating radar traveltime data. *Water Resources Research*, 42(12).

Looms, M. C., Jensen, K. H., Binley, A., and Nielsen, L. (2008). Monitoring unsaturated flow and transport using cross-borehole geophysical methods. *Vadose zone journal*, 7(1):227–237.

Maurer, H. and Musil, M. (2004). Effects and removal of systematic errors in crosshole georadar attenuation tomography. *Journal of Applied Geophysics*, 55(3-4):261–270.

Meles, G., Greenhalgh, S., Van der Kruk, J., Green, A., and Maurer, H. (2012). Taming the non-linearity problem in GPR full-waveform inversion for high contrast media. *Journal of Applied Geophysics*, 78:31–43.

Meles, G. A., Van der Kruk, J., Greenhalgh, S. A., Ernst, J. R., Maurer, H., and Green, A. G. (2010). A new vector waveform inversion algorithm for simultaneous updating of conductivity and permittivity parameters from combination crosshole/borehole-to-surface GPR data. *IEEE Transactions on geoscience and remote sensing*, 48(9):3391–3407.

Mozaffari, A. (2022). Towards 3d crosshole gpr full-waveform inversion. Technical report, Agrosphäre.

Mozaffari, A., Klotzsche, A., Warren, C., He, G., Giannopoulos, A., Vereecken, H., and van der Kruk, J. (2020). 2.5D crosshole gpr full-waveform inversion with synthetic and measured data. *Geophysics*, 85(4):H71–H82.

Mozaffari, A., Klotzsche, A., Zhou, Z., Vereecken, H., and Van der Kruk, J. (2021). 3-d electromagnetic modeling explains apparent-velocity increase in crosshole gpr data-borehole fluid effect correction method enables to incorporating high-angle traveltime data. *IEEE Transactions on Geoscience and Remote Sensing*, 60:1–10.

Müller, K., Vanderborght, J., Englert, A., Kemna, A., Huisman, J. A., Rings, J., and Vereecken, H. (2010). Imaging and characterization of solute transport during two tracer tests in a shallow aquifer using electrical resistivity tomography and multilevel groundwater samplers. *Water Resources Research*, 46(3).

Oberröhrmann, M., Klotzsche, A., Vereecken, H., and van der Krak, J. (2013). Optimization of acquisition setup for cross-hole: GPR full-waveform inversion using checkerboard analysis. *Near Surface Geophysics*, 11(2):197–209.

Rau, G. C., Andersen, M. S., McCallum, A. M., Roshan, H., and Acworth, R. I. (2014). Heat as a tracer to quantify water flow in near-surface sediments. *Earth-Science Reviews*, 129:40–58.

Revil, A., Cathles III, L., Losh, S., and Nunn, J. (1998). Electrical conductivity in shaly sands with geophysical applications. *Journal of Geophysical Research: Solid Earth*, 103(B10):23925–23936.

Seyfried, M. S. and Grant, L. E. (2007). Temperature effects on soil dielectric properties measured at 50 mhz. *Vadose Zone Journal*, 6(4):759–765.

Shakas, A., Linde, N., Baron, L., Selker, J., Gerard, M.-F., Lavenant, N., Bour, O., and Le Borgne, T. (2017). Neutrally buoyant tracers in hydrogeophysics: Field demonstration in fractured rock. *Geophysical Research Letters*, 44(8):3663–3671.

Slob, E., Sato, M., and Olhoeft, G. (2010). Surface and borehole ground-penetrating-radar developments. *Geophysics*, 75(5):75A103–75A120.

Steelman, C. M. and Endres, A. L. (2011). Comparison of petrophysical relationships for soil moisture estimation using GPR ground waves. *Vadose Zone Journal*, 10(1):270–285.

Tarantola, A. (1984). Inversion of seismic reflection data in the acoustic approximation. *Geophysics*, 49(8):1259–1266.

Tillmann, A., Englert, A., Nyari, Z., Fejes, I., Vanderborght, J., and Vereecken, H. (2008). Characterization of subsoil heterogeneity, estimation of grain size distribution and hydraulic conductivity at the Krauthausen test site using cone penetration test. *Journal of contaminant hydrology*, 95(1-2):57–75.

Topp, G. C., Davis, J., and Annan, A. P. (1980). Electromagnetic determination of soil water content: Measurements in coaxial transmission lines. *Water resources research*, 16(3):574–582.

Turesson, A. (2006). Water content and porosity estimated from ground-penetrating radar and resistivity. *Journal of Applied Geophysics*, 58(2):99–111.

van der Kruk, J., Gueting, N., Klotzsche, A., He, G., Rudolph, S., von Hebel, C., Yang, X., Weihermüller, L., Mester, A., and Vereecken, H. (2015). Quantitative multi-layer electromagnetic induction inversion and full-waveform inversion of crosshole ground penetrating radar data. *Journal of Earth Science*, 26:844–850.

van der Kruk, J., Liu, T., Mozaffari, A., Gueting, N., Klotzsche, A., Vereecken, H., Warren, C., and Giannopoulos, A. (2018). GPR full-waveform inversion, recent developments, and future opportunities. In *2018 17th International Conference on Ground Penetrating Radar (GPR)*, pages 1–6. IEEE.

Van der Kruk, J., Steelman, C., Endres, A., and Vereecken, H. (2009). Dispersion inversion of electromagnetic pulse propagation within freezing and thawing soil waveguides. *Geophysical Research Letters*, 36(18).

Vereecken, H., Döring, U., Hardelauf, H., Jaekel, U., Hashagen, U., Neuendorf, O., Schwarze, H., and Seidemann, R. (2000). Analysis of solute transport in a heterogeneous aquifer: the Krauthausen field experiment. *Journal of Contaminant Hydrology*, 45(3-4):329–358.

Vidale, J. E. (1990). Finite-difference calculation of traveltimes in three dimensions. *Geophysics*, 55(5):521–526.

Yang, X., Klotzsche, A., Meles, G., Vereecken, H., and Van Der Kruk, J. (2013). Improvements in crosshole gpr full-waveform inversion and application on data measured at the boise hydrogeophysics research site. *Journal of Applied Geophysics*, 99:114–124.

Zheng, C. and Gorelick, S. M. (2003). Analysis of solute transport in flow fields influenced by preferential flowpaths at the decimeter scale. *Groundwater*, 41(2):142–155.

Zhou, Z., Klotzsche, A., Hermans, T., Nguyen, F., Schmäck, J., Haruzi, P., Vereecken, H., and van der Kruk, J. (2020). 3D aquifer characterization of the Hermalle-sous-Argenteau test site using crosshole ground-penetrating radar amplitude analysis and full-waveform inversion GPR amplitude analysis and FWI for 3D imaging. *Geophysics*, 85(6):H133–H148.

Zhou, Z., Klotzsche, A., Schmäck, J., Vereecken, H., and van der Kruk, J. (2021). Improvement of ground-penetrating radar full-waveform inversion images using cone penetration test data: Improvement of GPR FWI images using CPT. *Geophysics*, 86(3):H13–H25.

List of Figures

List of Tables

Acronyms

AA	Amplitude Analysis
BG	Background
CMP	Common midpoint
EM	Electromagnetic
ERT	Electrical resistivity tomography
FDTD	Finite difference time domain
FWI	Full-waveform inversion
GPR	Ground penetrating radar
JSC	Jülich Supercomputing Center
JURECA	Jülich Research on Exascale Cluster Architectures
MOG	Multi-offset gather
RMS	Root-mean-squared error
RWTH	Rheinisch-Westfälische Technische Hochschule Aachen
SM	Starting model
WARR	Wide angle reflection and refraction
ZOP	Zero-offset profile